


12-2018

Exploration of radiation damage mechanism in mems devices.

Pranoy Deb Shuvra
University of Louisville

Follow this and additional works at: <https://ir.library.louisville.edu/etd>

 Part of the [Electronic Devices and Semiconductor Manufacturing Commons](#), [Nanoscience and Nanotechnology Commons](#), [Nanotechnology Fabrication Commons](#), and the [Nuclear Engineering Commons](#)

Recommended Citation

Shuvra, Pranoy Deb, "Exploration of radiation damage mechanism in mems devices." (2018). *Electronic Theses and Dissertations*. Paper 3119.

<https://doi.org/10.18297/etd/3119>

This Doctoral Dissertation is brought to you for free and open access by ThinkIR: The University of Louisville's Institutional Repository. It has been accepted for inclusion in Electronic Theses and Dissertations by an authorized administrator of ThinkIR: The University of Louisville's Institutional Repository. This title appears here courtesy of the author, who has retained all other copyrights. For more information, please contact thinkir@louisville.edu.

EXPLORATION OF RADIATION DAMAGE MECHANISM IN MEMS DEVICES

By

Pranoy Deb Shuvra

University of Louisville

A Dissertation

Submitted to the Faculty of the

J. B. Speed School of Engineering of the University of Louisville

in Partial Fulfillment of the Requirements for the Degree of

Doctor of Philosophy in Electrical Engineering

Department of Electrical and Computer Engineering

University of Louisville

Louisville, KY 40292

December 2018

EXPLORATION OF RADIATION DAMAGE MECHANISM IN MEMS DEVICES

By

Pranoy Deb Shuvra
University of Louisville

A Dissertation Approved on
November 14, 2018
by the following Dissertation Committee

Dr. Shamus P. McNamara (Dissertation Advisor)

Dr. Bruce Alphenaar

Dr. Kevin Walsh

Dr. Gamini Sumanasekera

DEDICATION

To my parents, Pankaj Kumar Deb and Namita Rani Deb, for their endless patience, love and inspiration. They are the root of all my success.

ACKNOWLEDGEMENTS

I am very grateful for all the support that I got during my PhD program. I would like to take the opportunity to express my gratitude to the following exceptionally kind people who helped me to pass all the hurdles on the way of my graduation.

First, I would like to express my deepest gratitude to my adviser Dr. Shamus McNamara for his continuous support over the last 7 years. He always inspired me and guided me in the right direction. This dissertation would not be possible without his guidance.

I am especially grateful to Dr. Bruce Alphenaar for believing in my potential and giving me the opportunity to work in the DTRA (Defense Threat Reduction Agency) program. I am also very grateful to Dr. Kevin Walsh for his unconditional support and for sharing valuable insights in this project. I would like to thank Dr. Gamini Sumanasekera for his time and effort in evaluating my dissertation and giving valuable feedback.

Special thanks to Dr. Ji-Tzuoh Lin for helping me succeed in my academic endeavors and for being a great friend. I would like to thank Vanderbilt University professors: Dr. Jim Davidson and Dr. Michael Alles for sharing their valuable knowledge and insight in our weekly meetings. I would also like to thank Vanderbilt university students: Charles Nathan Arutt, Huiqi Gong and Wenjun Liao for their help with X-ray experiments.

Thanks to my friend Sri Sukanta Chowdhury for helping me at different stages of my education and personal life. He has been a great friend over the last 14 years and counting. Also, thanks to Dr. Julia Aebersold, Dr. Evgeniya Moiseeva, Xiaojin Wang and Curt McKenna for training me to use the cleanroom equipment and sharing their findings.

I would like to acknowledge and thank DTRA (Defense Threat Reduction Agency) program for the financial support through Grant HDTRA1-15-1-0027 and hope that they will continue to promote excellent fundamental research.

Last but not least, I would like to thank my wife, Chandnee Das, for her patience, sacrifices and immense help towards my graduation.

ABSTRACT

EXPLORATION OF RADIATION DAMAGE MECHANISM IN MEMS DEVICES

Pranoy Deb Shuvra

November 14, 2018

We explored UV, X-ray and proton radiation damage mechanisms in MEMS resonators. T-shaped MEMS resonators of different dimensions were used to investigate the effect of radiation. Radiation damage is observed in the form of resistance and resonance frequency shift of the device. The resistance change indicates a change in free carrier concentration and mobility, while the resonance frequency change indicates a change in mass and/or elastic constant.

For 255nm UV radiation, we observed a persistent photoconductivity that lasts for about 60 hours after radiation is turned off. The resonance frequency also decreases 40-90 ppm during irradiation and slowly recovers at about the same time scale as the resistance during annealing. For X-ray radiation, the resonance frequency decreases with radiation, but the resistance increases. To investigate X-ray dose-rate dependence, we irradiated the resonators at three different dose rates of X-ray: 5.4, 10.9 and 30.3 krad(SiO₂)/min. The change in resonance frequency and resistance both showed a dose rate dependence where a lower dose-rate X-ray caused a larger shift in resonance frequency than the higher dose-rate. We attributed the observed shift in resonance frequency to the change in carrier

concentration—using Keyes’ theory of electronic contribution to elastic constant—for both X-ray and UV radiation. The resistance change is explained by the net effect of the carrier concentration and mobility change.

We proposed that the carrier concentration changes through two differing mechanisms for X-ray and UV radiation. For X-ray, dopant depassivation is primarily responsible for the carrier concentration change since an X-ray is known to dissociate the hydrogen-boron complex and it penetrates through the 15 μm thick Si resonator affecting the whole bulk of Si. On the contrary, the 255nm UV gets absorbed near the surface (within 10nm) and charges the native oxide. The mirror charge on adjacent silicon is responsible for the carrier concentration change. The mirror charges drive the silicon surface to accumulation, depletion or strong inversion depending on the type and amount of charge trapped in the oxide. Since the carrier concentration only changes near the surface, it was predicted that higher surface-to-volume ratio devices will show a greater shift in resonance frequency. This was proven by radiating three devices with differing widths (1, 2 and 8 μm), and therefore differing surface-to-volume ratios. This experiment verified that the UV light effect is surface dominated.

The dimensional dependence is also observed for X-ray radiation damage. We found that a reduction in the surface-to-volume ratio enhances the X-ray radiation damage and we proposed a hydrogen diffusion-based model that fits the observed dimensional dependence of X-ray radiation damage.

For proton radiation, the direction of resonance frequency change depended on the energy of radiated proton. Two proton energies were tested: 0.8MeV and 2MeV. The proton with 0.8MeV energy stops inside the resonator, causing greater displacement

damage than the proton with 2MeV energy, which readily passes through the resonator. The 2MeV proton causes more ionization damage than the 0.8MeV protons. So, the observed energy dependence of resonance frequency shift comes from the competing effects of displacement damage and ionization damage since resonance frequency decreases due to ionization damage but increases due to displacement damage. The result agrees with our theory since the 0.8MeV proton radiation showed net resonance frequency increase during radiation and more permanent damage after annealing compared to the 2MeV proton radiation.

TABLE OF CONTENTS

ACKNOWLEDGEMENTS	iv
ABSTRACT	vi
LIST OF FIGURES	xiii
LIST OF TABLES	xxiii
CHAPTER I INTRODUCTION	1
1.1 Motivation	1
1.2 Overview of the radiation damage	3
1.3 Objectives	4
1.4 Dissertation outline	5
CHAPTER II LITERATURE REVIEW	7
2.1 Displacement damage	7
2.2 Ionization damage	11
2.3 Material properties affected by radiation	14
2.3.1. Effect on resistivity	14
2.3.1.1. Persistent photoconductivity	18
2.3.1.2. Hydrogen passivation	23

2.3.2. Effect on elastic constant.....	30
2.4 Conclusion.....	36
CHAPTER III ASYMMETRIC MEMS RESONATOR.....	38
3.1 Asymmetric and symmetric mems piezoresistors.....	40
3.1.1. Symmetric Piezoresistor Theory	43
3.1.2. Asymmetric Piezoresistor Theory.....	45
3.2 Finite element analysis	47
3.3 Lumped parameter model.....	53
3.4 Experimental results	56
3.5 Conclusion.....	56
CHAPTER IV FABRICATION AND EXPERIMENTAL SETUP.....	58
4.1 Fabrication of Si MEMS resonators.....	59
4.1.1. Metal deposition and etching.....	62
4.1.2. Photolithography	64
4.1.3. Deep Reactive Ion Etching of Si	66
4.1.4. Dry Etching of SiO ₂ in Trion Metal Etcher	68
4.1.5. Anhydrous HF release	70
4.2 Packaging and wire-bonding.....	71
4.3 Resonance frequency measurement	72
4.3.1. UV radiation exposure setup	74

4.3.2. X-ray radiation exposure setup.....	76
4.3.3. Proton radiation exposure setup	77
4.4 Base resistance measurement	78
4.5 Data acquisition and analysis	79
4.6 Conclusion.....	79
CHAPTER V RESULTS.....	81
5.1 UV radiation experimental result	82
5.1.1. Effect of doping type and concentration	85
5.1.1. Effect of beam width	87
5.2 X-ray radiation experimental result.....	89
5.2.1. Effect of dose rate.....	91
5.2.2. Effect on base resistance	94
5.2.3. Effect of doping type.....	97
5.2.4. Effect of beam width	98
5.3 Proton radiation experimental result	101
5.4 Conclusion.....	103
CHAPTER VI THEORETICAL MODELS AND DISCUSSIONS.....	104
6.1 Model of UV radiation damage.....	105
6.1.1. Spring softening.....	105
6.1.2. Gas adsorption on surface	110

6.1.3. Resistance change due to photocarriers.....	112
6.1.4. Trapping of photocarriers at native oxide	119
6.1.5. Resonance frequency modulation by excess free carriers.....	124
6.2 Model of X-ray radiation damage	131
A. Resistance change during X-ray radiation	133
B. Dimensional dependence of X-ray radiation damage	136
6.3 Model of proton radiation damage	141
6.4 Conclusion.....	144
CHAPTER VII CONCLUSION	145
REFERENCES	148
CURRICULUM VITA	163

LIST OF FIGURES

<p>Fig. 1. Single characteristic curve obtained by plotting normalized maximum power degradation parameter of a solar cell with respect to displacement damage dose caused by proton and electron having a range of energies.</p>	9
<p>Fig. 2. Ionization process during electromagnetic radiation where p_e denotes photoelectrons, e_a denotes excited atom, e_h denotes electron hole pairs, A_e denotes Auger electron, I denotes ions, F denotes electric field, s denotes escape length and $\rho(z)$ shows charge density profile with respect to depth from the surface [15].</p>	11
<p>Fig. 3. (a) Mobility vs. temperature plot showing the dominant scattering mechanism at two temperature ranges [5], (b) Impurity concentration vs. mobility at room temperature for three different semiconductors [5].</p>	16
<p>Fig. 4. (a) Fermi distribution of trapped-hole density usually found in substrates with moderate amount of trap states, (b) simplified rectangular distribution (c) simplified triangular distribution, (d) shifted rectangular distribution.....</p>	21
<p>Fig. 5. Lattice positions in crystalline silicon at (110) plane showing BB (backbonding) site, AB (antibonding) site, Bond minimum (BM) site and tetrahedral (T_d) interstitial site and hexagonal (H and H') interstitial site [12].</p>	24
<p>Fig. 6. Experimental (solid line) and calculated (dashed line) hydrogen concentration profile in high resistivity (100 Ωcm) silicon after hydrogenation for 1h at 125⁰C using deuterium plasma [11].</p>	27

Fig. 7. Experimental (circles) and calculated (solid line) hydrogen concentration profile in highly doped (Boron concentration $5 * 10^{18} \text{ cm}^{-3}$) p-type silicon after hydrogenation for 30min at 150°C using deuterium plasma [14]..... 29

Fig. 8. (a) Symmetric and, (b) Asymmetric MEMS cantilever piezoresistor with dimensions [10]..... 40

Fig. 9. Schematic illustration of base bending in asymmetric and symmetric models in two directions..... 42

Fig. 10. (a) Schematic showing the position of neutral axis (dotted line) in the asymmetric model for bending in left direction. (b) Equivalent circuit of a short section of the base under bending. (c) Schematic showing the neutral axis is centered in the base beam in the symmetric piezoresistor. (d) Equivalent circuit of a short section of the symmetric base under bending with equal magnitude but opposite signs for the change in resistance. 45

Fig. 11. Stress distribution 3D color plot when beam is displaced in the left direction for the asymmetric (a) and the symmetric (b) model. 48

Fig. 12. Stress distribution along the edges of the base beam for (a) asymmetric model thick arm, (b) asymmetric model thin arm and, (c) symmetric model right arm. The red line shows the average of each two stresses along the length of the arms..... 49

Fig. 13. (a) Comparison of asymmetric and symmetric piezoresistor performance with respect to percent resistance change in linear scale and, (b) comparison of performance for asymmetric, symmetric and diffused piezoresistor model in log scale. Inset of (a) shows the percent change in resistance versus displacement plot of symmetric case

separately with magnified y-axis to clearly show the unidirectional nature of resistance change with displacement in either direction.....	50
Fig. 14. (a) Plot of sensitivity versus width showing the optimum width of the left arm is 12.5 μm . Inset: Percentage of resistance change versus displacement for several left arm widths, (b) percent change in displacement for different thick arm widths.....	51
Fig. 15. (a) Creating nine separate piezoresistor elements out of the bulk model to formulate the lumped parameter model, (b) Equivalent circuit for the lumped parameter model.....	52
Fig. 16. Sensitivity values ($\times 10^{-6} \mu\text{m}^{-1}$) of each piezoresistor element for asymmetric model and symmetric model.....	53
Fig. 17. Comparison of experimental, simulation and lumped model with respect to displacement vs. percent change in base resistance plot.....	56
Fig. 18. Fabrication flowchart showing the major steps in the fabrication.....	59
Fig. 19. (a) Optical micrograph of the fabricated device with dimensions (b) Magnified view of the piezoresistor base.....	60
Fig. 20. (a) PVD75 system in the MNTC cleanroom, (b) The deposition chamber inside the PVD75 system [7].....	62
Fig. 21. (a) Al contact pads and (b) gold contact pads after wet etching of exposed contact metals.....	63
Fig. 22. (a) SUSS Mask Aligner in the cleanroom [6] and, (2) alignment marks (at two levels of magnification) used for the lithography.....	64
Fig. 23. DRIE tool at the MNTC's cleanroom.....	65

Fig. 24. (a) Resonator structure after the dry etch process, (b) zoomed-in view of the tip of the cantilever. The resonator is still attached to the substrate by the sacrificial oxide layer.....	67
Fig. 25. (a) After the backside window etch using DRIE, (b) Zoomed-in view showing the resonator from the backside through the thin oxide layer.....	67
Fig. 26. SEM image of devices after etching away the sacrificial oxide layer from underneath the free-standing structures (black regions represents opened backside window area with no silicon).....	68
Fig. 27. Anhydrous HF etch tool in the cleanroom.....	69
Fig. 28. (a) Device released using anhydrous HF etch process, (b) close up of one of the 900nm wide resonator cantilever.	70
Fig. 29. (a) 2 dies (for target and reference devices) are bonded to chip carrier with silver epoxy, (b) reference device was covered with metal cover to shield it from radiation.	71
Fig. 30. (a) Wire bonded die, (b) close-up view of the wire bonding.....	72
Fig. 31. (a) UV radiation experiment physical setup and, (b) CaF ₂ window that passes UV light to the target device [8].	73
Fig. 32. (a) 255nm LED source used in our project [4] and, (b) LED placed in front of the CaF ₂ window of cryostat to irradiate the device inside the vacuum chamber.	74
Fig. 33. Schematic illustration of the electrical setup for UV radiation experiment.	74
Fig. 34. ARACOR system's X-ray exposure chamber.	75
Fig. 35. Schematic diagram of X-ray radiation experiment's electrical measurement setup.	76

Fig. 36. Inside of proton radiation chamber where device was mounted for radiation exposure.....	77
Fig. 37. (a) SEM image of a resonator with extra pads to support 4-wire resistance measurement, (b) 4-wire resistance measurement setup.....	78
Fig. 38. The voltage across the base of the resonator is tracked at twice the driving frequency with the lock-in amplifier and recorded with LabView data acquisition software. The voltages are plotted against the tracking frequency where the peak voltage corresponds to the resonance frequency. A Lorentzian fit to the data is also shown.	79
Fig. 39. Pre-radiation characterization of MEMS resonator showing stable resistance and resonance frequency behavior after pump-down of 3 days where the system attained a pressure of 3.5×10^{-6} mbar at room temperature [3].	82
Fig. 40. (a) Ppm change in resistance and, (b) ppm change in resonance frequency for the exposed and shielded device under 465nm blue light radiation [13].....	83
Fig. 41. (a) Ppm change in resistance and, (b) ppm change in resonance frequency under 255nm UV light for exposed and shielded devices [13].....	84
Fig. 42. Net change in 4-terminal resistance (a) and resonance frequency (b) in exposed device due to UV radiation after subtracting the temperature effect [13].	85
Fig. 43. Comparison of ppm change in resonance frequency of resonators before, during and after UV exposure (green and red markers indicate radiation on and off times respectively) with (a) two different p-type doping concentrations and, (b) p-type and n-type of about same doping ($\approx 3.6 \times 10^{17} \text{ cm}^{-3}$) concentration.	86

Fig. 44. Ppm change in resonance frequency as a function of time during 5.6 minutes of UV radiation and subsequent annealing for (a) 8 μ m, (b) 2 μ m and (c) 1 μ m wide resonators. The vertical dotted line separates the in-situ and Annealing data.	87
Fig. 45. Pre-radiation characterization of resonance frequency showing the stability of our measurement over 10 frequency sweeps [1].....	88
Fig. 46. Frequency sweeps after different total dose of X-ray radiation showing gradual shifting of resonance frequency as the total X-ray dose increases [1].....	89
Fig. 47. Ppm change in resonance frequency as a function of total dose(left) and as a function of post-radiation anneal time (right) [1].	90
Fig. 48. (a) Ppm change in resonance frequency as a function of dose rate for (a) non-hydrogenated and, (b) hydrogenated devices [16].....	90
Fig. 49. (a) Symmetric and, (b) Asymmetric MEMS cantilever piezoresistor with dimensions [16].....	91
Fig. 50. Time evolution of in-situ and post-radiation resonance frequency shift. The radiation began at time, t = 0 and the radiation ended at different times that are indicated by markers for different dose rates [16].....	93
Fig. 51. Comparison of irradiated (at 5.4 krad/min(SiO ₂)) and un-irradiated device resonance frequency shift characteristics as a function of time under continuous pumping for 40hours [16].	93
Fig. 52. Ppm change in resonance frequency and ppm change in 4-wire resistance in a heavily doped (5.8 \times 10 ¹⁸ cm ⁻³) p-type resonator during and after radiation (red line separates the in-situ and anneal data) for 30.26krad X-ray exposure for about 33 minutes.	94

Fig. 53. Dose rate dependence of base resistivity as a function of total dose for non-hydrogenated and hydrogenated devices.	95
Fig. 54. Resistance change vs. resonance frequency change for different dose rates for both non-hydrogenated and hydrogenated (denoted by “(H)” in the legend) devices.....	96
Fig. 55. Comparison of low carrier concentration ($3.68 \times 10^{17} \text{cm}^{-3}$) p-type and ($3.62 \times 10^{17} \text{cm}^{-3}$) n-type Si resonators’ (a) resonance frequency shift and, (b) 4-wire base resistance shift under different doses of X-ray radiation.	97
Fig. 56. Width dependence of resonance frequency shift with respect to time. The vertical black line separates the insitu and annealing data.	98
Fig. 57. Frequency sweep snapshots for different fluences of proton radiation with (a) 2MeV proton and, (b) 0.8 MeV proton. The plots show that the resonance frequency decreases for high energy proton radiation while increases for low energy proton radiation [2].....	99
Fig. 58. Ppm change in resonance frequency as a function of total ionizing dose(bottom x-axis) and fluences(top x-axis) and, subsequent annealing as a function of time for (a) 2MeV proton radiation and (b) 0.8MeV proton radiation [2].....	100
Fig. 59. Resonator 2-wire base resistance decreases for both 2 MeV and 0.8 MeV proton radiation and in both cases the resistance persistently stays high during annealing [2].	102
Fig. 60. 2D model used for COMSOL simulation to find electrostatic force per unit length due to charged oxide. Charged oxide areas are marked in red.	107
Fig. 61. (a) Electrostatic force per unit length of the cantilever vs. displacement from center of the cavity, (b) extrapolation of simulation data to find the slope of force vs. displacement plot for 2nm thick oxide.....	109

Fig. 62. (a) Schematic illustration of the gas adsorption on the cantilever, (b) cantilever model used in the 2D simulation.	110
Fig.63. (a) Displacement vs. driving frequency for different amount of mass added to the cantilever, (b) Resonance frequency plotted against added monolayers of N ₂ mass. About 8 monolayers need to be adsorbed on the cantilever to cause 20 ppm change in resonance frequency.....	111
Fig. 64. Absorption depth of UV in silicon with respect to wavelength. Most of the UV is absorbed close to the surface.	116
Fig. 65. (a) Schematic diagram of UV radiated cantilever showing the direction of radiation, (b) Excess carrier concentration across the cantilever starting from top surface. Si absorbs UV light at/near the surface (up to ≈10nm depth) and generates lots of excess carriers. Surface recombination lowers the concentration at the surface (shown in inset figure).....	117
Fig. 66. Band diagram of silicon and silicon dioxide showing the relative energy difference between conduction and valence bands.	119
Fig. 67. Majority carrier concentration at the surface of p-type and n-type silicon as a function of the oxide charge density.	122
Fig 68. Parts per million (ppm) change in resistance with respect to oxide charge density.	123
Fig. 69. Normalized change in c_{44} with respect to distance from the surface plotted for different oxide charge densities that causes (a) accumulation ($\rho_{ox} = -0.5 \times 10^{13} \text{cm}^{-2}$), (b) depletion ($\rho_{ox} = 0.5 \times 10^{13} \text{cm}^{-2}$), or (c) strong inversion ($\rho_{ox} =$	

$1 \times 10^{13} \text{cm}^{-2}$) at the silicon surface for p-type silicon with doping concentration of $5.8 \times 10^{18} \text{cm}^{-3}$	126
Fig. 70. Beam dimension transformation to get a uniform and constant effective Young's modulus.....	128
Fig. 71. Dimensional dependence study of the UV radiation damage with heavily doped ($5.8 \times 10^{18} \text{cm}^{-3}$) p-type Si resonators. (a) Ppm change in resonance frequency with respect to oxide charge density for three different widths ($1 \mu\text{m}$, $2 \mu\text{m}$ and $8 \mu\text{m}$).....	129
Fig. 72. Normalized resonance frequency shift vs. beam width for p-type resonators with doping concentration of $5.8 \times 10^{18} \text{cm}^{-3}$ and a fixed oxide charge density of $8.71 \times 10^{12} \text{cm}^{-2}$	130
Fig. 73. Normalized resonance frequency shift as a function of oxide charge density for p-type Si resonators of different doping concentration.....	131
Fig. 74. Ppm change in resonance frequency as a function of excess hole concentration for several deformation potential values that span the typical range of values found in literature. Deformation potential affects the slope of the plot and larger deformation potential causes steeper slope i.e. for a given change in carrier concentration we get larger shift in frequency.	132
Fig. 75. (a) Hole mobility as a function of impurity concentration (N_s) and, (b) gradient of mobility ($d\mu_p/dN_s$) as a function of impurity concentration (N_s).	134
Fig. 76. Ppm change in resistance with respect to excess hole concentration for different percentage of trapping of positively charged hydrogen at the surface.	135
Fig. 77. Schematic illustration that shows the concept of hydrogen transport in Si and subsequent trapping in native oxide for (a) $8 \mu\text{m}$ and (b) $2 \mu\text{m}$ wide resonating cantilever	

devices. The hydrogen gets trapped at the same rate per unit surface area for both devices but the change in free hydrogen concentration per unit volume is different due to different surface-to-volume ratio. 137

Fig. 78. Excess carrier concentration as a function of beam width that shows excess free carrier decreases as the width increases. 139

Fig. 79. Comparison of experimental and theoretically predicted values of ppm change in resonance frequency for different beam widths. Our model’s prediction closely matches with the experimental values. 140

Fig. 80. Simulation results from SRIM analysis. (a) Ionization energy as a function of target depth from the exposed Si surface for 0.8MeV proton radiation and (b) Non-ionizing energy loss (NIEL) as a function of target depth from the Si surface for 2MeV proton radiation. 143

LIST OF TABLES

Table 1: Piezoresistor Dimensions.....	41
Table 2: Silicon Material Properties	47
TABLE 3: Process parameters of the PVD75 metal deposition system.....	63
TABLE 4: Parameters used for photolithography process using different resists.....	65
TABLE 5: DRIE etch parameters used to etch silicon device layer.....	66
TABLE 6: Trion metal etcher parameters used to etch photoresist and to etch SiO ₂ layer.	67
TABLE 7: Anhydrous etch process parameters.....	69
Table 8: Ball bonding parameters	72
Table 9: Resonance frequency change for different oxide thicknesses	108
Table 10: Parameter values used in photocarrier generation calculation	114
Table 11: Results of photocarrier generation calculation for different UV wavelengths	118

CHAPTER I

INTRODUCTION

1.1 Motivation

Miniaturized sensors and actuators such as accelerometers, resonators, pressure sensors, gyroscopes, and comb drives are examples of common microelectromechanical systems (MEMS). They are extensively used in terrestrial smart appliances such as smart-phones, robots, self-driving cars, virtual reality gaming devices, etc. MEMS devices are known for their small size, low weight, low power consumption and high reliability. They are replacing many bulky electro-mechanical components such as accelerometers and gyroscopes with smaller, lighter and more reliable MEMS counterparts in navigation systems (e.g. MEMS accelerometer and gyroscope was used in MARS rovers [18]). All those features make MEMS devices very attractive for space application. However, the space environment is very harsh and full of ionizing and non-ionizing radiation. For example, our atmosphere is continuously bombarded with cosmic rays consisting of charged/charge-neutral particles at a rate of about 2×10^{18} per second [19]. The atmosphere and earth's magnetic field acts as an active shield to protect us and our electronic equipment from high energy radiation letting only the lower energy secondary radiation to reach ground level. Since this protection is lacking in space, radiation damage is one of the major problems faced by any electronic equipment used in space. The Sun also emits bursts of charged particle, X-ray, ultraviolet and gamma rays during solar storms that often pose a threat to our satellite communication system. The satellites also experience secondary radiation such as Bremsstrahlung resulting from interaction of charged particle with the materials on the satellite. It is necessary to evaluate the MEMS device performance

under those extreme conditions, especially since commercial off-the-shelf MEMS devices are already being used in micro- and pico-satellites [20]. The cost of placing a low earth orbit satellite is about \$10,000 per kilogram [18]. The lifetime expectancy of conventional satellites are low (10 to 15 years) whereas the development time is high (for large satellites, 5 to 15 years) [18, 21]. There is a huge incentive for developing low-cost, high-reliability and mass-produced micro-satellites (10 to 100kg) and pico-satellites (<1kg)—since it will potentially reduce the cost of setting up satellite communication by orders of magnitude and will also reduce the development time dramatically. MEMS devices tested in space in last couple of decades further proved potential of MEMS in space application, e.g. DARPA launched a picosatellite mission on January 26, 2000 to test the performance of MEMS RF switches onboard a couple of picosats that are tethered together showing the idea of using MEMS-based picosat constellation for satellite communication [22]. The lifetime of picosats can be increased by using radiation hard components. But due to weight constraint, only a minimal amount of shielding is available to protect onboard electronic devices. So, we need to use devices that are inherently radiation hard. MEMS devices can meet this criterion since they can be properly designed to minimize the effect of radiation. To increase radiation immunity in MEMS devices, we need to understand the mechanism of radiation damage on the atomic level. The stability of MEMS devices under radiation also needs to be improved since many applications require high levels of accuracy and reliability. For example, MEMS gyroscope and accelerometers [23] for aerospace navigation application and MEMS oscillators in timing devices [24] for GPS applications require ppm level accuracy. The radiation effect on MEMS devices is an active area of research [25]. Radiation hardness of MEMS devices depends on several factors including geometry, position of dielectric, actuation method, packaging etc. and can be improved by careful design. Radiation-hard MEMS devices can also be used in other radiation environments such as in nuclear reactors or in emergency equipment for nuclear disasters like the Chernobyl disaster [26] or the Fukushima Daiichi nuclear disaster [27].

1.2 Overview of the radiation damage

There are two major types of radiation-induced damage caused by radiation: nonionizing displacement damage and ionizing radiation damage [28]. Heavy ions or high energy radiation usually causes displacement damage along with some ionizing damage of varying degree. Displacement damage causes a change in the structural properties of the exposed material such as a change in Young's modulus, material crystallinity and strength of material. Also, it creates defects in the material that reduces the carrier mobility, reduces minority carrier lifetime and reduces free carrier concentration [29]. Mechanical failure can happen easily in highly stressed small beams especially if energetic particles stop inside the beam. Sometimes displacement damage continues post-radiation for certain amount of time before annealing starts to take place [30]. The resistance of piezoresistive elements was found to be increased upon proton radiation with fluence on the order of 10^{16} cm^{-2} [31]. The change was attributed to the displacement damage caused by proton radiation. NIEL (Non-Ionizing Energy Loss) of radiation can create trap centers that can reduce majority carrier concentration and can also lower the carrier mobility due to increased scattering. Several other articles also reported NIEL induced damage in piezoresistors [32-34].

Lower energy electromagnetic radiation such as UV and x-rays usually causes ionization radiation damage. Ionizing radiation creates trapped charge in the dielectric medium that can create accumulation, depletion [32] or strong inversion on the underlying semiconductor material. TID (Total Ionizing Dose) of radiation creates electron-hole pairs that can facilitate dissociation of B-H complexes in partially passivated silicon substrate causing an increase in carrier concentration [1]. The increased carrier concentration changes the electrical properties and even the mechanical properties of the semiconductor

[1, 35]. Electrostatically actuated MEMS devices are most vulnerable to ionizing radiation due to dielectric charging caused by charge getting trapped in exposed dielectric material. Also, floating electrodes can accumulate trapped charges due to the radiation [36]. Those trapped charges modify the electric field and interferes with the electrostatic actuation of MEMS devices. Too much charge accumulation can cause micro-welding of mems actuators or latch up of MEMS switches [37]. Trapped charges often causes shift in the calibration of MEMS devices such as accelerometers [38], pressure sensors [32], comb drives [36], optical mirrors [39] and resonators [1]. Some MEMS application such as resonators in GPS system require stringent control of calibration that is on the order of tens of ppm whereas transistor-based electronics often can tolerate few percent variation in its basic characteristics [25]. It makes it imperative to study the fundamental mechanism of radiation damage to help develop strategies to design radiation immune MEMS devices.

1.3 Objectives

- Fabricate and characterize silicon MEMS resonators of different dimensions for radiation experiment.
- Explore the effect of UV, X-ray and proton radiation on resonance frequency and/or resistance of MEMS resonators before, during and after radiation.
- Investigate X-ray dose rate dependence of radiation damage.
- Develop and verify theoretical models to explain the observed shift in resonance frequency and resistance caused by different radiations.

1.4 Dissertation outline

This introduction chapter showed the significance of the radiation effect study, identified the potential of MEMS devices in space application and provides an overview of the radiation damage. In this section, a brief outline of the contents of later chapters is presented.

The literature review chapter (Chapter 2) provides the necessary background for explaining the radiation damage mechanism. Fundamental mechanisms of displacement damage and ionization damage on the atomic level are discussed along with some formulas that can be used to quantify them. Next, the radiation effect on material properties such as resistivity and elastic constant is presented in detail. The persistent photoconductivity and hydrogen passivation mechanism is addressed later in the chapter. The theory of hydrogen diffusion in silicon is also presented. Finally, a description of how the doping/carrier concentration affects the electronic contribution to the materials elastic constant is summarized from [35, 40].

Chapter 3 presents the novel design of the MEMS resonator that is used to do the radiation experiment. The significance of the asymmetric design is established from the finite element analysis and the lumped parameter modeling. Design optimization process is discussed and a comparison between the simulation and experimental result is presented.

In chapter 4, the detailed fabrication procedure of the MEMS resonator is described and the process parameters for all the fabrication steps is reported. This chapter also contains a detail description of the experimental setups used for characterizing the MEMS resonators and for doing the UV, X-ray and proton radiation tests.

Chapter 5 presents the experimental results obtained from UV, X-ray and proton radiation experiments. Resonance frequency and/or resistance of MEMS resonators was recorded before, during and after radiation for each radiation experiment. Different dose rates (5.4krad(SiO₂)/min, 10.9krad(SiO₂)/min and 30.3krad(SiO₂)/min) of X-ray were used to observe dose-rate dependence of X-ray radiation damage. Resonators of different dimensions were used to find geometry dependence for both UV and X-ray radiation damage. Protons of two different energies (0.8MeV and 2MeV) were used for proton radiation tests.

In the modeling and discussion chapter (Chapter 6), theoretical analyses of radiation damage mechanisms are presented for each types of radiation. For UV, a surface charge model is presented where native oxide charging is shown to play a major role in UV radiation damage. For X-ray, hydrogen-boron complex dissociation and hydrogen transport in silicon is discussed and a tentative model is presented as the viable mechanism for the observed X-ray radiation damage. For proton radiation, both ionization and displacement damage are shown to be responsible for the observed net effect of proton radiation.

Finally, the conclusion chapter (Chapter 7) discusses the significance and the implication of the observed radiation effect and the presented radiation damage mechanisms in the spirit of moving towards designing radiation-hard MEMS devices.

CHAPTER II

LITERATURE REVIEW

MEMS devices are inherently more radiation tolerant than microelectronics devices that uses CMOS technology. Radiation hardness of MEMS devices depends on several factors including geometry, position of dielectric, actuation method, packaging etc. and can be improved by careful design. Designing better MEMS devices for space application requires identifying the damages caused by radiation and understanding the physical mechanism behind them. Effect of radiation on material properties such as conductivity and Young's modulus often plays a significant role in causing radiation damage that affect device performance [1]. Dielectric charging is another major contributor to the radiation induced degradation. Radiation damage has been investigated in various electrostatic MEMS devices such as in comb drives [36], microshutters [41], micromirrors [39] and, RF switches [30] where dielectric charging causes the degradation. Designing radiation-hard MEMS devices require identifying the types of damage caused by radiation and understanding the physical mechanism behind them.

2.1 Displacement damage

Nonionizing displacement damage is caused by particle irradiation such as proton and neutron or high energy electromagnetic waves such as gamma rays. There is a

threshold energy (T_d) required to dislodge an atom from its position in a crystal (for silicon $T_d = 21\text{eV}$ [42]). When particle or wave with sufficient energy ($\geq T_d$) hit the target atom, it gets knocked out of its place and move to another lattice point by displacing its occupant or move to a vacancy or move to an interstitial space between atoms [43]. Energy of the incident particle has great influence on the type of interaction that takes place between the particle and the target atoms. For example, coulombic scattering dominates for radiation with less than 10MeV proton and for higher energy proton nuclear elastic interaction needs to be considered but nuclear inelastic interaction does not become significant until proton energy reaches 100MeV [44]. In nuclear inelastic collision, the momentum is not conserved since the impinging proton causes the nucleus to break down and emit nucleons of different energies. Also, some gamma rays and pions are also emitted in the process. The emitted nucleons, pions and gamma rays does not contribute to the displacement damage significantly. The residual nucleus has different atomic number than the initial state so contributes differently to subsequent defect production. As the particle flows through the target material it continues to lose energy and causes both ionizing and nonionizing damage to the material. Nonionizing energy loss (NIEL) is usually defined by the rate of energy loss per unit length (unit MeV/cm or MeVcm⁻²/gram) due to nonionizing event. It can be calculated using the following equation:

$$NIEL(E) = \frac{N}{A} \int_{\theta_{min}}^{\pi} \left(\frac{d\sigma(\theta, E)}{d\Omega} \right) T(\theta, E) L[T(\theta, E)] d\Omega \quad (1)$$

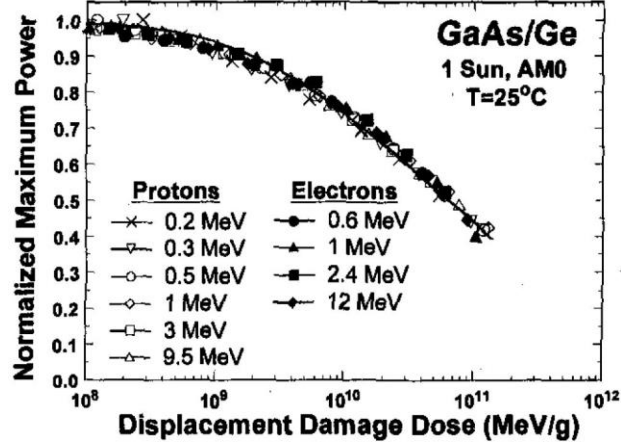


Fig. 1. Single characteristic curve obtained by plotting normalized maximum power degradation parameter of a solar cell with respect to displacement damage dose caused by proton and electron having a range of energies.

where $\frac{d\sigma(\theta, E)}{d\Omega}$ is differential cross section of target material's atomic displacement,

$T(\theta, E)$ is the average recoil energy of struck atoms, $L[T(\theta, E)]$ is Lindhard partition factor [45] that defines how much of the energy goes for nonionizing event, N is Avogadro's number, θ_{min} is the minimum angle of incidence that is able to cause atomic displacement and A is atomic mass of the target material [42]. There are different models for calculating the differential cross section that is appropriate for different proton energy ranges. For example, Rutherford differential cross section is suitable for nonrelativistic coulombic elastic collision whereas optical models are necessary for relativistic nuclear elastic scattering [46]. To account for nuclear inelastic scattering event that is relevant at higher energy radiation (e.g. >100MeV proton) requires empirical data [42]. There are some Monte Carlo simulation software such as SRIM [47] and PHITS [48] that can be used to calculate NIEL [49, 50]. Displacement damage dose, D_d is often used to characterize the radiation damage on device parameters because it generalizes the damage sustained by the device irrespective of the particle energy and type of radiation. As shown in figure Fig. 1

for GaAs/Ge solar cell's displacement damage degradation due to proton and electron radiation with several different particle energies constitutes only one characteristic curve and could have been obtained easily using only one particle with a specific energy [42, 51]. Displacement damage dose can be calculated from NIEL by using equation (2) where D_d and $NIEL$ both are functions of depth, t of the target material and ϕ is the proton fluence [52].

$$D_d(t) = 1.6 \times 10^{-8} NIEL(t) \phi \quad (2)$$

Displacement damage dose parameter provides a way to correlate the damage caused by different radiation sources and can be utilized to predict radiation damage caused by ions that are rare and expensive to investigate.

Energetic ions create lots of Frenkel defects (a vacancy and a displaced interstitial atom) on their track while traversing across the target material. Usually the density of Frenkel defects at the radiation site is very high and both the vacancy and the interstitial atom associated with them are extremely mobile. That leads to annihilation of about 95% of the defects right away. Some vacancies get occupied by the initially inactive interstitial impurity atoms. Remaining vacancies are electrically very active and create defect complexes such as E center (by interacting with n-type dopant atoms) and A center (by interacting with O₂ impurities) or create other vacancies such as divacancies [53]. Those defect complexes act as recombination and charge trapping centers. As a result, carrier concentration and minority carrier lifetime get reduced. In the charged state, those trap centers scatter carriers resulting in reduction of carrier mobility. Divacancies in Si forms mid-band trap states situated ≈ 0.35 eV above valence band. With high enough radiation damage electronic behavior of Si approaches their intrinsic counterpart irrespective of their

initial doping level due to those divacancies. It is reported in [49] that diffusion length damage coefficient (in solar cells) varies differently with respect to NIEL in n-type and p-type semiconductors leading to the conclusion that different defect complexes might be dominant in n-type and p-type semiconductors.

2.2 Ionization damage

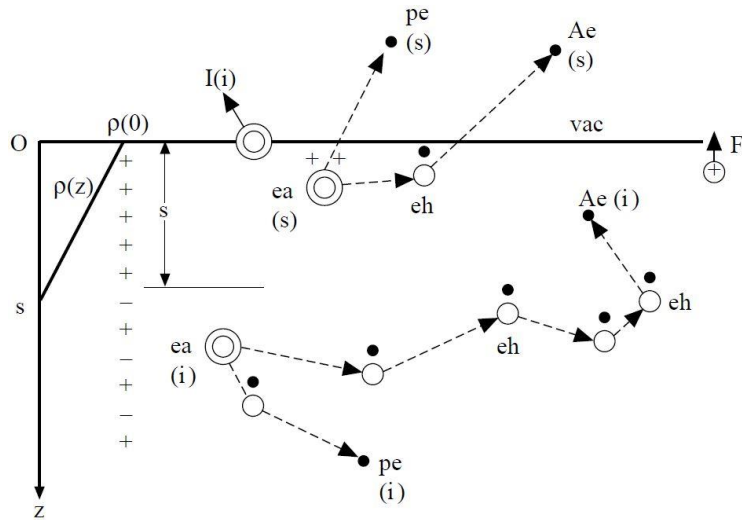


Fig. 2. Ionization process during electromagnetic radiation where pe denotes photoelectrons, ea denotes excited atom, eh denotes electron hole pairs, Ae denotes Auger electron, I denotes ions, F denotes electric field, s denotes escape length and $\rho(z)$ shows charge density profile with respect to depth from the surface [15].

Insulators used on the MEMS devices are particularly vulnerable to ionizing radiation damage since in insulators charges created due to radiation cannot easily redistribute themselves to return to the initial equilibrium state [15]. An illustration of ionization process during radiation is shown in Fig. 2. When electromagnetic waves such as x-ray and gamma ray impinge on MEMS devices, it engages in inelastic collision with the atoms of the constituting material. If the impinged photon has sufficient energy, the excited atom (ea) emits photoelectrons (pe). Within 10^{-15} s, the atom goes through de-

excitation that results in emission of photon (fluorescence) or emission of auger electron. The probability of auger electron emission is a function of energy of the radiation. At lower energy ($h\nu < 10\text{keV}$) auger electron emission dominates while at higher energies de-excitation by photon emission is preferred. The emitted photoelectrons and auger electrons travels through the material and create electron-hole pairs. If the generated photoelectrons and auger electrons arrives close to the surface, within the electron escape length (s) for the material, they get emitted from the material surface to the surrounding medium. As a result, the surface gets positively charged. It is interesting to note that the escape length, s , is larger than inelastic mean free path (IMFP) of electrons since it is argued that a major portion of the emitted electrons are secondary electrons [15]. As the radiation continues more electrons get emitted and charge builds up at the surface with the charge density given by equation (3). The charge density profile with depth (z) is shown on the left side of Fig. 2.

$$\rho(z) = \rho(0)\left[1 - \left(\frac{z}{s}\right)\right] \quad (3)$$

The flow of electron out of the material surface can be defined as emission current, I_e . Some mobile ions also move at the interface constituting current $I(i^+)$. The accumulated positive charge at the surface creates an electric potential that forces a current, I_s , to flow from the substrate that is given by,

$$I_s = I_e - \left(\frac{\partial Q_c}{\partial t}\right) - I(i^+) \quad (4)$$

where $\left(\frac{\partial Q_c}{\partial t}\right)$ is the rate of total charge accumulation in the sample. At the beginning, $I_s = 0$ due to the absence of electric field, so all the emitted electron accounts for charge

buildup, $\left(\frac{\partial Q_c}{\partial t}\right) \approx I_e$. But when radiation continues for long time ($t \approx \infty$), I_s equals I_e meaning that the lost electrons are replenished by the substrate current and charge build up ceases i.e. $\left(\frac{\partial Q_c}{\partial t}\right) = 0$. The reason that metals with defined potential are immune to ionization damage is that any surface charge get readily neutralized by the substrate current, I_s . But in insulators poor DC conductivity gives rise to significant amount of charge buildup and after radiation is turned off it discharges following a form similar to discharge of a high resistance RC circuit given by the following equation,

$$Q_c(t) = Q_c(t_i)e^{-t/\tau} \quad (5)$$

Time constant, $\tau = \epsilon/\gamma$ where γ is the DC conductivity of the dielectric material. The surrounding medium has significant impact on the amount of charge that can accumulate on the surface. For example, at higher pressures the gases can get ionized by the radiation and get adsorbed on the surface neutralizing some of the charges. That will also reduce the electric field that will result in reduction of the mobile ion movement [15]. Effect of coating the dielectric surface with metals has been investigated [54]. It is found that the metal injects electrons into the insulator that changes the charge distribution of the insulator. The amount of electron injection from the metal found to depend on several factors including energy of the radiation, atomic number of the insulator and atomic density of the insulator.

At very high radiation energies, Compton scattering dominates as the energy loss mechanism. It generates high energy Compton electrons that often create defects in the material. Since free electron energy is increased, the escape length increases that leads to

increased charged volume. But the absorption coefficient of the radiation decreases with high photon energy of the radiation that reduces the rate of charge creation.

2.3 Material properties affected by radiation

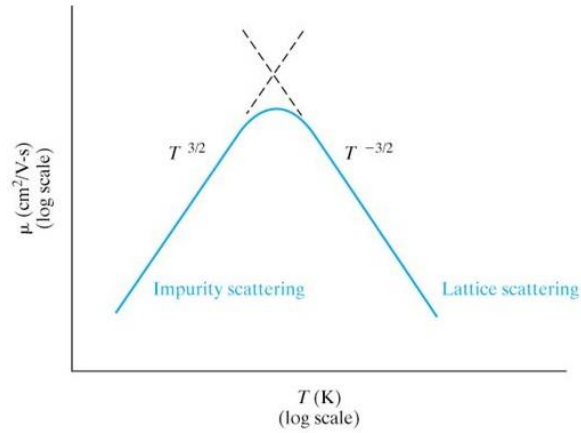
To understand the effect of radiation on MEMS device performance, we need to find the material properties that dictates the MEMS behavior and how radiation alter those material properties. For example, piezoresistor sensing elements depend heavily on the resistance and piezoresistive coefficient of the semiconductor and any significant shift in those material properties will cause change in calibration or change in sensitivity of the piezoresistor. Similarly, MEMS resonators are susceptible to the change in Young's modulus since it defines the natural frequency of the oscillating structure. Sometimes change in resistance and young's modulus can be interrelated in a way that they can affect each other. In the following sections, we will look at the basic mechanism of how radiation affect those two material properties and how they can be correlated.

2.3.1. Effect on resistivity

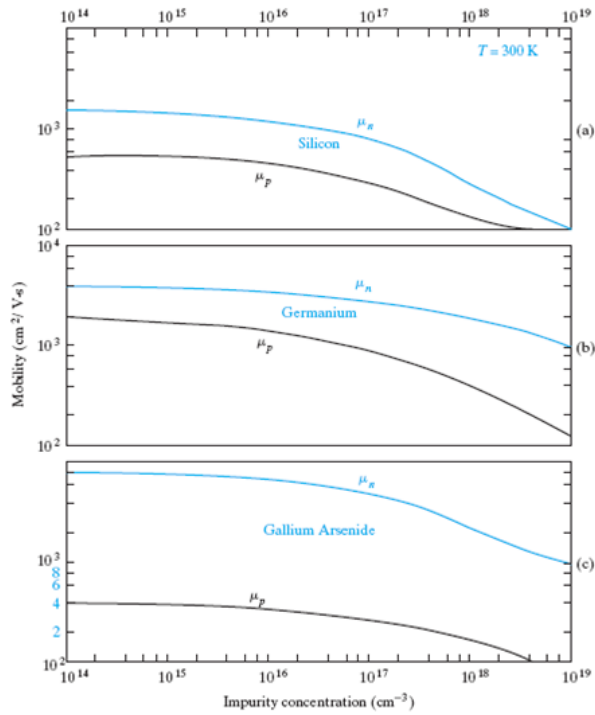
One of the salient feature of semiconductor is that resistivity can be controlled by changing the doping level. In intrinsic semiconductor, only the thermally generated electron-hole pairs ($\approx 10^{10} \text{cm}^{-3}$ at 300K) contributes to charge transport and as the temperature increases more electron-hole pair get generated that lowers the resistance. That continues until electron-hole pair generation reaches saturation and mobility reduction due to lattice scattering become dominant. Equation (6) shows the temperature dependence of

intrinsic carrier concentration where E_g is band gap energy and, m_n^* and m_p^* are density-of-states effective masses of electron and hole respectively [5].

$$n_i(T) = 2 \left(\frac{2\pi kT}{h^2} \right)^{\frac{3}{2}} (m_n^* m_p^*)^{3/4} e^{-E_g/2kT} \quad (6)$$



(a)



(b)

Fig. 3. (a) Mobility vs. temperature plot showing the dominant scattering mechanism at two temperature ranges [5], (b) Impurity concentration vs. mobility at room temperature for three different semiconductors [5].

In doped semiconductors charge transfer is dominated by the carriers introduced by the dopant atoms and it takes only a little thermal energy to free those carriers. So, change

in resistance with temperature is not straightforward rather it depends on both mobility and carrier concentration at any given temperature. At low temperature, mobility is dominated by the amount of impurity scattering since the carriers has low thermal energy at low temperature and get easily scattered by any charged ion residing in any defects or impurities. On the contrary, at high temperature the momentum of the charge carriers is higher so get less influenced by the impurities but get obstructed frequently by the higher lattice vibration at this elevated temperature i.e. lattice scattering dominates at high temperature. Fig. 3(a) shows how mobility changes with temperature and the dominant scattering mechanism at that temperature. Although at high temperature carrier mobility should mainly be affected by lattice scattering, impurity scattering seems to become significant at high doping levels as shown in Figure Fig. 3(b). So, the two parameters mobility and carrier concentration that determines the resistivity of a semiconductor are interrelated and both varies with temperature. Equation (7) can be used to calculate resistivity of a semiconductor where n is electron concentration, p is hole concentration, μ_n is electron mobility and μ_p is hole mobility [55].

$$\rho = \frac{1}{qn\mu_n + qp\mu_p} \quad (7)$$

Another way of generating electron-hole pairs is to radiate them with electromagnetic waves such as visible light, UV or X-ray. The impinged photon gets absorbed by atoms that energize electrons on the outer shells and excited electrons get transferred to higher energy states leaving holes behind. The excitation follows by de-excitation that results in photon emission or heat release in the form of lattice vibration. So, radiation causes temperature to rise in the radiated sample. Also, it changes the free

carrier concentration by generating electron-hole pairs, creating defects and breaking bonds (e.g. breaking B-H complexes). Since both mobility and carrier concentration get affected by radiation, the resulting change in resistivity is determined by several factors including doping level and operating temperature. Sometimes photogenerated carriers get trapped in the defect states or trap centers especially in the interface states or adjacent dielectric medium causing a persistent change in carrier concentration with long recovery time.

2.3.1.1. Persistent photoconductivity

Incident photon generates electron-hole pairs that usually lowers the resistance of an illuminated sample. This temporary increase in conductivity is termed photoconductivity and conductivity falls back to its original value rapidly as the light is turned off if there is no mechanism preventing the recombination of extra carriers. One way of preventing the recombination of excess carriers is to separate them spatially and/or trapping one of the carrier. In that case, the photoconductivity can persist for a long time after the light is turned off leading to persistent photoconductivity (PPC). The charge separation can happen due to a number of factors such as surface and interface traps, p-n junctions, inhomogeneity in material composition and non-uniformity in dopant distribution [56]. Macroscopic potential barrier at the interface is reported to cause charge separation in n-GaAs sample grown on semi-insulating Cr-doped GaAs substrate [57]. Both increase in carrier density and widening of conduction path (by neutralizing space charge near the interface) increased conductivity on the film during illumination. So, excess electron sheet density $\Delta(nd)$ can be used as a parameter for capturing both change in electron density (n) and change in conduction path width (d) effect on photoconductivity.

The excess electron sheet density $\Delta(nd)$ is related to total photon dose (Q) by the following equation,

$$\Delta(nd)(Q) = ZL \ln(1 + Q/Q_0) \quad (8)$$

where $Q_0 = ZL\gamma^{-1}$ and Z is the deep trap density. Parameters L and γ represents mean free path of holes and carrier generation efficiency of photon at the interface, respectively. Another factor influencing conductivity was enhanced mobility due to screening of impurity ions that reduced carrier scattering. After photoexcitation is removed, logarithmic decay of photoconductivity was observed [56].

Although PPC is relatively common in compound semiconductors due to their high defect density, it was also observed in Silicon sample [58] where Sulfur has been diffused in Si to create n-p junction near the surface. The junction separated photogenerated carriers and Sulfur captured electrons that helped to prevent recombination. Light doping of Si and low temperature ($\approx 45\text{K}$) helped to make PPC stronger. At that low temperature, impurity scattering dominated the mobility and neutralization of impurity ions by captured electrons helped increase the mobility.

Decay of PPC is often non-exponential and in some cases exist for a really long time making it practically time-independent [56, 59]. Queisser *et al.* proposed a theoretical model to explain the decay kinetics of PPC [56]. The model assumes an n-type film grown on insulating substrate with high trap density. A general solution for decay of excess electron sheet density is found to be,

$$\Delta(nd)(x, t) = \int_0^\infty p(x, t = 0) \exp\left[-\left(\frac{t}{\tau_0}\right) \exp\left(-\frac{2x}{a}\right)\right] dx \quad (9)$$

where $p(x, t = 0)$ is the initial hole density profile at moment of termination of photoexcitation ($t = 0$), τ_0 is recombination lifetime and a is Bohr radius of electron. This general solution can be solved numerically for different trapped-hole distribution at $t = 0$. An alternative approach to simplify the general solution has been suggested where an assumption has been made about the time evolution of trapped-hole profile called sharp-front assumption [56]. After implementing this simplifying assumption equation (9) becomes,

$$\Delta_s(nd)(x, t) = \int_{x_s}^{\infty} p(x, t = 0) dx \quad (10)$$

where position of the sharp front (x_s) is given by,

$$x_s(t) = \frac{1}{2} a \ln\left(1 + \left(\frac{t}{\tau_0}\right)\right). \quad (11)$$

It is found that the assumption holds well in many practical cases, and usually only introduces less than 2% error in the calculation. A critical value of hole capturing trap density (Z_c) was suggested that predicts whether a certain sample will show PPC and is given by,

$$Z_c = \frac{\gamma Q}{a} \quad (12)$$

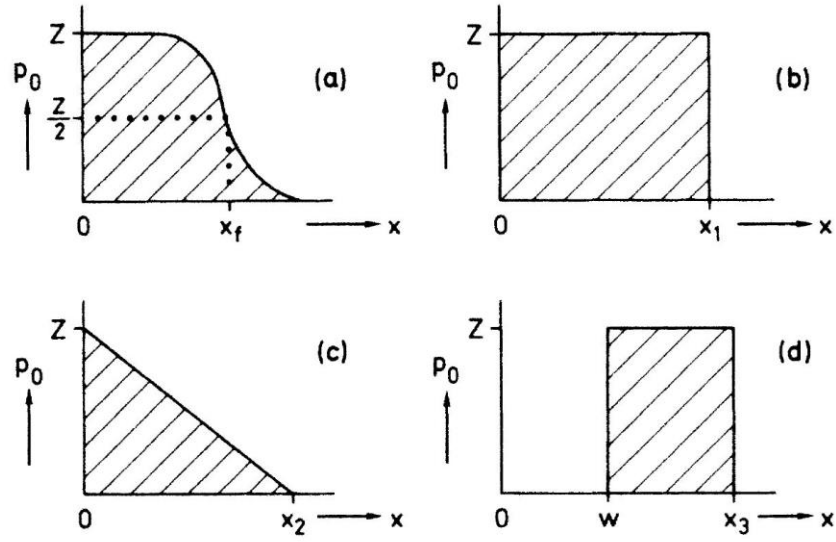


Fig. 4. (a) Fermi distribution of trapped-hole density usually found in substrates with moderate amount of trap states, (b) simplified rectangular distribution, (c) simplified triangular distribution, (d) shifted rectangular distribution.

For a sample to show persistence of photoconductivity it must have a volume density of trap states (Z) less than Z_c . Otherwise the separation between the carriers will be too small to survive beyond recombination lifetime (τ_0) which is very small (e.g. $\approx 10^{-9}$ s for GaAs).

Although for substrates with moderate amount of trap states Fermi distribution (Fig. 4(a)) is more appropriate for trapped-hole density distribution, it can still be approximated by rectangular or triangular distribution with reasonable accuracy to simplify calculation of sheet density of excess electrons given by equation (10). Few possible distributions for trapped-hole density is shown in Fig. 4. The following equations shows excess electron sheet density for rectangular (equation (13)) and triangular (equation

(14)) trapped-hole distribution.

For rectangular distribution:

$$\Delta(nd) = Zx_1 - \frac{1}{2}aZ \ln\left[1 + \left(\frac{t}{\tau_0}\right)\right] \quad (13)$$

For triangular distribution:

$$\begin{aligned} \Delta(nd) = K - \frac{1}{2}Za \ln\left[1 + \left(\frac{t}{\tau_0}\right)\right] \\ + Z^2(4K)^{-1} \left(\frac{a}{2}\right)^2 (\ln[1 + \left(\frac{t}{\tau_0}\right)])^2 \end{aligned} \quad (14)$$

where K represents $\Delta(nd)$ at $t = 0$.

Another distribution named shifted rectangular distribution (Fig. 4(d)) is found in semiconductors that has a charge-free buffer layer (i.e. traps-free region) between the substrate and the top conducting film. The buffer layer expands the distance between the separated holes and electrons and increases the recombination lifetime. The effective recombination lifetime is given by $\tau_0 \exp\left(\frac{2\omega}{a}\right)$ in this case.

There are few limitations to the model. The model assumes trapped charges are fixed in space which is only true at very low temperatures. At higher temperatures, some trapped charges get released and move towards the interface where they recombine with electrons. As a result, recombination gets accelerated. There are other methods that can accelerate recombination such as tunneling, hopping or impurity band conduction. Those are also not included in this model.

The model predicts that larger exposure time will increase PPC since separated holes will move deeper into the substrate and will take longer time to recombine. So essentially different photon doses will produce similar decay profile except a parallel shift due to larger photoconductivity and longer persistence [56].

2.3.1.2. Hydrogen passivation

It is well-known that hydrogen can passivate impurities in crystalline silicon and lots of research has been done to find out the passivation mechanism. Pankove et al. [60] first observed this phenomena in 1983, where sixfold increase in silicon resistivity was observed after hydrogenation and the change in resistance was attributed to hydrogen passivation of boron impurities. Next year his group published more results that includes SIMS profile of hydrogen and boron in hydrogenated silicon and it shows spatial correlation of their concentration [61]. It corroborates the assumption of boron passivation by hydrogen. With infrared spectroscopy, an absorption band was observed at 1875 cm^{-1} and it was attributed to Si-H stretching mode. Although previous experiments show that Si-H stretching modes tend to be higher (2000 cm^{-1}), it was argued that the presence of Boron lowered the frequency due to change in force constant and due to local fields caused by dielectric cavity in crystals. So according to Pankove, the passivation of boron takes place due to bond breaking between the Boron and one of its neighboring Silicon where the bond is replaced by Si-H bond leaving Boron bonded with only three Si atoms. Raman spectroscopy of boron doped silicon was conducted by Stutzmann [62] and it was found that new hydrogen vibration related peaks (e.g. 1880 cm^{-1} and 650 cm^{-1}) appear after hydrogenation. He argued that 650 cm^{-1} peak corresponds to B-H bond vibration. In

constast with Pancove’s hypothesis, Stutzmann thinks the hydrogen gets bonded with boron instead of silicon and the bond is an ionic bond. Fano broadening was also observed in the Raman spectrum that indicates reduction in free carrier density. IR (Infrared) reflectance spectroscopy further confirmed the free carrier reduction by characteristic plasma edge shifting. However, hydrogenation was found to be a reversible process where annealing the hydrogenated sample at about 200⁰C de-passivated the impurities [62]. Chantre et al. reported that commercial silicon wafers have about 1 μ m deep passivated region on the surface of the wafer [63]. They suspect the hydrogen was introduced inadvertently to the wafers during the polishing step.

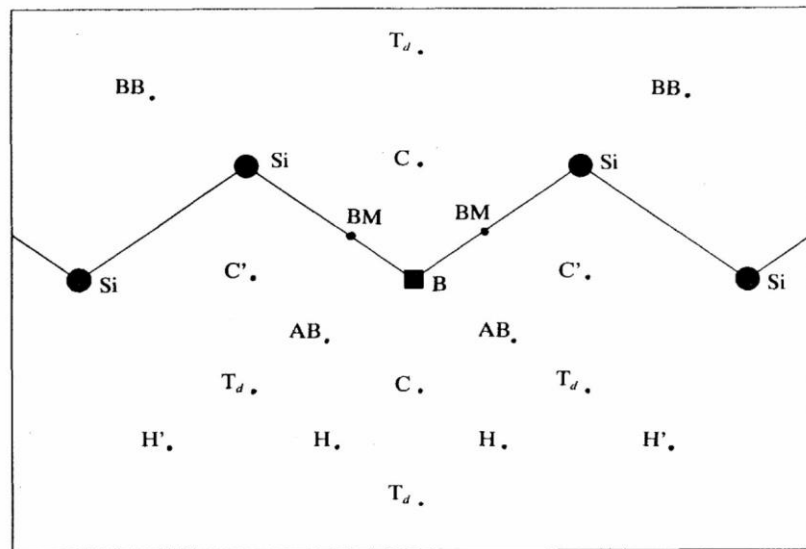


Fig. 5. Lattice positions in crystalline silicon at (110) plane showing BB (backbonding) site, AB (antibonding) site, Bond minimum (BM) site and tetrahedral (T_d) interstitial site and hexagonal (H and H') interstitial site [12].

Few other possible mechanisms of hydrogen passivation were proposed as well. For example, Assali et al. [64] suggested that hydrogen bonds with Boron covalently while residing in the interstitial antibonding site in the silicon crystal. According to the model,

mobile interstitial hydrogen moves in the crystal through tetrahedral interstitial lattice site (T_d site) and when it comes close to Boron impurity, it forms $Si:B_sH_i$ complex that de-passivates Boron. Another group, Bonapasta et al. [65] proposed Si-H-B three-center bond formation as the mechanism of boron passivation. Equilibrium position of hydrogen atom in Si crystal was also a topic of significant debate. For example, Baranowski [66] et al. suggested hydrogen occupy backbonding site (BB), Assali et al. [64] claimed hydrogen occupy antibonding site (AB) while Bonapasta et al. [65] calculated that hydrogen will reside near bond center of Si-B bond. Denteneer et al. [12] used first-principle calculation to find energy surface of H in silicon crystal and concluded that equilibrium hydrogen resides at bond minimum (BM) site near the center of Si-B bond. Fig. 5 shows the lattice sites that are suggested as equilibrium positions of the hydrogen atom. Denteneer et al. also showed that there are four equivalent BM sites around the boron atom and hydrogen atoms can easily roam across those BM sites since there are only 0.2eV energy barrier between those sites.

At temperature above 150⁰C boron-hydrogen complex starts to dissociate [12]. The following hydrogenation reaction occurs in boron doped p-type silicon where hydrogen acts as a donor with a donor level near the midgap (0.52eV from conduction band of Si) [67].



Hydrogen can also passivate n-type impurities by forming acceptor-hydrogen complex [67, 68]. In n-type Si, hydrogen acts as an acceptor with an energy level 0.06eV below conduction band. For example, the following passivation-depassivation reaction was suggested for phosphorus doped n-type silicon [67].



So, there are three possible charge states of hydrogen in silicon namely H^+ , H^- and H^0 . Preferred charge state of hydrogen is H^+ and H^- in p-type and n-type silicon respectively. However, the equilibrium concentration of H^+ , H^- and H^0 depends on the fermi level of the silicon as shown in equations (19) and (20) for p-type and n-type silicon respectively [67].

$$\frac{[H^+]}{[H^0]} = \exp\left[\frac{E_d - E_F}{kT}\right] \quad (19)$$

$$\frac{[H^-]}{[H^0]} = \exp\left[\frac{E_F - E_a}{kT}\right] \quad (20)$$

The diffusion coefficient of hydrogen in silicon depends on its charge state. H^+ has the highest diffusivity while H^0 has the lowest [67]. A common method of hydrogenation is to expose the silicon to deuterium plasma [11, 14, 67]. To avoid surface damage sometimes remote plasma is used instead of direct plasma exposure [69, 70]. Deuterium is easier to detect during Secondary Ion Mass Spectroscopy (SIMS). After hydrogenation, experimental hydrogen profile shows smaller penetration depth than theoretical prediction using laws of diffusion since hydrogens get trapped at defects and impurities [11]. In lightly

doped silicon, hydrogen dimer H_2 formation from hydrogen monomers dominate and the total concentration of hydrogen in lightly doped silicon can be approximated by concentration of hydrogen dimers given by [11],

$$[H_2] = \frac{36\pi DR[H_0]^2 t}{(4\pi R[H_0]x + \sqrt{3})^4} \quad (21)$$

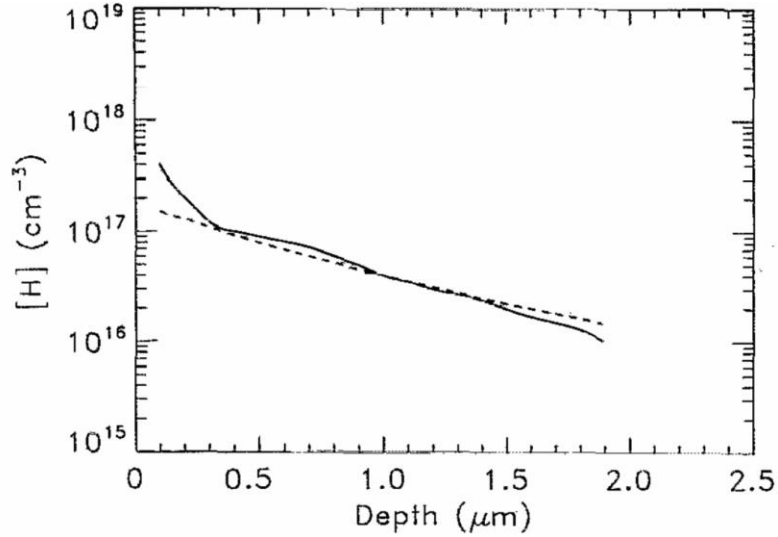


Fig. 6. Experimental (solid line) and calculated (dashed line) hydrogen concentration profile in high resistivity (100 Ωcm) silicon after hydrogenation for 1h at 125 $^{\circ}\text{C}$ using deuterium plasma [11].

where $[H_0]$ is surface concentration of hydrogen monomers, R is the capture radius, D is the diffusion coefficient of hydrogen in silicon, x is depth from the surface and t is the time of hydrogenation. Hydrogen profile calculated using equation (21) matches closely with the experimental data (obtained from SIMS) except at the surface region (Fig. 6). The concentration of H^+ and H^- is negligible in lightly doped silicon if hole concentration (p) is less than ten times of intrinsic carrier concentration (n_i) [14]. For lightly doped p-type silicon, overall diffusion coefficient (D) of hydrogen (both H^+ and H^0 species) is given by,

$$D = D^+ + \frac{D^0 p_d}{p} \quad (22)$$

where D^+ is diffusion coefficient of H^+ species, p_d is the estimated hole concentration if fermi level was aligned with the hydrogen donor level (E_d) and D^0 is the diffusion coefficient of H^0 species. D^0 and p_d can be calculated from equation (23) and equation (24) respectively.

$$D^0 = (0.015 \text{ cm}^2 \text{ s}^{-1}) \exp\left(\frac{-0.14 \text{ eV}}{kT}\right) \quad (23)$$

$$p_d = 2.3 * 10^{16} (T)^{\frac{3}{2}} \exp\left(\frac{-0.95 \text{ eV}}{kT}\right) \quad (24)$$

For highly doped silicon, mass action law can be used to find the relative concentration of non-passivated boron ($[B]$) and hydrogen-boron complex ($[HB]$) as shown in equation .

$$\frac{C^+[B]}{[HB]} = K \quad (25)$$

where C^+ is the concentration of H^+ species and K is dissociation constant at equilibrium that is given by equation (26) as a function of lattice site density (ρ) and binding energy (E) of hydrogen-boron complex.

$$K = \left(\frac{\rho}{2}\right) \exp\left(\frac{-E}{kT}\right) \quad (26)$$

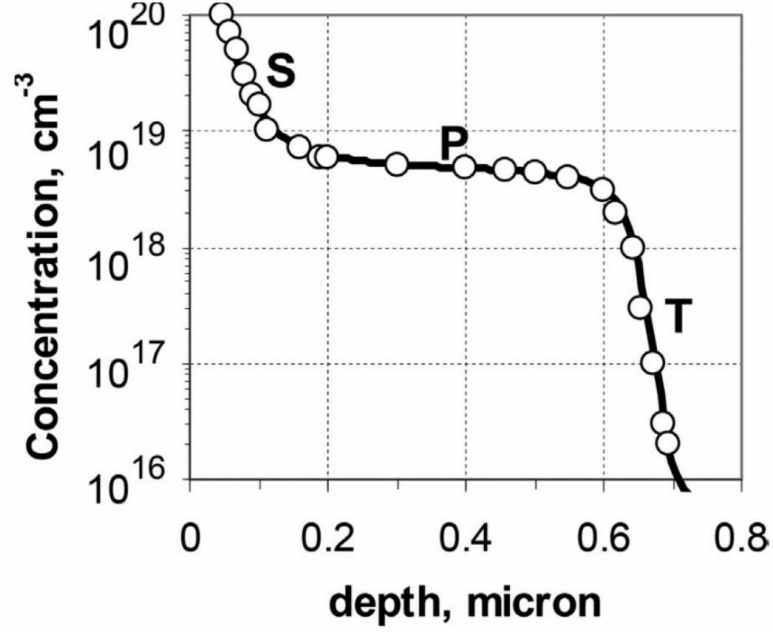


Fig. 7. Experimental (circles) and calculated (solid line) hydrogen concentration profile in highly doped (Boron concentration $5 * 10^{18} \text{ cm}^{-3}$) p-type silicon after hydrogenation for 30min at 150°C using deuterium plasma [14].

Time evolution of total hydrogen concentration (C_t) can be found by solving the following expression [14],

$$\frac{\partial C_t}{\partial t} = \frac{\partial}{\partial z} \left[D^+ p \frac{\partial}{\partial z} \left(\frac{C^+}{p} \right) \right] \quad (27)$$

where z is the depth from the surface and hole concentration p is given by,

$$p = \frac{N_B K}{(C^+ + K)} - C^+ \quad (28)$$

where N_B is the concentration of boron in silicon. The surface concentration of neutral hydrogen species denoted by $C^0(0)$ is constant for fixed gas ambient, and surface concentration of H^+ species denoted by $C^+(0)$ can be expressed as,

$$C^+(0) = \left(\frac{K C^0(0)}{p_d} \right)^{\frac{1}{2}} N_B^{\frac{1}{2}} \quad (29)$$

The depth of passivated region (L) is given by,

$$L = \left[\frac{4D^+ C^+(0)t}{N_B} \right]^{1/2} \quad (30)$$

Fig. 7 shows the experimentally observed hydrogen concentration profile (circles) and fitted computed profile (solid line). The profile has three regions namely surface (S), quasi-plateau (P) and tail (T) region. At the surface (S) region, in-diffusion of monomeric and dimeric hydrogen species dominate similar to the case of lightly doped silicon mentioned earlier. On the other hand, in plateau (P) and tail (T) region diffusion of H^+ species dominates in p-type silicon, and the profile can be approximated by numerical solution of equation (27).

2.3.2. Effect on elastic constant

Elastic modulus is a fundamental mechanical property of material and it is a measure of the stiffness of that material. Radiation can change elastic constant of a semiconductor by displacing its constituent atoms that introduces defects in the crystals or by changing its free carrier concentration that strains the material. Only high energy gamma radiation or heavy particle radiation like proton radiation can cause elastic constant change by the former process (called displacement damage) but the latter process can occur for any types of radiation with sufficient energy. There are several other ways radiation can change elastic constant, but the dominant mechanism is different for different circumstances. For example, radiation induced changes in free carrier concentration can change elastic constant of semiconductor known as electronic effect on elastic constant [71]. Also, charge separation at the surface can create a local electric field at the surface

and large electric field can change elastic constant [72]. Temperature change can also change elastic constant [73]. In this section, we will discuss the electronic effect on elastic constant.

We will first discuss deformation potential in a strained crystal. Then, we will find the electronic contribution to the change in free energy due to strain and compare it with the elastic energy: to calculate the change in elastic constant due to electronic effect.

Shockley and Bardeen[74] reported that energy gap (E_g) changes if strain is introduced on semiconductors e.g. Silicon, Germanium and Tellurium. Although non-axial strains cancel each other due to symmetry; uniaxial strains—that causes dilation of crystal—contributes to band gap shift. They measured band gap shift from the observed change in mobility in strained semiconductors and found good agreement with previous band gap measurements conducted in strained sample.

In another article, Bardeen and Shockley [75] proposed that the shift in band gap caused by strain can be modeled as scattering of charges by long wavelength acoustic phonon. The acoustic wave produces an effective electrostatic potential named deformation potential. Wave function of carriers at band edges can be derived for strained crystal by adding deformation potential to the existing periodic lattice potential of the crystal.

Conduction band and valence band energies in a strained crystal with small momentum P can be approximated by,

$$E(p, \epsilon_{ij}) = E_0(P) + E_1\Delta \quad (31)$$

where $\Delta = \epsilon_{11} + \epsilon_{22} + \epsilon_{33}$, is the stress induced dilation of the crystal: effect of other component of stress cancels out. The change in effective mass with strain is usually negligible. $E_0(P)$ is the energy for unstrained crystal. The deformation potential is defined as,

$$E = E_1 \Delta(r) \quad (32)$$

They evaluated a matrix element, M that captures electron and lattice phonon interaction given by,

$$|M|^2 = E_1^2 \langle \Delta^2 \rangle_{Av} \quad (33)$$

where $\langle \Delta^2 \rangle_{Av}$ is the average dilation of the strain induced acoustic wave.

The mobility of the strained crystal can be calculated using the following formula:

$$\mu = \left[\frac{(8\pi)^{\frac{1}{2}} \hbar^4 c_{ii}}{2E_1^2 (m^*)^{\frac{5}{2}} k_0^2} \right] T^{-\frac{3}{2}} \quad (34)$$

where c_{ii} is the elastic constant of the acoustic phonon and m^* is the free electron mass.

Keyes [71] proposed that electronic states (at band extrema) of a crystal contributes to the total free energy of that crystal and when crystal is strained, free energy changes due to shift of band edges. From thermodynamics perspective, elastic constant is the rate of change of free energy. So electronic states influence the elastic property of a semiconductor. Keyes found that shift in band edges have significant influence on the elastic properties only if two or more bands have high density of states at their fermi energy level: usually true for moderate to highly doped semiconductors.

The electronic contribution to the elastic constant change comes from the free energy component given by equation (35) for the nondegenerate semiconductors.

$$F_{el} = \frac{1}{4} \frac{\sum \sum (W^{(i)} - W^{(j)})^2 n^{(i)} n^{(j)}}{kT \sum n^{(i)}} \quad (35)$$

where $W^{(i)}$ is the shift of band edge energy due to strain and $n^{(i)}$ is the total number of electron in band (i) given by,

$$n^{(i)} = \int_{-\infty}^{\infty} N^{(i)}(E) f(E, \zeta) dE \quad (36)$$

where $f(E, \zeta)$ is the probability of occupancy of a state of energy E and ζ is the fermi energy.

The shift in energy $W^{(i)}$ can be expressed in terms of deformation potential

$$W^{(i)} = \Xi^{(i)} : \boldsymbol{\varepsilon} \quad (37)$$

where $\boldsymbol{\varepsilon}$ is the stain tensor. Deformation potential $\Xi^{(i)}$ can be written as:

$$\Xi^{(i)} = \Xi_d \mathbf{1} + \Xi_u \mathbf{a}^{(i)} \mathbf{a}^{(i)} \quad (38)$$

where $\mathbf{a}^{(i)}$ unit vector lies along the direction of rotational symmetry axis; $\mathbf{1}$ is identity tensor; $\Xi_d \equiv \Xi_x$ i.e. deformation potential constant in x direction: in a cartesian coordinate where z direction is along the axis of valley (i); and $\Xi_u \equiv \Xi_z - \Xi_x$.

Substituting terms of equation (35) using Fermi-Dirac statistics and applying deformation potential concept, electronic contribution of free energy can be rewritten as:

$$F_{el} = -(v/2) \left(\frac{2}{\pi^{1/2}} \right) N_c F_{1/2}'(\eta) \Xi_u^2 J(\boldsymbol{\varepsilon}, \boldsymbol{\varepsilon}) \quad (39)$$

where N_c is density of states at conduction band, $F_{1/2}$ is 1/2 order Fermi-Dirac integral, $J(\boldsymbol{\varepsilon}, \boldsymbol{\varepsilon})$ is a function of strain tensor given by:

$$J(\boldsymbol{\varepsilon}, \boldsymbol{\varepsilon}) = \frac{4}{9}(\varepsilon_{xy}^2 + \varepsilon_{yz}^2 + \varepsilon_{zx}^2), \quad \text{for Ge } (< 111 > \text{ valleys}) \quad (40)$$

$$J(\boldsymbol{\varepsilon}, \boldsymbol{\varepsilon}) = \frac{2}{9}(\varepsilon_{xx}^2 + \varepsilon_{yy}^2 + \varepsilon_{zz}^2 - \varepsilon_{xx}\varepsilon_{yy} - \varepsilon_{yy}\varepsilon_{zz} - \varepsilon_{zz}\varepsilon_{xx}), \quad (41)$$

for Si (< 001 > valleys)

When stress is applied to strain the crystal, it does work on the crystal. The work raises the free energy. Elastic energy contribution to the free energy is expanded up to second order of strain to get equation (42).

$$F_g = \frac{1}{2}[B(\text{tr } \boldsymbol{\varepsilon})^2 + \frac{4}{3}c'(\varepsilon_{xx}^2 + \varepsilon_{yy}^2 + \varepsilon_{zz}^2 - \varepsilon_{xx}\varepsilon_{yy} - \varepsilon_{yy}\varepsilon_{zz} - \varepsilon_{zz}\varepsilon_{xx}) + 4c_{44}(\varepsilon_{xy}^2 + \varepsilon_{yz}^2 + \varepsilon_{zx}^2)] \quad (42)$$

where B is bulk modulus and c' is shear elastic constant given by,

$$c' = \frac{1}{2}(c_{11} - c_{12}) \quad (43)$$

Comparing equation (42) with equation (39), we find the electronic contribution to elastic constant change.

$$\Delta c_{44} = -\frac{4}{9}\left(\frac{2}{\pi^{\frac{1}{2}}}\right)N_c F_{\frac{1}{2}}'(\eta)\mathcal{E}_u^2, \quad \text{for Ge} \quad (44)$$

$$\Delta c' = -\left(\frac{2}{\pi^{\frac{1}{2}}}\right)N_c F_{\frac{1}{2}}'(\eta)\mathcal{E}_u^2, \quad \text{for Si} \quad (45)$$

Deformation potential constant \mathcal{E}_u reported to be 16eV and 9eV for germanium and silicon respectively [71]. Relationship of electron concentration and change in elastic constant can be shown directly using the following relations

$$n^{(i)} = \left(\frac{2}{\pi^2}\right) N_c F_{\frac{1}{2}}(\eta) \quad (46)$$

$$N = \sum n^{(i)} \quad (47)$$

where N is total number of electron in conduction band. Equation (44) and (45) can be rewritten as,

$$\Delta c_{44} = -\frac{4}{3} \left(\frac{4\pi}{3}\right)^{\frac{2}{3}} \left(\frac{m^* \mathcal{E}_u^2}{h^2}\right) N^{\frac{1}{3}} L_2\left(\frac{T}{T_D}\right), \quad \text{for } n\text{-type Ge} \quad (48)$$

$$\Delta c' = -2(2\pi)^{\frac{2}{3}} \left(\frac{m^* \mathcal{E}_u^2}{h^2}\right) N^{\frac{1}{3}} L_2\left(\frac{T}{T_D}\right), \quad \text{for } n\text{-type Si} \quad (49)$$

where the temperature is normalized to degenerate temperature (T_D). Keyes calculated that 8% reduction in Δc_{44} should be attainable by doping n-type Ge [35]. With increase in temperature the electronic effect on elastic constant decreases. The function $L_2\left(\frac{T}{T_D}\right)$ and T_D is given by [71],

$$L_2\left(\frac{T}{T_D}\right) = \frac{2}{3} \left(\frac{T_D}{T}\right) \left[\frac{F_{\frac{1}{2}}'(\eta)}{F_{\frac{1}{2}}(\eta)}\right] \quad (50)$$

$$T_D = \left(\frac{3N}{8\pi v}\right)^{\frac{2}{3}} \left(\frac{h^2}{2m^*k}\right) \quad (51)$$

Keyes also derived expression for change in elastic constant due to changes in hole concentration observed in p-type Ge [76]. But he adopted some simplifying assumptions to make calculations simpler; for example, valence band was assumed to be perfectly

parabolic and heavy holes were only considered. Later, Csavinszky et al. [40] extended his model to p-type Si that also included the effect of light hole and split-off band hole. Equation (52) shows the general expression for change of elastic constant with hole concentration in p-type Si.

$$\Delta c' = -\frac{1}{5} \left(\frac{8\pi}{3} \right)^{\frac{2}{3}} \frac{\varepsilon_s'^2}{h^2} \{ m_{v1}^* N_1^{\frac{1}{3}} + m_{v2}^* N_2^{\frac{1}{3}} + m_{v3}^* N_3^{\frac{1}{3}} (1 - \frac{1}{15} \frac{\lambda}{\zeta}) \} \quad (52)$$

where λ is spin-orbit splitting; ε_s' is valence band's shear deformation potential constant; m_{v1}^* , m_{v2}^* and m_{v3}^* are effective masses of heavy hole, light hole and split-off band holes respectively; and N_1, N_2 and N_3 are heavy hole, light hole and split-off band hole concentrations respectively.

2.4 Conclusion

Finding the radiation damage mechanism on MEMS devices is of utmost importance to use MEMS devices in radiation environment. Ionization damage and/or displacement damage can cause MEMS devices to fail if they are not designed carefully. Electrostatically actuated MEMS devices are particularly vulnerable to dielectric charging by radiation. It has been found that shielding the dielectric material from radiation with conducting material dramatically increases radiation tolerance in electrostatically actuated MEMS accelerometers [77]. Similarly absence of dielectric material between electrodes was found to improve radiation hardness in MEMS micro-mirrors as reported by Miyahira et al [39]. Biasing electrodes was also found to improve radiation hardness. Both ionization and displacement damage changes elastic constant that shifts resonance frequency in

MEMS resonators. Once we know the mechanisms of such changes, compensation mechanisms can be implemented to reduce the effect of the change.

CHAPTER III

ASYMMETRIC MEMS RESONATOR

The piezoresistive effect in semiconductor materials such as silicon and germanium were discovered by Charles Smith in 1954 [78] and continues today to be a popular transduction mechanism in the field of MEMS. Piezoresistors are used in many MEMS devices such as resonators [79], pressure sensors [80], accelerometers [81], gyroscopes [82], gas detectors [83] and topography sensors in atomic force microscopes [84]. Silicon is the most commonly used material for piezoresistors. The sensitivity of a silicon piezoresistor depends on a number of factors including orientation of the piezoresistor (pzt) element, doping concentration, temperature and stress distribution. Three of these factors (orientation, doping concentration and temperature) determine the piezoresistive coefficient of silicon [85-89], while the stress distribution depends on the piezoresistor geometry and direction of applied load. If a piezoresistor is subjected to a uniaxial load, there is either compressive or tensile stress leading to a decrease or increase in resistance, respectively. Bending a piezoresistive beam puts one edge under compression and the other edge under tension creating regions of both positive and negative resistance change. The two effects can partially cancel each other reducing the net resistance change. For a completely symmetric system, the net resistance change will be nearly zero.

To increase the sensitivity of a given piezoresistor, the geometry should be optimized to reduce this cancellation and increase the net resistance change. Introducing asymmetry in the piezoresistor structure causes the stress distribution to be asymmetric, and the percent resistance change is consequently much higher for a given load or displacement. The most common method to introduce asymmetry is through the use of diffused piezoresistors and junction isolation. A diffused region is selectively introduced into regions with high stress of either tension or compression, but not both. This is easily implemented in devices with motion out of the plane of the substrate, such as the membranes used in a piezoresistive pressure sensor [80]. Asymmetry may be introduced through sidewall doping, and this has been demonstrated for in-plane force sensing [90-92]. Sidewall doping may be accomplished with either dopant diffusion or ion implantation. Sidewall doping is not widely used because of difficulties with introducing dopant atoms in the correct place and with making electrical contact [93, 94]. Another method to introduce asymmetry is to alter the sample geometry to create an asymmetrically shaped piezoresistor. For example, Fletcher *et al.* reported a substantial increase (15-200 times) in sensitivity due to introduction of asymmetry in a piezoresistor structure [95, 96]. If geometric changes could be used to improve the sensitivity this would have significant advantages over the use of diffusion. No lithography step would be required to define the diffused region, relaxing feature size requirements, reducing lithography steps, alignment error, and wiring complexity. This is particularly advantageous for applications where a beam is bending in the plane of the substrate, for which two piezoresistors would otherwise need to be formed on the edge of a cantilever beam.

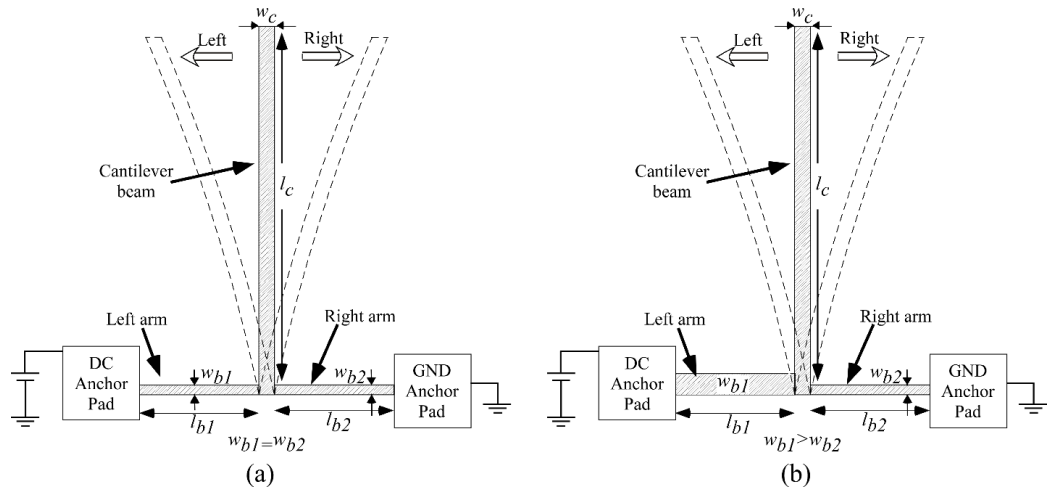


Fig. 8. (a) Symmetric and, (b) Asymmetric MEMS cantilever piezoresistor with dimensions [10].

In this section we simulate the performance of asymmetric, symmetric and diffused piezoresistors. The asymmetric and symmetric piezoresistors are uniformly doped using the starting substrate doping concentration. We use a lumped parameter model for asymmetric and symmetric piezoresistors to investigate the effect of asymmetry on stress distribution and resistance changes in different parts of the sample. Finally, we compare our simulation results with experimental data to validate the finite element and lumped parameter model simulations. We observe an increase in piezoresistor sensitivity of approximately 481 times due to the introduction of asymmetry [10].

3.1 Asymmetric and symmetric mems piezoresistors

A T-shaped mems piezoresistor is considered (as shown in Fig. 8) consisting of a freestanding cantilever beam attached to the center of a base beam. The base beam is clamped at both ends to the substrate by anchor pads, but is otherwise freestanding. The cantilever divides the base beam into two sections - left arm and right arm. The cantilever

beam can be displaced by an external force in either the left or right direction. This will in turn cause the base beam to bend. The amount of bending depends on the cantilever beam displacement and the base beam dimensions. If single crystal silicon or other piezoresistive material is used, this bending will induce resistance changes in the base beam. Piezoresistor dimensions are labeled in the figures where w_{b1} and w_{b2} represent the widths of the two regions of the base beam. Table 1 lists the numeric values of the dimensions used for the devices presented here.

Table 1: Piezoresistor Dimensions

Parameters	Symbols	Values (μm)	
		Asymmetric	Symmetric
Cantilever length	l_c	655	655
Cantilever width	w_c	8	8
Left arm width	w_{b1}	11	5
Right arm width	w_{b2}	5	5
Left arm length	l_{b1}	51	51
Right arm length	l_{b2}	51	51

The overall resistance change can be determined by applying a DC voltage across the base and measuring the current. Since the bending introduces varying compressive and tensile stresses in different regions of the base beam, the resistance change will vary spatially throughout the base. Asymmetry is introduced in the proposed model by connecting a wide piezoresistor with a narrow piezoresistor. Fig. 9 shows an exaggerated

view of the base bending for both the asymmetric and symmetric designs. A theoretical explanation for the performance of both the symmetric and asymmetric piezoresistors are described in sections 3.1.1 and 3.1.2, respectively. Fig. 10a shows the stress near the center of the base beam for the asymmetric case, and Fig. 10b shows an equivalent circuit of the piezoresistance at a point along the asymmetric beam. Similarly, for the symmetric case, Fig. 10c and 3d show the stress near the center of the beam and the equivalent circuit of the piezoresistance at a point along the symmetric beam.

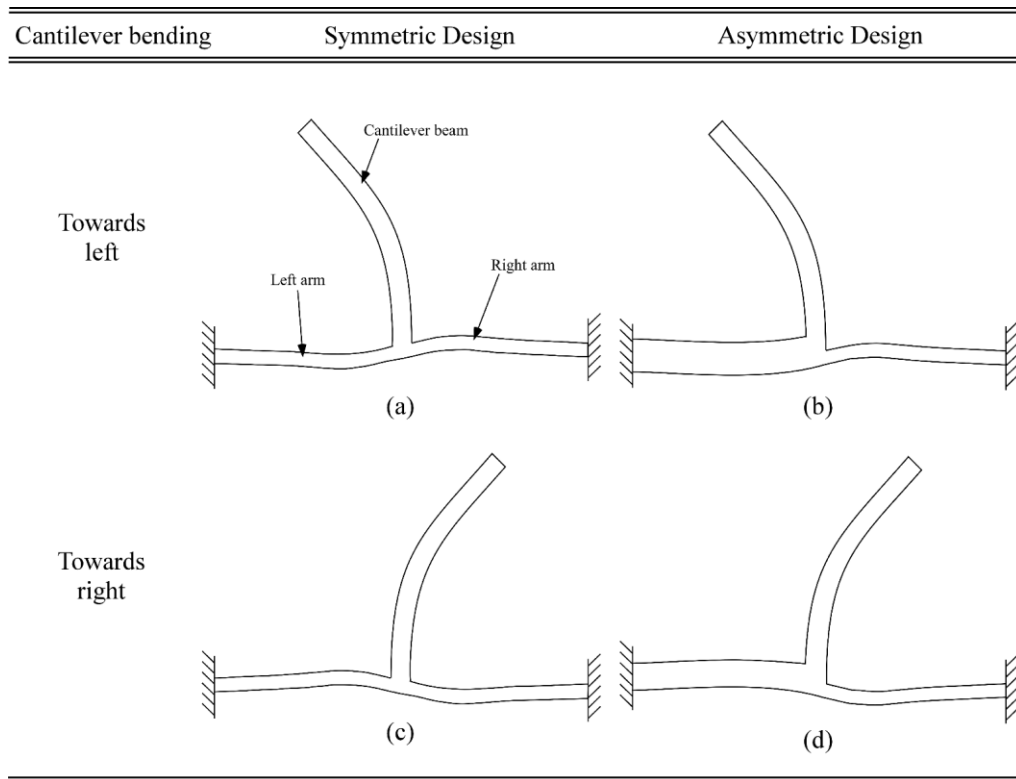


Fig. 9. Schematic illustration of base bending in asymmetric and symmetric models in two directions.

3.1.1. Symmetric Piezoresistor Theory

Fig. 10(c) shows a schematic of the symmetric piezoresistor near the center of the beam. The neutral axis is at the center of the beam, even if the beam is bent, as one side will be in compression and the other side will be in tension with equal magnitude. The resistance of a short segment of the piezoresistor may be found by considering the portion in compression and the portion in tension as separate piezoresistors in parallel, as shown in Fig. 10(d). Calculating the resistance change across a short bent section will show the contribution of that section to the overall resistance change. Suppose the resistances R1 and R2 had an initial value of R_0 at no bending condition. After bending the change in resistance of R1 and R2 are given by,

$$\Delta R1 = \pi_l \sigma_l R_0 \quad (53)$$

$$\Delta R2 = -\pi_l \sigma_l R_0 \quad (54)$$

where π_l and σ_l are the longitudinal piezoresistive coefficient and longitudinal stress respectively. Here it is assumed that the transverse stress is negligible.

Since the piezoresistors are oriented parallel to the [110] direction, the longitudinal piezoresistance is given by,

$$\pi_l = \frac{1}{2} (\pi_{11} + \pi_{12} + \pi_{44}) \quad (55)$$

But π_{11} and π_{12} are much smaller than π_{44} so equation (55) can be approximated by,

$$\pi_l = \frac{\pi_{44}}{2} \quad (56)$$

The equivalent resistance across the bent section is given by,

$$R_{eq} = \frac{R_0^2 + R_0\Delta R1 + R_0\Delta R2 + \Delta R1\Delta R2}{2R_0 + \Delta R1 + \Delta R2} \quad (57)$$

Using equation (53), (54) and (56), equation (57) simplifies to,

$$R_{eq} = \frac{R_0}{2} - \frac{\pi_{44}^2 \sigma_l^2 R_0}{4} \quad (58)$$

where the first term corresponds to the initial equivalent resistance ($\frac{R_0}{2}$) across that bent section. The change in equivalent resistance is given by,

$$\Delta R_{eq} = -\frac{\pi_{44}^2 \sigma_l^2 R_0}{4} \quad (59)$$

where the negative sign indicates that the resistance decreases. In a normal diffused piezoresistor, $\Delta R_{eq} \propto \pi_{44} \sigma_l$. Since $\pi_{44} \sigma_l \ll 1$, $(\pi_{44} \sigma_l)^2$ is very small and the sensitivity of the symmetric piezoresistor design is significantly reduced compared to a normal diffused piezoresistor. Furthermore, because this term is squared, it is impossible to determine the direction of bending, as the resistance always decreases. In practice, the overall resistance change across the piezoresistor is also affected by the edge effects at the joints especially where the two arms connect. The overall resistance change will be dominated by those edge effects for the symmetric piezoresistor since the contribution from the two base arms is very small.

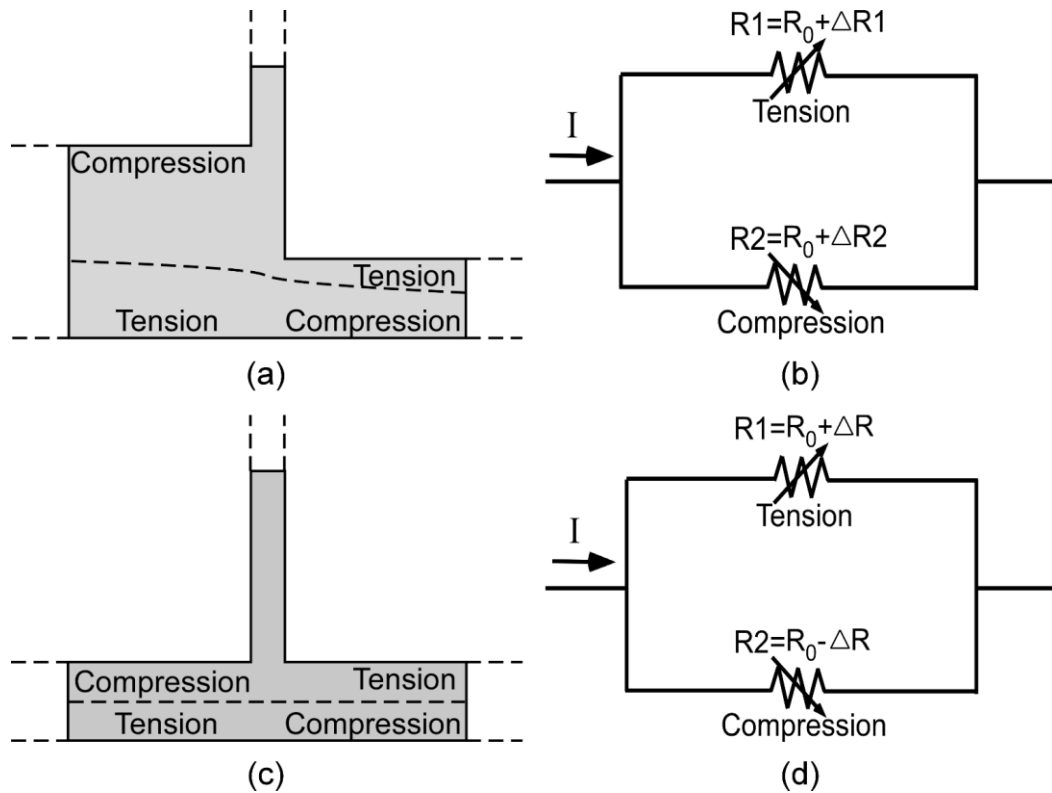


Fig. 10. (a) Schematic showing the position of neutral axis (dotted line) in the asymmetric model for bending in left direction. (b) Equivalent circuit of a short section of the base under bending. (c) Schematic showing the neutral axis is centered in the base beam in the symmetric piezoresistor. (d) Equivalent circuit of a short section of the symmetric base under bending with equal magnitude but opposite signs for the change in resistance.

3.1.2. Asymmetric Piezoresistor Theory

In order to obtain a good signal from a piezoresistor undergoing pure bending, it is necessary to add some asymmetry. In this work, a new design is introduced where the asymmetry is introduced through a geometric change while retaining the uniformly doped piezoresistor, causing an asymmetry in the stress distribution of the piezoresistor.

In the asymmetric design, the thicker base arm bends less than the thinner base arm due to higher stiffness of the thicker arm. Fig. 10(a) shows a schematic of the piezoresistor

near the center of the beam. The neutral axis of the two piezoresistors, which are located near the center of each beam, must shift to connect to make a common connection, as shown schematically in Fig. 10(a). On the left piezoresistor, the neutral axis is shifted down, resulting in a net compressive region. On the right piezoresistor, the neutral axis is shifted up, again resulting in a net compressive region. These effects do not cancel, always introducing more compression, and thus the sensitivity is improved. The piezoresistor on the right has a larger effect on the overall change in resistance because (1) the piezoresistor on the left has a smaller total resistance due to its greater width, and (2) the piezoresistor on the left has a smaller maximum stress because the force is distributed over a greater width.

Fig. 10(b) shows an equivalent circuit of a short segment of the piezoresistor, considering the compressive and tension regions as parallel resistors. The change in resistance for the two resistors are not equal in magnitude because the stresses above and below the neutral plane are unequal in value at each bent sections. There is a smaller cancellation of the resistance changes because the compressive and tensile stresses associated with a given segment of the piezoresistor are unequal. This in turn leads to a larger overall change in resistance across the piezoresistor. The goal of designing this type of asymmetric piezoresistor is to increase the width of the left piezoresistor as much as possible to introduce as much asymmetry as possible, but not increase the width of the beam so much that the stress is not transferred to the right piezoresistor. Numerical simulations are described in a later section wherein we found the optimal width of the left piezoresistor.

Table 2: Silicon Material Properties

Property	Values	Units
Orientation	(100)	-
Density	2330	kg/ μm^3
Young's modulus	170	GPa
Poisson's ratio	0.28	-
Conductivity	27.417	S/cm
Resistivity	0.036	$\Omega\text{-cm}$
π_{11}	$6.6 \cdot 10^{-11}$	1/Pa
π_{12}	$-1.1 \cdot 10^{-11}$	1/Pa
π_{44}	$81.684 \cdot 10^{-11}$	1/Pa

3.2 Finite element analysis

The asymmetric, symmetric and diffused piezoresistor models are simulated using two different Finite Element Model (FEM) simulation packages—COMSOL and CoventorWare. Table 2 lists the material properties used in the simulations. The substrate is chosen to be (100) silicon, with the piezoresistors aligned in the $\langle 110 \rangle$ direction to maximize the resistance change [86]. Among the three piezoresistive coefficients, π_{44} has the greatest effect on resistance change. Values for π_{11} and π_{12} of undoped silicon in the $\langle 110 \rangle$ direction are taken from the literature [97] while the value for π_{44} is extracted experimentally (as described in section V below). An external force is used to bend the cantilever beam. A DC voltage is applied across the base so that the base resistance change with respect to displacement can be determined. Since the resistance change in a piezoresistive material is directly related to the stress condition in that material, it is imperative to study the stress distribution in the model for proper insight of the physical

mechanism. Fig. 11 shows the stress distribution in a 3D color plot obtained from a COMSOL simulation for a beam displacement in the left direction. The figure shows that in the symmetric design high compressive and high tensile stresses arise near the anchor points and near the junction where the cantilever connects to the base beam. Compressive and tensile stress regions occur in pairs on either side of the cantilever and on opposing faces of the base beam. In the asymmetric case, the base beam's right arm also has two high stress regions with two pairs of compressively and tensely stressed sections. But the left arm has a different stress distribution due to the high rigidity of this section and only one compressive and one tensile region is found. Additionally, a shear stress is in effect in the region at the middle of the base beam that overlaps with the central cantilever in both designs. The stresses are uniform throughout the thickness of the base beam.

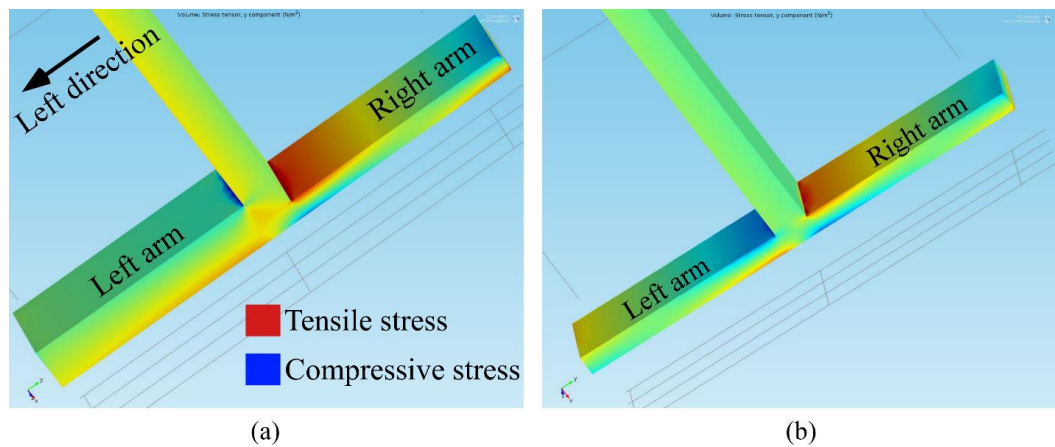


Fig. 11. Stress distribution 3D color plot when beam is displaced in the left direction for the asymmetric (a) and the symmetric (b) model.

To further clarify the mechanism, the longitudinal stress is plotted along the top and bottom edges of the two arms of the base beam for both asymmetric and symmetric design as shown in Fig. 12. As seen from the figure, in the symmetric case the average of the compressive and tensile stresses is very small. On the other hand, in the asymmetric

case the average is non-zero and found to have a net compressive stress of approximately 0.2 MPa and 0.09 MPa for thin and thick arm, respectively, for bending in the left direction. Similarly, bending in the right direction will have a net tensile stress for the asymmetric model. The direction of bending is distinguishable based on the net stress for the asymmetric design and this causes the resistance to change in opposite directions.

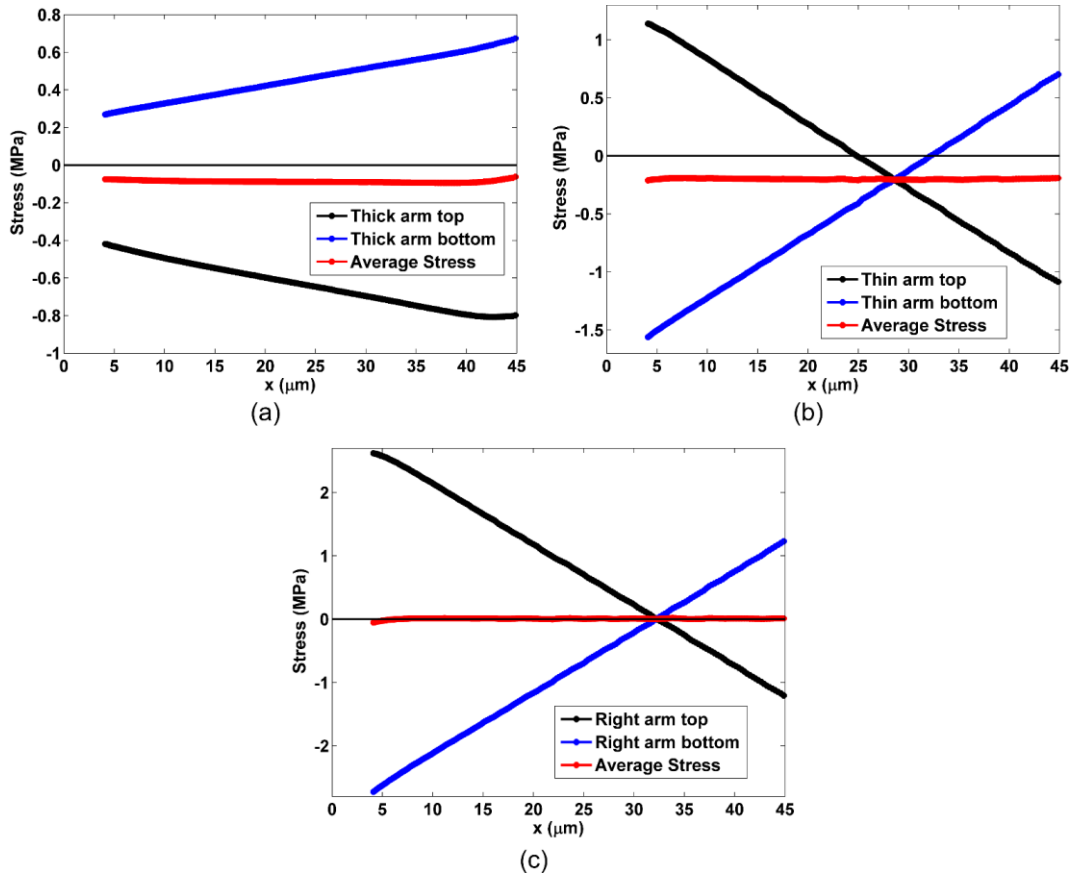


Fig. 12. Stress distribution along the edges of the base beam for (a) asymmetric model thick arm, (b) asymmetric model thin arm and, (c) symmetric model right arm. The red line shows the average of each two stresses along the length of the arms.

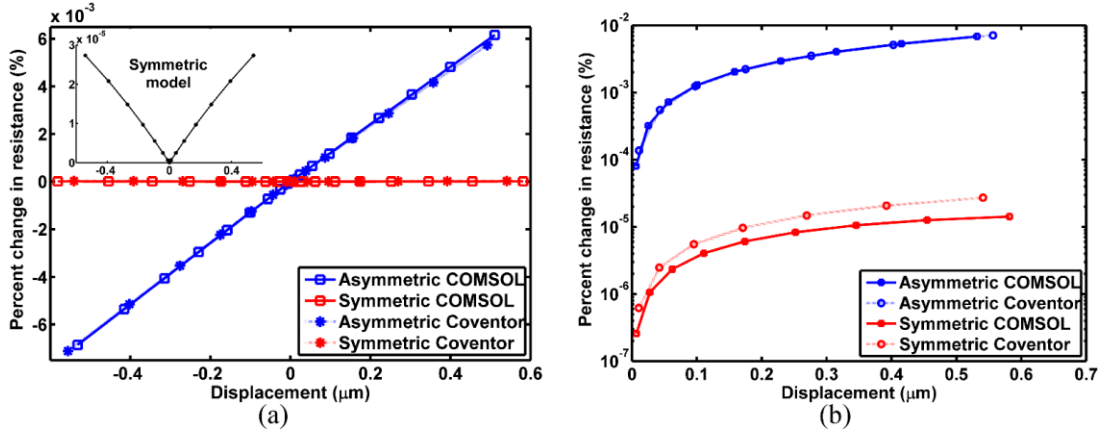


Fig. 13. (a) Comparison of asymmetric and symmetric piezoresistor performance with respect to percent resistance change in linear scale and, (b) comparison of performance for asymmetric, symmetric and diffused piezoresistor model in log scale. Inset of (a) shows the percent change in resistance versus displacement plot of symmetric case separately with magnified y-axis to clearly show the unidirectional nature of resistance change with displacement in either direction.

The percent change in the base resistance with respect to displacement is calculated for the symmetric and asymmetric piezoresistors. In the symmetric piezoresistor, the resistance increases with displacement in either direction as shown in the inset of Fig. 13(a) making it impossible to determine which direction the cantilever is bending. This implies that in the symmetric case there will be a frequency doubling in the rate of change of resistance compared to the driving frequency of the load when the structure is excited with an alternating load. Also, as shown in Fig. 13(a), the base resistance change in the symmetric design is very small due to excessive cancellation of resistance changes among the different parts of the model. On the other hand, for the asymmetric design the base resistance increases while bending in one direction and decreases while bending in another direction. When excited with an oscillating load, the frequency observed across the base will be at the same frequency as that of the driving frequency. Moreover, the peak-to-peak amplitude is doubled in the asymmetric case due to bidirectional change in resistance compared to

the symmetric case where the resistance change is unidirectional. Fig. 13(b) shows the comparison between the asymmetric and symmetric piezoresistor models on a semi-log scale. It shows results corresponding to bending in the right direction only for simplicity. It is observed from this figure that the change in resistance is more than two orders of magnitude higher in asymmetric model compared to symmetric model. Defining the sensitivity as $\frac{\Delta R/R}{d}$, where d is the cantilever tip displacement, it is found that the sensitivity of the asymmetric piezoresistor is 481 times higher than the symmetric piezoresistor.

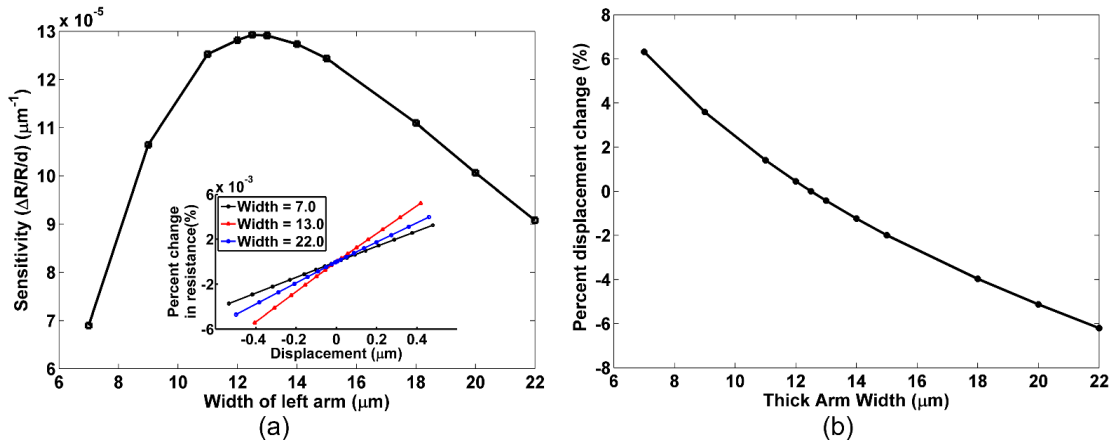


Fig. 14. (a) Plot of sensitivity versus width showing the optimum width of the left arm is 12.5 μm . Inset: Percentage of resistance change versus displacement for several left arm widths, (b) percent change in displacement for different thick arm widths.

Since the goal in the asymmetric piezoresistor design is to reduce the cancellation of resistance changes by introducing asymmetry in the geometry, it is imperative to do a parametric study to find the optimum geometric dimensions to maximize its performance. In the T-shaped piezoresistor, the asymmetry comes from the difference in the width of the two arms of the base beam as shown in Fig. 8. To investigate the effect of asymmetry, a simulation study is conducted with different widths of the left arm of the base beam. The sensitivity of the piezoresistor is plotted with respect to the left arm width in Fig. 14(a). It

shows that the optimum width of the left arm is approximately 12.5 micron. The inset shows the percentage of resistance change with respect to displacement for several widths of the left arm. Initially the sensitivity increases with left arm width due to the fact that the stress distribution is becoming more asymmetric, leading to lower cancellation of the resistance changes. However, when the left arm becomes too wide, the stiffness of that arm increases, resulting in less contribution from that arm in the net resistance change. These two competing processes lead to a maxima that yields optimized dimensions for the two sides of the base beam. The width of the left arm has very little impact on the displacement of the cantilever or the force sensitivity ($\Delta R/R/F_x$). Fig. 14(b) shows that the displacement varies by 6% or less as the width of the left arm changes.

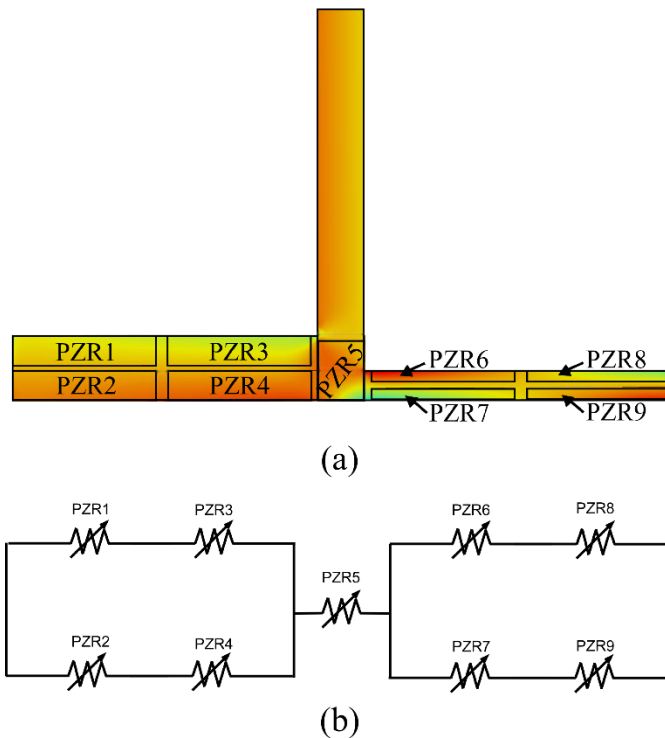


Fig. 15. (a) Creating nine separate piezoresistor elements out of the bulk model to formulate the lumped parameter model, (b) Equivalent circuit for the lumped parameter model.

3.3 Lumped parameter model

In the asymmetric and symmetric models discussed previously, the whole device is considered as a continuous piezoresistive element. To form a lumped model, the device is divided into nine discrete piezoresistor elements as shown in Fig. 15(a). Each piezoresistor element is subjected to either compression or tension depending on which direction the cantilever beam is bent. Fig. 15(b) shows how the resistances of the nine piezoresistor elements combine in a lumped parameter circuit to generate the overall resistance. FEM simulations are used to determine the resistances for each individual piezoresistor element for a given displacement. Then the lump parameter circuit is used to determine the total resistance across the entire base beam for that displacement. The lump parameter model helps explain the effect of asymmetry in the device geometry by isolated the contribution from each individual section of the device, and is useful for optimizing the device dimensions.

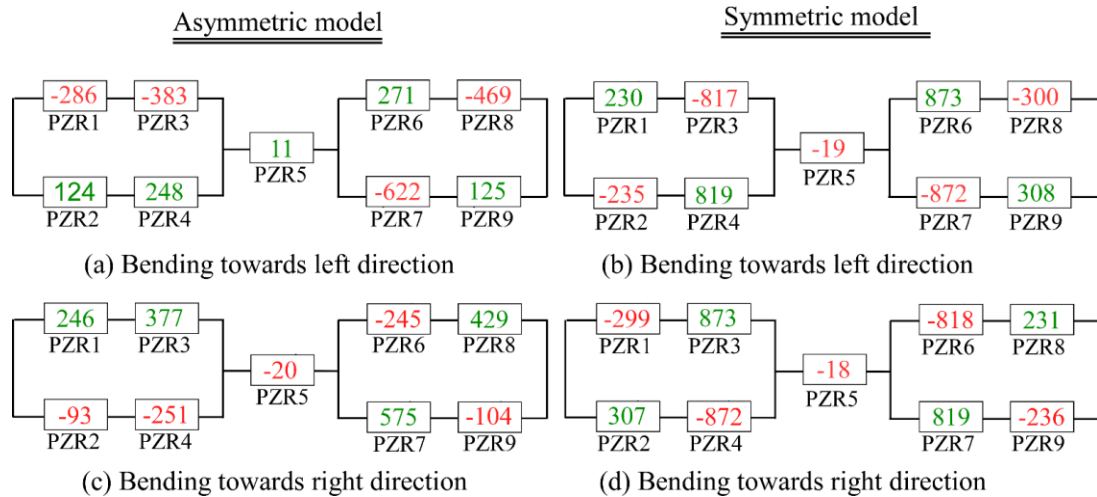


Fig. 16. Sensitivity values ($\times 10^{-6} \mu\text{m}^{-1}$) of each piezoresistor element for asymmetric model and symmetric model.

Fig. 16(a) and (b) shows the sensitivities ($\frac{\Delta R/R}{d}$) of each piezoresistor element of the asymmetric piezoresistor design and the symmetric piezoresistor design, respectively, for the cantilever beam bending in the left direction while (c) and (d) shows the same except for the cantilever beam bending towards the right. The sensitivities are calculated from the data obtained from the COMSOL simulation. Negative sensitivity is found at the regions of compressive stress while positive sensitivity is found at the regions of tensile stress. In the symmetric piezoresistor design, the external load produces four regions that undergo bending, generating compressive- tensile stress pairs on each bent region. The sensitivity values corresponding to each bent regions are almost equal but opposite in sign as shown in Fig. 16(b) and (d). That implies that the resistance change from each bent region is nearly zero due to the cancellation of resistance changes from the compressive and tensile sections. In the asymmetric design, the wider part of the base has one bending region while the other part has two bending regions. More importantly, the compressive and tensile stresses on each bent region is no longer of the same magnitude. So each bent segment has much more net contribution to the overall resistance change across the entire piezoresistor than with the symmetric case. The resistance change in the thin arm dominates the net resistance change across the base and it contributes about 84 % of the net resistance change for the proposed asymmetric structure. Additionally, since the stress distribution is asymmetric on two arms of the base, the total resistance decreases when the beam moves towards the left while resistance increases when the beam moves towards the right. That makes the resistance change bidirectional. On the contrary, the stress distribution is symmetric on the two base arms in the symmetric design and that makes the resistance change unidirectional for the application of the load in either direction.

Many MEMS devices described in the literature have diffused piezoresistor elements strategically placed to optimize device performance [81, 98-103]. Usually piezoresistor elements are placed at high stress areas of the device and connected together in a Wheatstone bridge configuration to maximize output. In the lump resistor model this would approximately correspond to taking the combined magnitudes of resistors PZR3 and PZR4. The change in resistance in the asymmetric piezoresistor is approximately 12% of the resistance change in a diffused piezoresistor, showing that the asymmetric resistance change is substantially smaller than what is achievable using diffused elements. However, the asymmetric design is considerably easier to fabricate and wire than the diffused piezoresistor, and the sensitivity is large enough for many applications. In the asymmetric design, uniformly doped structures can be used without defining any diffusion regions. This helps to reduce the device dimensions and also reduces lithography steps to fabricate the device. Another advantage is that it is easier to connect the asymmetric piezoresistors with the external circuit since the contact pads can be conveniently placed outside the oscillating freestanding structure. It increases reliability and leads to simpler design of mems devices.

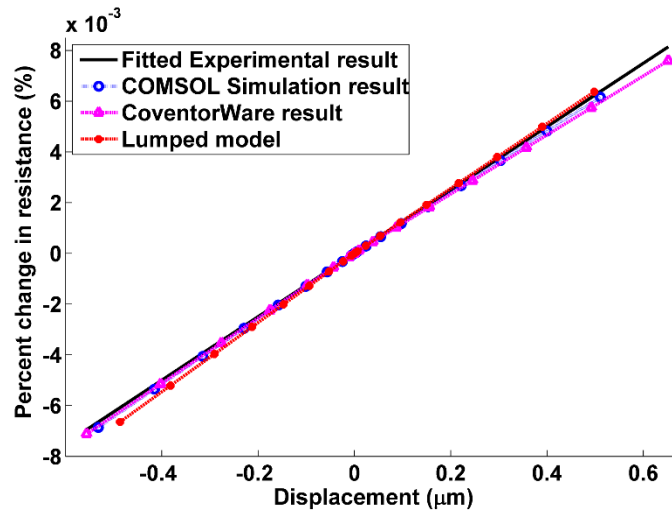


Fig. 17. Comparison of experimental, simulation and lumped model with respect to displacement vs. percent change in base resistance plot.

3.4 Experimental results

Testing is conducted to find the change in resistance with displacement of the cantilever beam. It is performed using a probe station and the data obtained from the experiment is then examined to find a linear fit. The linear fit of the experimental data is plotted in Fig. 17 along with the simulation data from COMSOL, CoventorWare and the lumped parameter model. All results match closely as shown in the figure. The agreement found between the simulation data and the experimental data validates the computer simulations and the lumped parameter model.

3.5 Conclusion

From the comparison of the asymmetric, symmetric and diffused piezoresistor models, it is evident that the asymmetric piezoresistors offer distinctive advantages over both the symmetric and diffused piezoresistor models. The asymmetric piezoresistors are approximately 481 times more sensitive than the symmetric piezoresistors due to less

cancellation of local resistance changes in different parts of the piezoresistors. Asymmetric piezoresistors also have distinctive advantages over the diffused piezoresistors with respect to ease of design, fabrication and wiring. They offer better process control due to less fabrication steps and less temperature sensitivity during fabrication due to the absence of any diffused regions and associated junctions. The lumped parameter model helped us to understand the effect of stress distribution on the piezoresistor performance. The accuracy of the simulated models are tested against experimental data and found excellent agreement among them. The concept of utilizing geometric asymmetry to optimize stress distribution that increases net resistance change by reducing cancellation can be expanded to other asymmetric geometries and is a potential field of research. Although not demonstrated here, if multiple beams are utilized, multiple piezoresistors may be obtained and arranged in a Wheatstone configuration as commonly used with diffused piezoresistors.

CHAPTER IV

FABRICATION AND EXPERIMENTAL SETUP

This chapter will focus on the fabrication of MEMS resonators and the experimental setup that had been used to conduct the radiation experiment. I will also discuss about the data analysis techniques that we used to produce presented results. Before starting fabrication, we designed and simulated our MEMS devices in COMSOL and CoventorWare to optimize the device performance. After finalizing the device dimensions, we designed our photomask for fabrication in L-Edit. We included a lot of test structures in our design to measure different parameters such as resistivity, mobility and contact resistance. We fabricated our devices in University of Louisville's Micro/Nano Technology Center (MNTC). The UV radiation experiments were conducted in our lab at University of Louisville, but the X-ray radiation experiments were conducted at Vanderbilt University's ARACOR 10keV X-ray system.

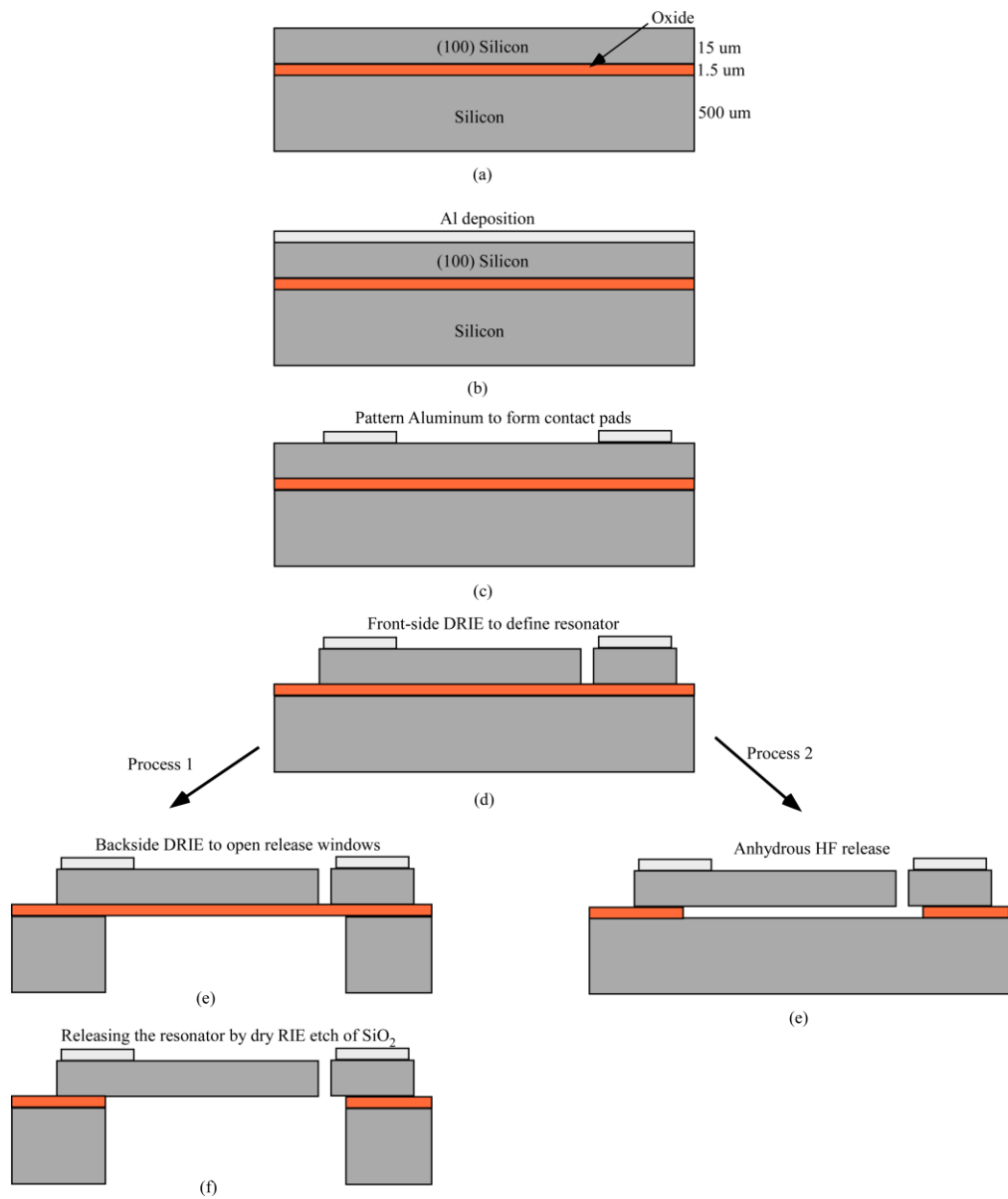


Fig. 18. Fabrication flowchart showing the major steps in the fabrication.

4.1 Fabrication of Si MEMS resonators

The fabrication started with a silicon-on-insulator(SOI) wafer. The selected SOI wafer has a device layer thickness of 15 microns, a buried oxide layer thickness of 1.5 microns and a handle wafer thickness of 500 microns. The target dimensions of the

piezoresistors are chosen to be the same as in the previously described simulated piezoresistor model for the asymmetric resonator design and are listed in Table 1. The device layer of the SOI wafer has a resistivity of approximately $0.03 \Omega\text{-cm}$.

Fig. 18 shows the fabrication sequence of the asymmetric resonator. The benefit of using an SOI wafer is that it has a built-in sacrificial oxide layer underneath the device layer that facilitates the release of the final freestanding structures. Before starting the fabrication, the SOI wafer is RCA-1 cleaned to remove any native oxide from the surface of device layer along with any other contaminants. This also helps with the adherence of aluminum to the silicon surface which is sputter deposited immediately after the cleaning process. The deposited aluminum is then patterned using optical lithography to create the contact pads.

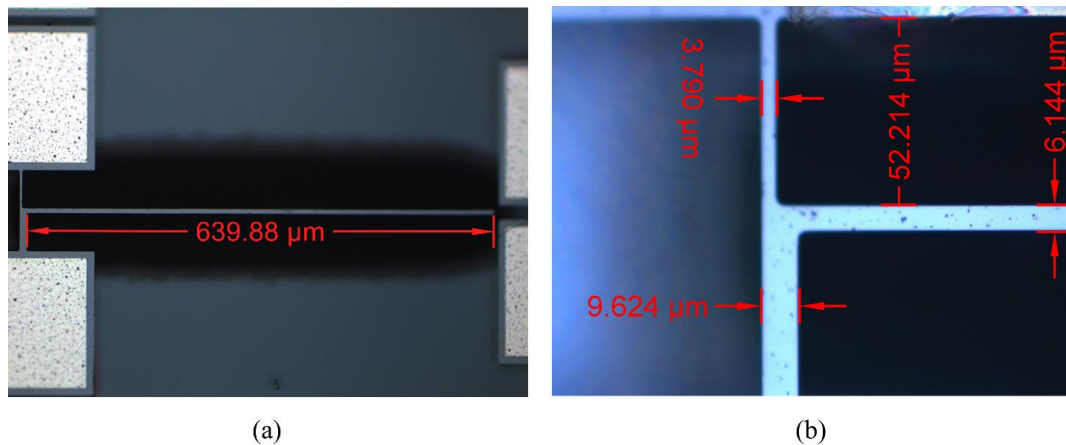


Fig. 19. (a) Optical micrograph of the fabricated device with dimensions (b) Magnified view of the piezoresistor base.

The second lithography step defines the piezoresistors on the device layer. Deep Reactive Ion Etching (DRIE) is used to pattern the device layer which removes silicon from everywhere except on the devices. At this point the piezoresistors are attached to the substrate by the 1.5micron oxide layer. We used one of two different approaches to release

the resonators from the substrate: either backside Si etch followed by dry reactive ion etching of SiO₂ (process 1) or anhydrous HF dry release (process 2). For the former release process (process 1), a third lithography step defines the backside release window that is followed by DRIE of silicon handle layer all the way up to the oxide layer. The oxide layer acts as an etch-stop layer in this case since DRIE is highly selective. Next, the oxide layer is dry etched in a Trion ICP Etcher to release the resonators completely from the substrate. On the other hand, in anhydrous HF release process (process 2), we used HF vapor that provides an isotropic etch of SiO₂. Both the processes avoid the stiction problem often encountered during a wet etch release procedure, but the advantage of anhydrous HF release is it reduces the fabrication time by reducing the number of process steps required while increasing the yield significantly. Furthermore, it was possible to get smaller feature sizes (e.g. 1µm features) with anhydrous HF release whereas in the other process the thinner devices often get broken due to the stress in buried oxide layer when backside window is opened. The disadvantage of anhydrous HF release is that the substrate is not removed from underneath the resonators. That might cause some spring softening effect due to the charging of the substrate although it was not significant in our experiments. Another disadvantage is that any further wet processing will lead to stiction. Fig. 19 shows a fabricated device along with measured dimensions. We will discuss the major fabrication steps in more detail in the next few sub-sections.

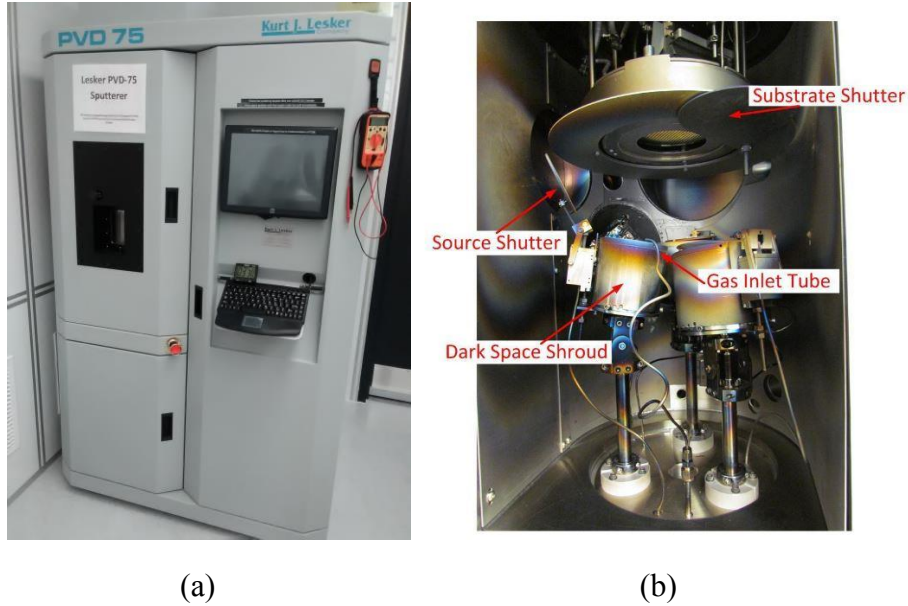


Fig. 20. (a) PVD75 system in the MNTC cleanroom, (b) The deposition chamber inside the PVD75 system [7].

4.1.1. Metal deposition and etching

PVD75 sputtering system shown in Fig. 20(a) was used for metal deposition. It contains a deposition chamber as shown in Fig. 20(b) and the chamber is maintained at a high pressure ($>1.1 \times 10^{-6}$ Torr) during deposition in Argon gas environment. A high DC voltage is applied across the chamber that ionizes the Argon gas molecules and it accelerates towards the target to knock-off metal atoms that get deposited on the substrate silicon wafer. We used two different types of contact metals (aluminum and gold) for our resonators. For gold contacts, we used Cr as an adhesion layer. The benefit of using gold is that buffered oxide etch (BOE) can be carried out after the metallization step without worrying about inadvertently etching the contact metal. TABLE 3 lists all the metal deposition process parameters and obtained film thicknesses.

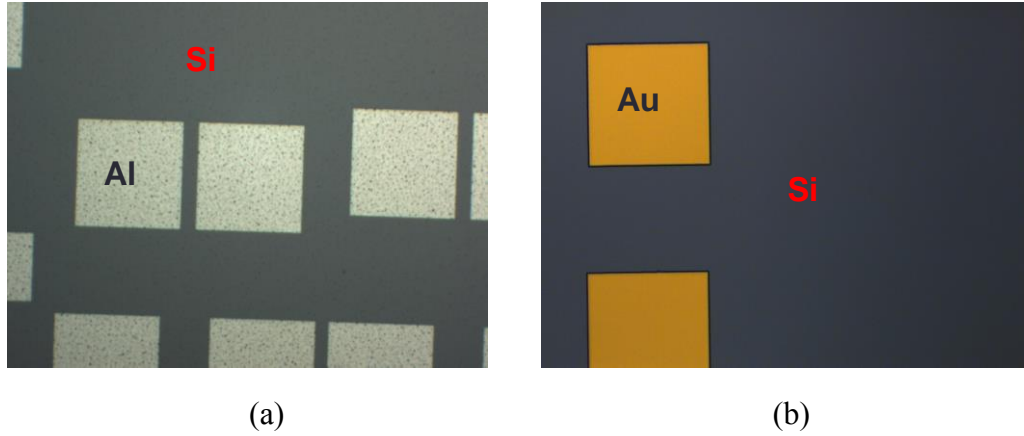


Fig. 21. (a) Al contact pads and (b) gold contact pads after wet etching of exposed contact metals.

TABLE 3: Process parameters of the PVD75 metal deposition system.

PVD75 Metal deposition	Power (W)	Base pressure (Torr)	Capman Pressure (mT)	Deposition Time (min)	Deposition Rate (nm/min)	Film thickness (nm)
Al	500	1.1×10^{-6}	5	32	≈ 19	≈ 608
Cr	300	1.1×10^{-6}	5	2.5	≈ 10	≈ 25
Au	300	1.1×10^{-6}	5	6	≈ 60	≈ 360

Fig. 21 shows the images of the Al and Au contact pads after the metal wet etching process.

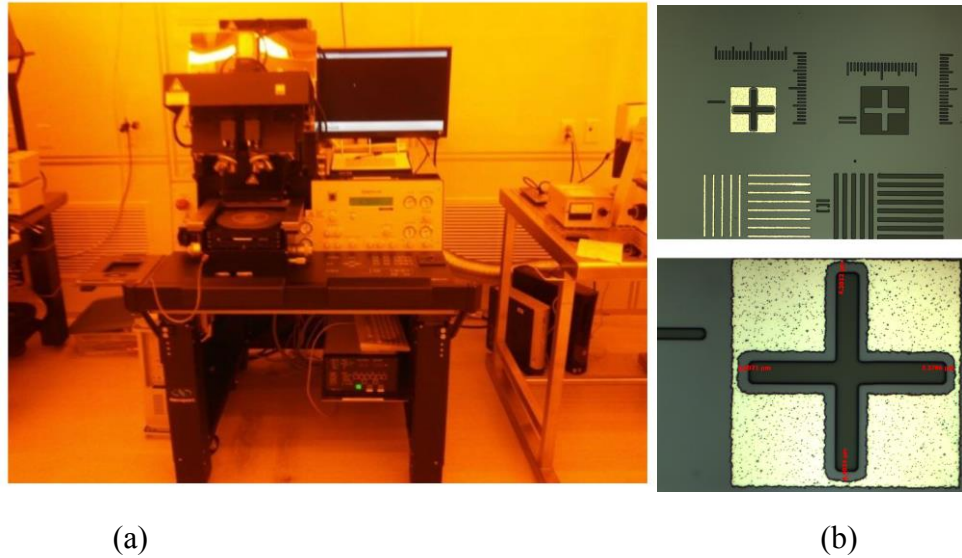


Fig. 22. (a) SUSS Mask Aligner in the cleanroom [6] and, (2) alignment marks (at two levels of magnification) used for the lithography.

4.1.2. Photolithography

Photolithography is basic building block of any microfabrication process. The complexity of a fabrication process often can be accurately reflected by the number of lithography steps required. In our case, we needed either two or three standard lithography steps depending on the how the devices were release from the substrate. Four different types of resist were used in the fabrication process of different batches/types of devices. Fig. 22(a) shows the SUSS mask aligner that was used for wafer alignment and UV exposure. Fig. 22(b) shows a typical alignment mark where a “+” mark on the photomask is aligned to the associated mark on the wafer from previous Al pattern. TABLE 4 reports different parameters that were used in the lithography process.

TABLE 4: Parameters used for photolithography process using different resists.

Resist	Spin recipe		Soft-bake		Exposure time(s)	Exposure Mode	Developer	Development Time (s)
	Spin speed (rpm)	Spin time (s)	Temp. (°C)	Time (s)				
1813	4000	30	115	120	8.5	Vac contact	MF319	70
1827	4000	30	115	120	12.8	Vac contact	MF319	90
SPR 220-7	4000	10	90 115	180 300	40	Prox. contact	MF319	123
AZ46 20	3000	30	100	600	38	Prox. contact	4:1 DI:AZ400K	120



Fig. 23. DRIE tool at the MNTC's cleanroom.

4.1.3. Deep Reactive Ion Etching of Si

TABLE 5: DRIE etch parameters used to etch silicon device layer.

DRIE Parameters		Etch		Passivation	
		Flow (sccm)	Tol(%)	Flow(sccm)	Tol(%)
Gas flow	C ₄ F ₈	0	5	85	5
	SF ₆	130	15	0	5
	O ₂	7.0	15	0	5
	Ar	0	5	0	5
		Etch		Passivation	
RF Power		800 W		800 W	
Platen power		12 W		0 W	
Cycle time		3 sec		2.1sec	

We used Bosch Deep Reactive Ion Etching (DRIE) process [104] to obtain anisotropic vertical silicon etch. Fig. 23 shows the DRIE tool used for the process. In this tool, Inductively Coupled Plasma (ICP) of different gases is used to conduct the etch and passivation of silicon. The vertical etch profile is obtained by using alternative etch and passivation cycle. During etch cycle SF₆ gas etches silicon along with any passivation layer on the vertically exposed area while during passivation cycle C₄F₈ gas deposits a polymer layer everywhere on the surface. The sidewalls remain protected by the passivation layer while the silicon etch progresses vertically. Photoresist was used as the masking layer since silicon etches about 50 times higher rate than photoresist in DRIE process. TABLE 5 lists all the DRIE process parameters. Fig. 24 shows the etch profile after the DRIE etch of silicon device layer while Fig. 25 shows the etch profile for the etching of backside window where the resonators are visible from the backside through the transparent thin oxide layer.

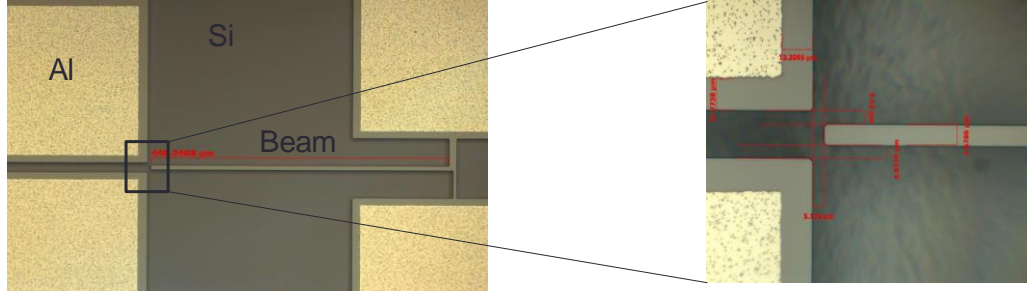


Fig. 24. (a) Resonator structure after the dry etch process, (b) zoomed-in view of the tip of the cantilever. The resonator is still attached to the substrate by the sacrificial oxide layer.

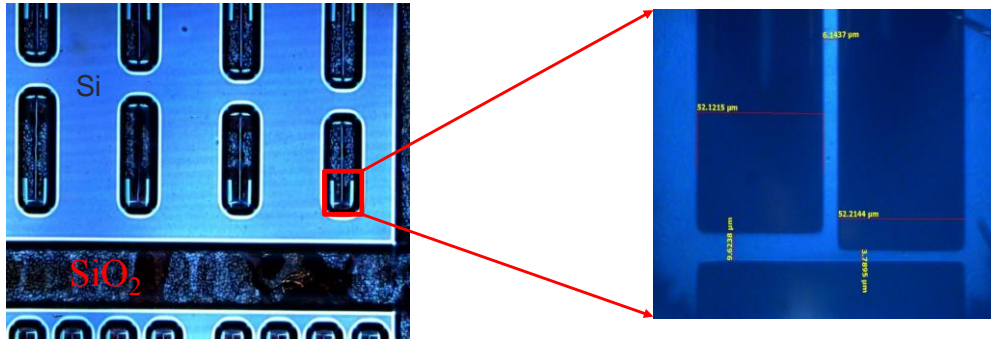


Fig. 25. (a) After the backside window etch using DRIE, (b) Zoomed-in view showing the resonator from the backside through the thin oxide layer.

TABLE 6: Trion metal etcher parameters used to etch photoresist and to etch SiO₂ layer.

TRION plasma Etching	Pressure (mT)	Gases	Flow rate (sccm)	ICP power (W)	RIE power (W)	He pressure (Torr)
O ₂ plasma cleaning	50	O ₂	50	300	0	5
SiO ₂ etch	10	CHF ₃ CF ₄	10 10	350	100	5

4.1.4. Dry Etching of SiO₂ in Trion Metal Etcher

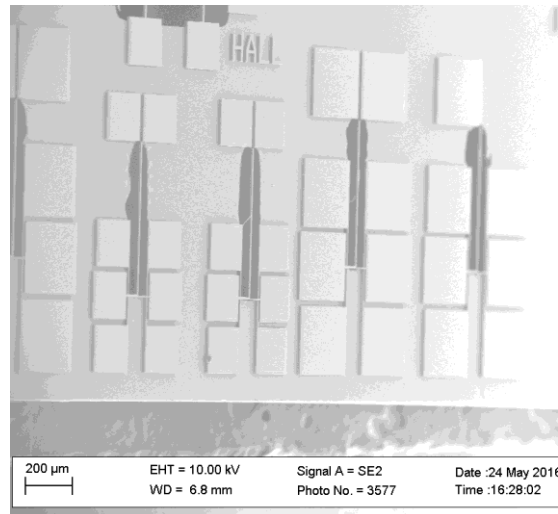


Fig. 26. SEM image of devices after etching away the sacrificial oxide layer from underneath the free-standing structures (black regions represents opened backside window area with no silicon).

Trion Metal Etcher uses reactive gas ions (ICP) to etch different materials including metals, semiconductor and dielectrics. We used equal proportion of CHF₃ and CF₄ gas combination to etch SiO₂ to release the freestanding structure of our resonators. TABLE 6 provides the list of parameters used in this process. The oxide etch was done from the backside of the wafer through the backside window opened by the previous silicon DRIE process. It was challenging to get a uniform etch of sacrificial oxide through the opening. It was critical to stop the etch after oxide is etched to prevent etching of the silicon resonator structure since the selectivity of the etch between silicon and SiO₂ was poor. As a result, often webs of oxide was present around the opened window as shown in Fig. 26. But the residual oxide near the window edge did not cause any issues and resonators were fully functional.



Fig. 27. Anhydrous HF etch tool in the cleanroom.

TABLE 7: Anhydrous etch process parameters

Anhydrous HF etch recipe	Steps	Time	Gass flow (sccm)			Etch Rate (nm/min)
			N ₂	Ethanol	HF	
Recipe 2	Stabilize	120	1250	350	0	-
	Etch	11000	1250	350	310	42
	Pump	30	0	0	0	-
Recipe 5	Stabilize	120	880	325	0	-
	Etch	3000	880	325	720	160
	Pump	30	0	0	0	-

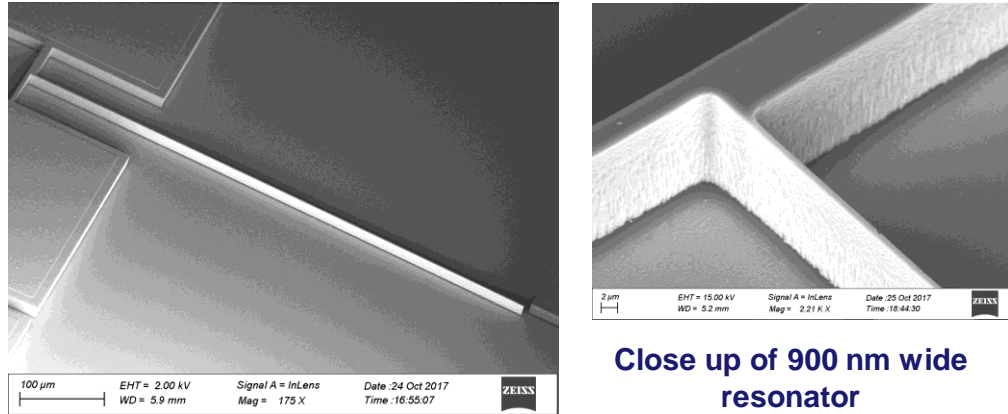


Fig. 28. (a) Device released using anhydrous HF etch process, (b) close up of one of the 900nm wide resonator cantilever.

4.1.5. Anhydrous HF release

In this process, HF vapor was used to etch sacrificial oxide. Fig. 27 shows the tool used for the anhydrous HF etch process. TABLE 7 shows the parameters used in this process. The etch rate is usually lower than the buffered oxide etch (BOE) and is controllable by changing the parameters. There is a trade-off between etch rate and uniformity where slower etch generally provides more uniform etch profile across the wafer. Most of the time we used “Recipe 2” as listed in TABLE 7. Fig. 28 shows some of our MEMS resonators released using anhydrous HF etch of the sacrificial oxide. As shown in the figure, cantilevers as narrow as 900nm was obtainable using this process without breakage.

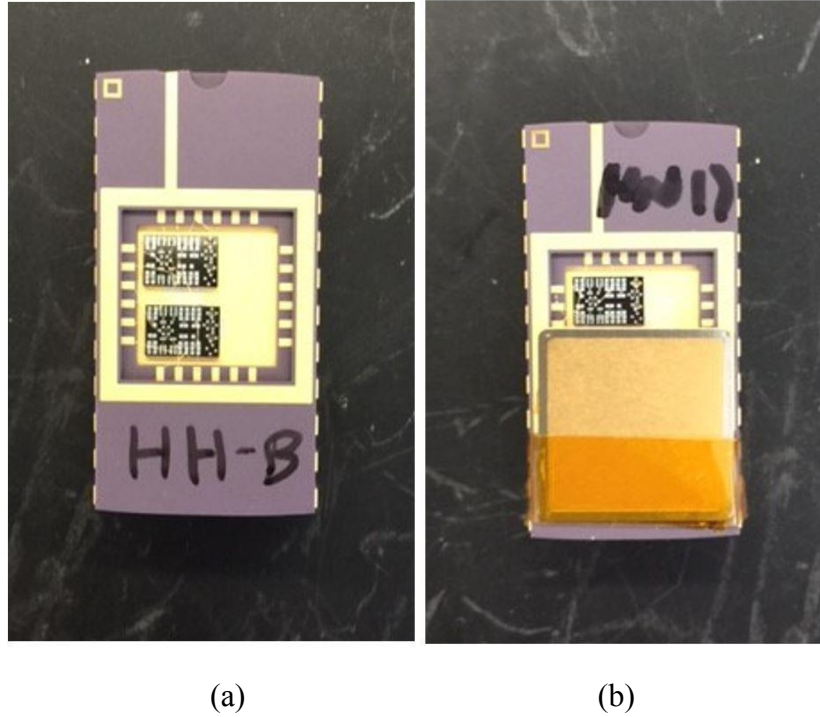


Fig. 29. (a) 2 dies (for target and reference devices) are bonded to chip carrier with silver epoxy, (b) reference device was covered with metal cover to shield it from radiation.

4.2 Packaging and wire-bonding

The resonators were packaged in Dual in-line chip carrier package (DIP). For UV experiment a reference device is placed below the target device where each device was on their own die as shown in Fig. 29. The reference device was shielded from radiation by a metal cover. The devices were bonded to gold plated pads of chip carrier using a K&S 4524D ball bonder. The parameters used in a typical Aluminum pad to chip carrier pad wire bonding process is presented in Table 8. The wire bonding temperature was 100⁰C for this process. Fig. 30 shows the SEM images of a wire bonded resonator.

Table 8: Ball bonding parameters

	Power	Time	Force	Loop	Tail	Ball
1 st Bond (on die pad)	3.25	3.1	2.9		6.7	3.8
2 nd bond (on DIP pad)	3.09	5.0	3.9			

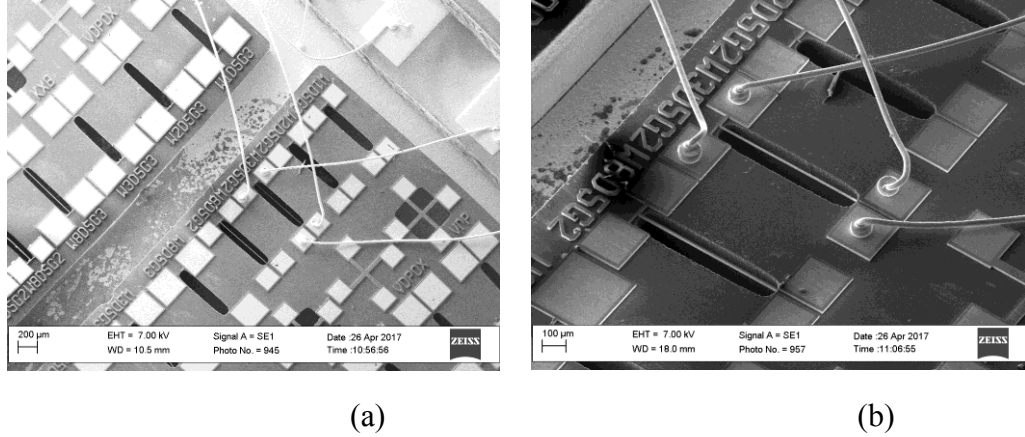


Fig. 30. (a) Wire bonded die, (b) close-up view of the wire bonding.

4.3 Resonance frequency measurement

Piezoresistive sensing mechanism is used to detect the resonance frequency of our resonators where the base of the resonator acts as a piezoresistor. As seen in Chapter 3, when the freestanding cantilever bends, the base get strained asymmetrically resulting in a net change in resistance across the base. We have also seen that the direction of resistance change is opposite (decrease and increase) for bending in two directions (left and right direction, respectively). Our resonators are driven electrostatically by applying an alternating voltage at one of the gates of the resonator. The other gate and one end of the cantilever base were grounded. A constant current/voltage is applied across the base so each mechanical oscillation of the cantilever resulted in an electrical signal of the same frequency across the base. Since electrostatic force between the cantilever and the gate reaches its peak twice each driving cycle, we only need to drive the cantilever at half the frequency of the resonance frequency to bring the cantilever into resonance.

So, we swept the driving ac signal frequency, f at some small interval (around half of theoretically expected resonance frequency value) while tracking the voltage across the base at twice the driving frequency, $2f$ using a lock-in amplifier to find and keep track of the resonance frequency. During radiation experiment, We choose a small enough window of frequency for scanning so that each scan can be done quickly but also made sure it is large enough so that it can track the shift in resonance frequency. The resonators were always driven in high vacuum to get a high Q factor. At pressure less than 10^{-4} mbar, the pressure dependence of resonance frequency was not significant.

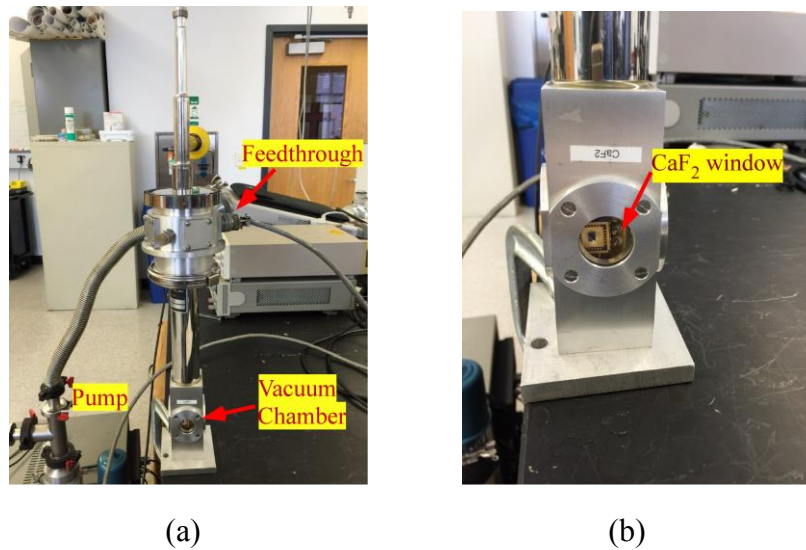


Fig. 31. (a) UV radiation experiment physical setup and, (b) CaF₂ window that passes UV light to the target device [8].

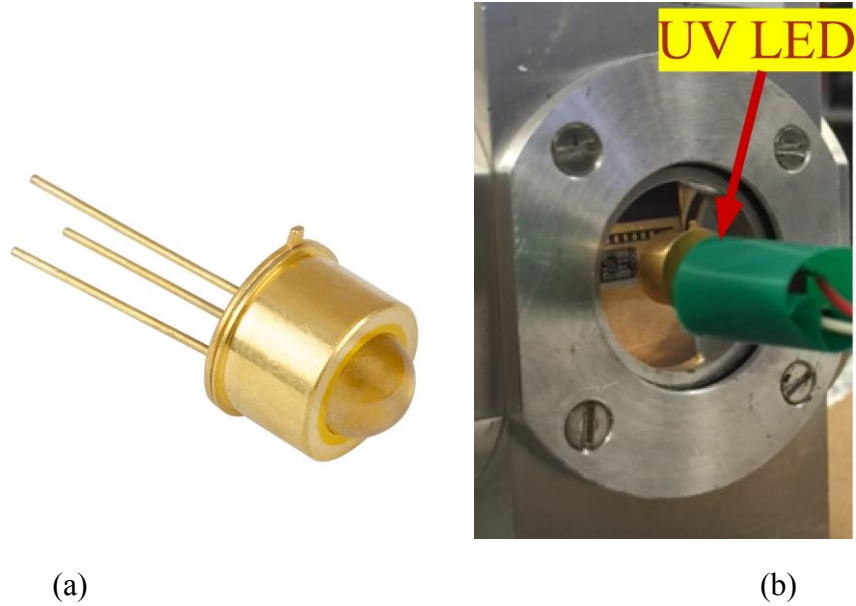


Fig. 32. (a) 255nm LED source used in our project [4] and, (b) LED placed in front of the CaF_2 window of cryostat to irradiate the device inside the vacuum chamber.

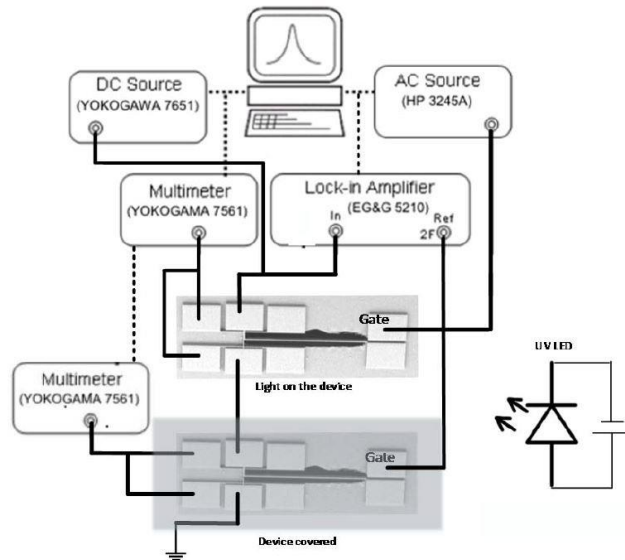


Fig. 33. Schematic illustration of the electrical setup for UV radiation experiment.

4.3.1. UV radiation exposure setup

Fig. 31 shows the physical setup for UV radiation experiment where a small vacuum chamber was used to mount the device vertically while facing towards the CaF_2

window. A UV LED (LED255J–OPTAN[®]) with a peak wavelength of 255nm was used as the UV source (Fig. 32). The power of the incident UV radiation on the exposed device from this LED is about 0.6mW/cm². Similar setup was used for the blue light exposure experiment except a 465nm blue LED was used instead of UV LED. Before each exposure the chamber is pumped for 48 – 72 hours so that a stable pressure on the order of 10⁻⁶mbar is obtained. A shielded reference device placed on the same chip carrier is used to subtract any heating effect from the experimental result. Fig. 33 shows the electrical setup used for UV experiment. The exposed and reference devices were connected in series and a constant current was applied across the devices. Since resonance frequencies of any two devices are usually not the same due to nonuniformity in the fabrication process, two different set of scanning frequency windows are alternated in a time-shared manner to keep track of the two resonance frequencies of the two devices. The resonance frequency was tracked before, during and after radiation to observe the effect of UV radiation.

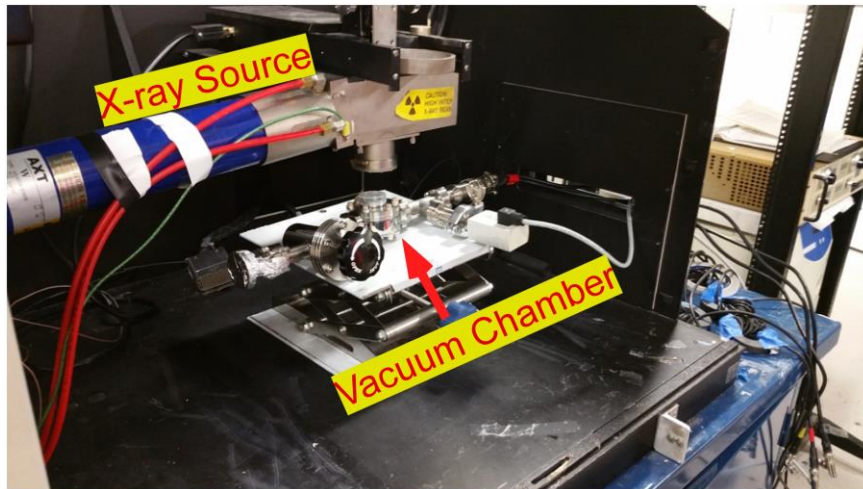


Fig. 34. ARACOR system's X-ray exposure chamber.

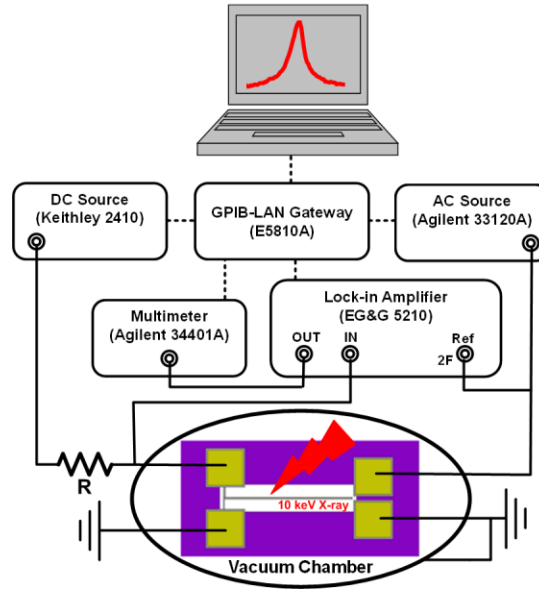


Fig. 35. Schematic diagram of X-ray radiation experiment's electrical measurement setup.

4.3.2. X-ray radiation exposure setup

X-ray radiation experiment was conducted at Vanderbilt University's ARACOR 10keV X-ray irradiator. The X-ray source was used to expose different resonators at 3 different dose rates (5.4, 10.9 and 30.3 krad(SiO_2/min)) with a total ionizing dose of up to 1Mrad(SiO_2) for each dose rates. Fig. 34 shows the X-ray system's exposure chamber where a small vacuum chamber containing the resonator is placed. Beryllium window of thickness $25.4\mu\text{m}$ is used to pass the X-ray to the device since it only absorbs 0.3% of X-ray energy. The vacuum chamber was pumped for at least 12 hours before each exposure to reach a stable pressure of 10^{-4}mbar . A fixed resistor (of similar resistance as the base resistance of the resonator e.g. $\approx 256\Omega$ for highly doped resonators) is connected in series with the base resistor of the resonator. A constant voltage of 50mV was applied across the series resistor assembly. A 4V ac signal was applied at one of the gate to drive the resonator while grounding the other gate. The voltage across the base resistor is connected to the

lock-in amplifier to track the voltage at twice the driving frequency. No reference device was used in case of X-ray since the noise at the underground radiation facility was very low and temperature was very stable. The resonance frequency was tracked before, during and after X-ray radiation by continuously scanning a small 2Hz frequency window around the pristine resonance frequency of the device. The hydrogenated devices were put in a steam bath for an hour before radiation to increase the hydrogen content in the device.

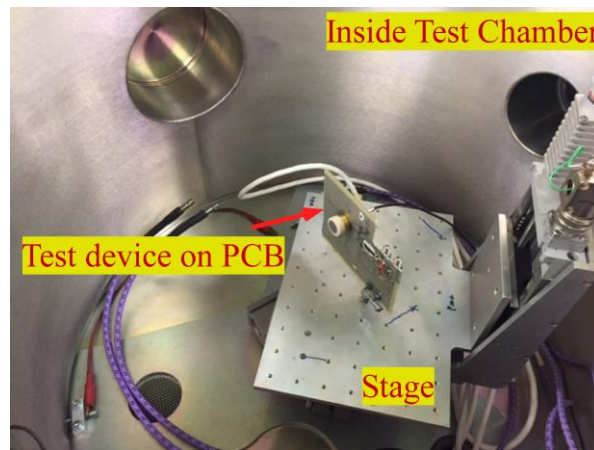


Fig. 36. Inside of proton radiation chamber where device was mounted for radiation exposure.

4.3.3. Proton radiation exposure setup

Proton radiation was conducted at Vanderbilt University using their Pelletron proton irradiation system [105]. For this experiment similar electrical setup is used as X-ray. The devices were radiated at a stable pressure of about 2×10^{-6} mbar at room temperature. The temperature variation during experiment was within 1°C . It is found that such temperature variation does not cause more than 10ppm change in resonance frequency. Resonators were irradiated with two different energies of proton—0.8MeV with

a proton flux of 4×10^8 ions/(cm²s) and 2MeV with a proton flux of 10^{10} ions/(cm²s). Fig. 36 shows the inside of the proton radiation chamber where the devices were mounted.

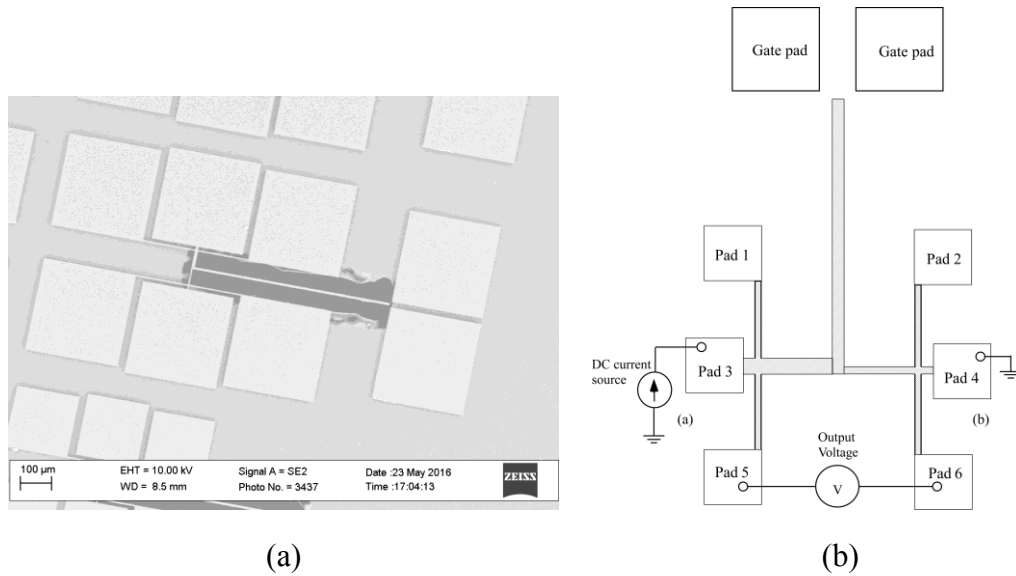


Fig. 37. (a) SEM image of a resonator with extra pads to support 4-wire resistance measurement, (b) 4-wire resistance measurement setup.

4.4 Base resistance measurement

For UV experiment, 4-wire resistance measurement of the base resistor was carried out along with the resonance frequency measurement on the same device. To conduct the 4-wire measurement some resonators were fabricated with extra set of pads as shown in Fig. 37(a). A constant current was applied across the pads 3 and 4 as shown in Fig. 37(b) while the voltage across the pads 5 and 6 is measured. From the known constant current and measured voltage 4-wire resistance is calculated. For X-ray radiation experiments, different set of devices were used to do the 4-wire resistance measurement and resonance frequency measurements.

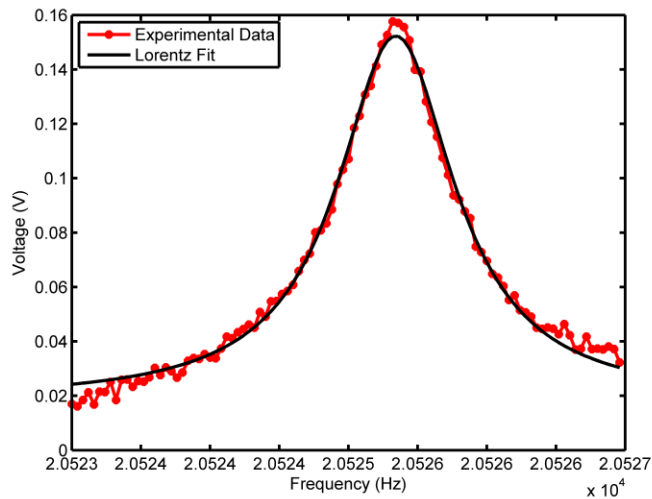


Fig. 38. The voltage across the base of the resonator is tracked at twice the driving frequency with the lock-in amplifier and recorded with LabView data acquisition software. The voltages are plotted against the tracking

4.5 Data acquisition and analysis

We automated the data collection system by using LabView data acquisition software. We controlled and read the data from frequency generator, DC current source, lock-in amplifier and other test equipment using LabView through GPIB (General Purpose Interface Bus) communication port. After collecting raw frequency and voltage data from the radiation experiments, we used Lorentzian Function to fit the data and determined the resonance frequency corresponding to the peak voltage of the fitted curve, as shown in Fig. 38.

4.6 Conclusion

The resonators showed very good stability and repeatability. The environmental variation of resonance frequency during X-ray and proton radiation was very small, mostly due to the underground location of the lab. Since UV experiment was carried out in a

noisier environment, a control device was implemented, and it successfully accounted for the environmental variation. We always kept the DC current through the base piezoresistor small enough to avoid significant Joule heating. We strived to keep the resonator oscillation in the linear regime to avoid nonlinear effect and our $8\mu\text{m}$ width resonators showed symmetric frequency response indicating linear modes of operation. The signal amplitude is stronger for $8\mu\text{m}$ width devices since they transfer larger stress at the base piezoresistor. To compensate for the lower stress transfer by smaller width ($2\mu\text{m}$ and $1\mu\text{m}$) devices, we sometimes had to apply higher ac gate voltage to increase the oscillation amplitude. That often lead to asymmetric frequency response, an indication of driving the resonator in nonlinear regime. But we were careful to avoid any errors arising from nonlinear operation such as always approaching the resonance from the same direction.

CHAPTER V

RESULTS

In this chapter, the results of the radiation experiments conducted on MEMS devices will be presented. We observed that MEMS devices get affected by both ionizing and non-ionizing radiation, but the damage pathways are different--even the difference in energy of the impinged radiation has significant effect on the amount and types of degradation observed. In most cases, the results are divided into three sections corresponding to pre-radiation, in-situ and post-radiation behavior of the MEMS devices. For UV radiation results, a shielded reference device was used to measure the heating effect and we used that result to separate the heating effect from the radiation effect on our target device. In all cases, the tests were conducted under vacuum and we pumped-down the vacuum chamber for long time (e.g. 12 hours to 72 hours) before taking pre-radiation measurements. That helped eliminate pressure and temperature fluctuations significantly. We radiated devices with different dopant types (B and Ph) and different dopant densities (e.g. $5.8 \times 10^{18} \text{cm}^{-3}$ and $3.6 \times 10^{17} \text{cm}^{-3}$). We also radiated devices with different beam widths (8 μm , 2 μm and 1 μm) for UV and X-ray experiments.

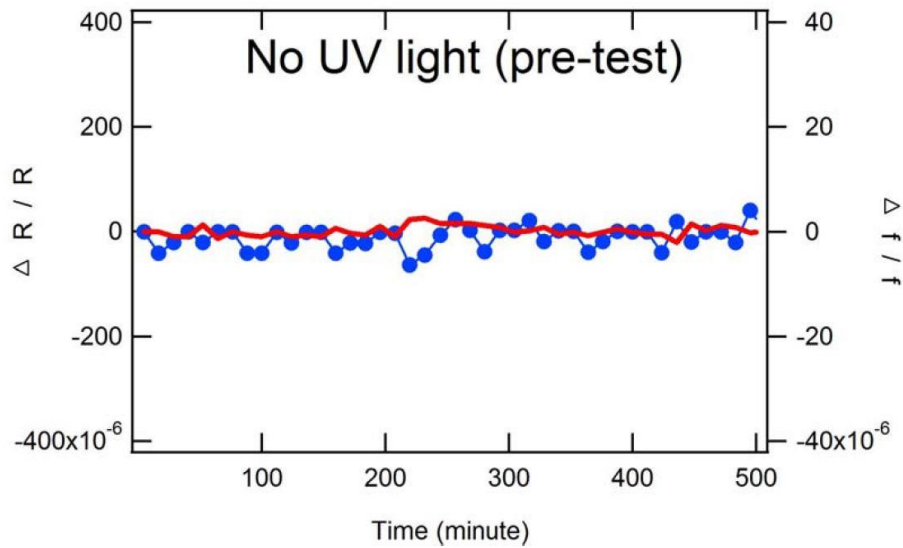


Fig. 39. Pre-radiation characterization of MEMS resonator showing stable resistance and resonance frequency behavior after pump-down of 3 days where the system attained a pressure of 3.5×10^{-6} mbar at room temperature [3].

5.1 UV radiation experimental result

We radiated Si MEMS resonator with UV and blue light. For this first set of results presented here (Fig. 8 to Fig. 42), the silicon had a p-type doping concentration of about $5.8 \times 10^{18} \text{cm}^{-3}$. Fig. 8 shows the stability of the observed parameters: resistance and resonance frequency at the pressure of 3.5×10^{-6} mbar. The temperature and pressure were very stable after continuous pump-down for 3 days. As a result, we can detect resonance frequency change as low as 5 ppm and resistance change as low as 50 ppm as seen in the figure.

As mentioned earlier, for UV experiments we used a reference device that was shielded from radiation by metal cover. We radiated both our target and reference (shielded) resonators by a 465nm wavelength Engin LZ1-10D800 LED blue light. The source had a peak wavelength of 425 nm and the output power was about 1.44mW. We

observed 4-terminal resistance and resonance frequency change as shown in Fig. 40. The resistance increased and resonance frequency decreased by roughly the same amount in the target and reference devices with a maximum decrease of 200ppm in resistance and 20 ppm in resonance frequency after 30 minutes of radiation at room temperature. The devices anneal completely within approximately 20 minutes after radiation.

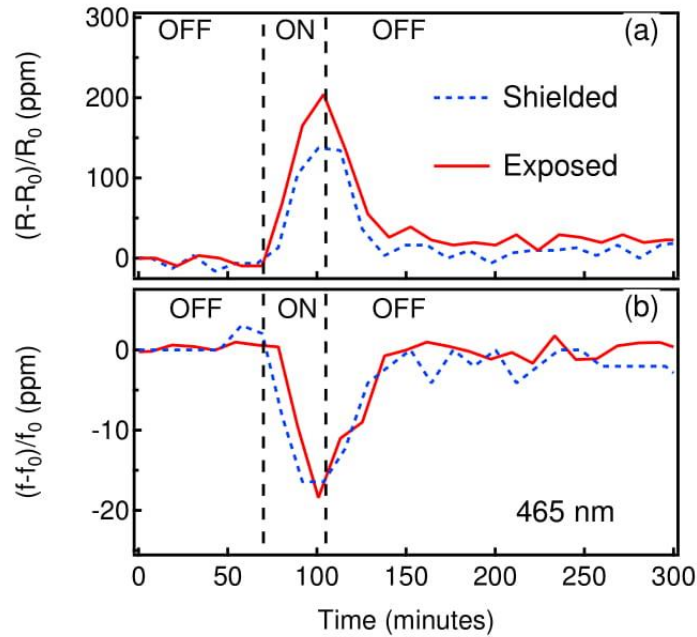


Fig. 40. (a) Ppm change in resistance and, (b) ppm change in resonance frequency for the exposed and shielded device under 465nm blue light radiation [13].

We exposed another set of devices to 255nm wavelength UV light. The UV source was Thorlabs LED255J Optan UV LED with output power of 220 μ W. The shielded device and exposed device behaved completely differently under UV light, particularly the UV-exposed device showed persistent change that lasted for long time while the shielded reference device recovered approximately after 20 minutes similar to the blue light radiation. Also, the resistance decreased in the exposed device while increased in the

reference shielded device. The amount of change in resistance and resonance frequency were also markedly different in the two devices. Fig. 42 shows the net change in the exposed device's 4-terminal resistance and resonance frequency due to UV radiation after subtracting the heating effect that was measured using the shielded device. The change in resistance was about 2500 ppm and change in resonance frequency was about 25ppm. The exposed device recovered after about 60hours in contrast with only 20 minutes for shielded device.

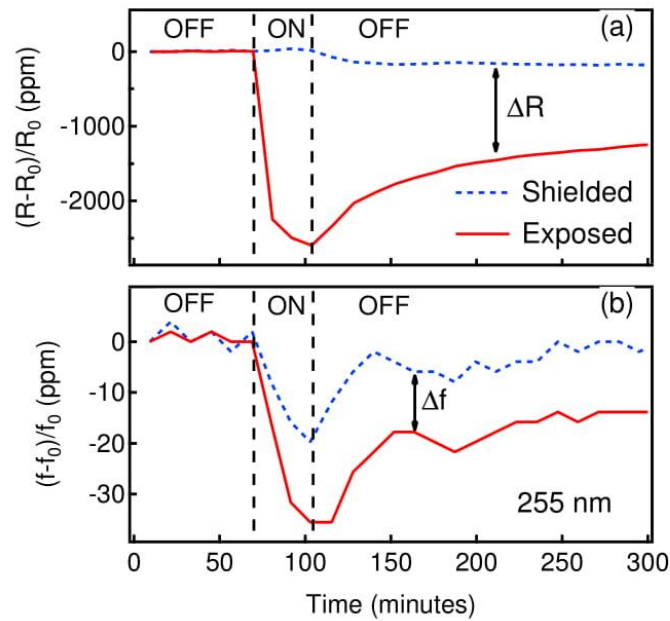


Fig. 41. (a) Ppm change in resistance and, (b) ppm change in resonance frequency under 255nm UV light for exposed and shielded devices [13].

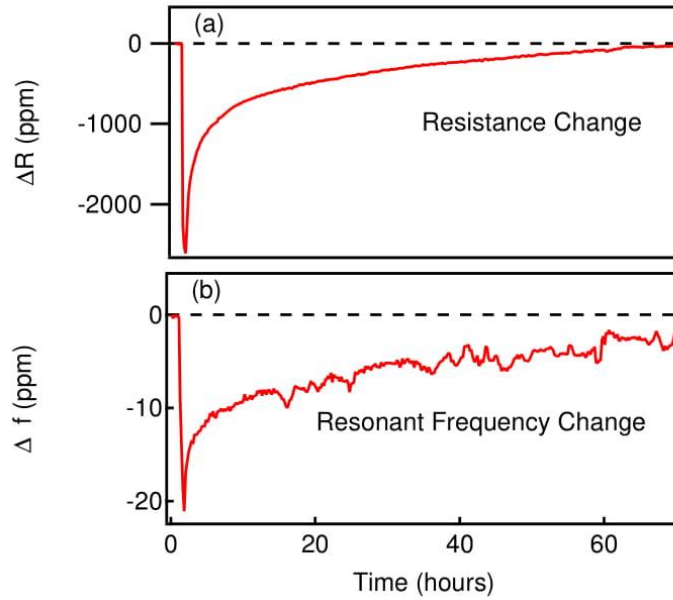
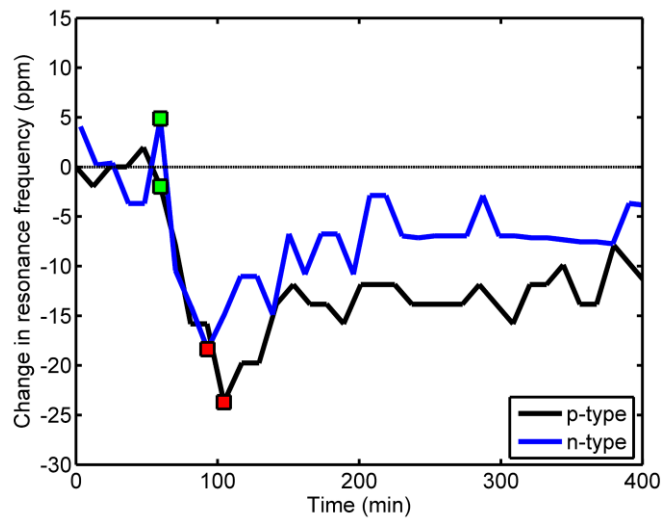
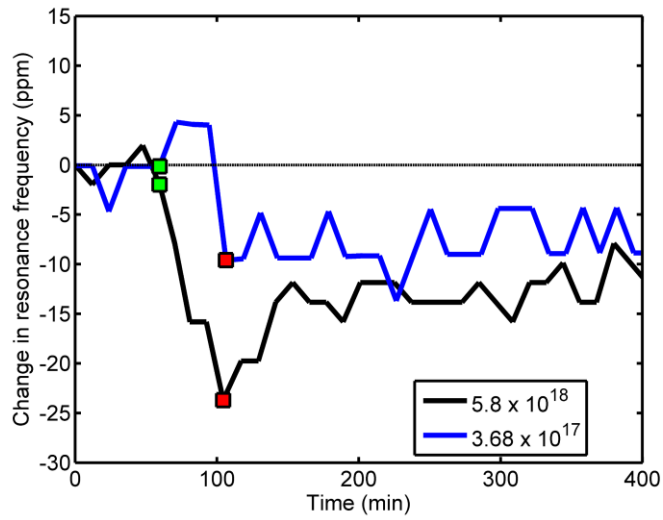


Fig. 42. Net change in 4-terminal resistance (a) and resonance frequency (b) in exposed device due to UV radiation after subtracting the temperature effect [13].

5.1.1. Effect of doping type and concentration

We exposed lower carrier concentration ($3.62 \times 10^{17} \text{cm}^{-3}$) n-type and lower carrier concentration ($3.68 \times 10^{17} \text{cm}^{-3}$) p-type Si resonators with UV in a similar setting as that of high carrier concentration ($5.8 \times 10^{18} \text{cm}^{-3}$) p-type UV radiation experiment mentioned above. The results of radiation test on all these three types of devices are showed in Fig. 43 where the ppm change in resonance frequency is showed as a function of time. The doping type and concentration does not have significant influence as the change in resonance frequencies in all three devices were comparable.



(a)

(b)

Fig. 43. Comparison of ppm change in resonance frequency of resonators before, during and after UV exposure (green and red markers indicate radiation on and off times respectively) with (a) two different p-type doping concentrations and, (b) p-type and n-type of about same doping ($\approx 3.6 \times 10^{17} \text{ cm}^{-3}$) concentration.

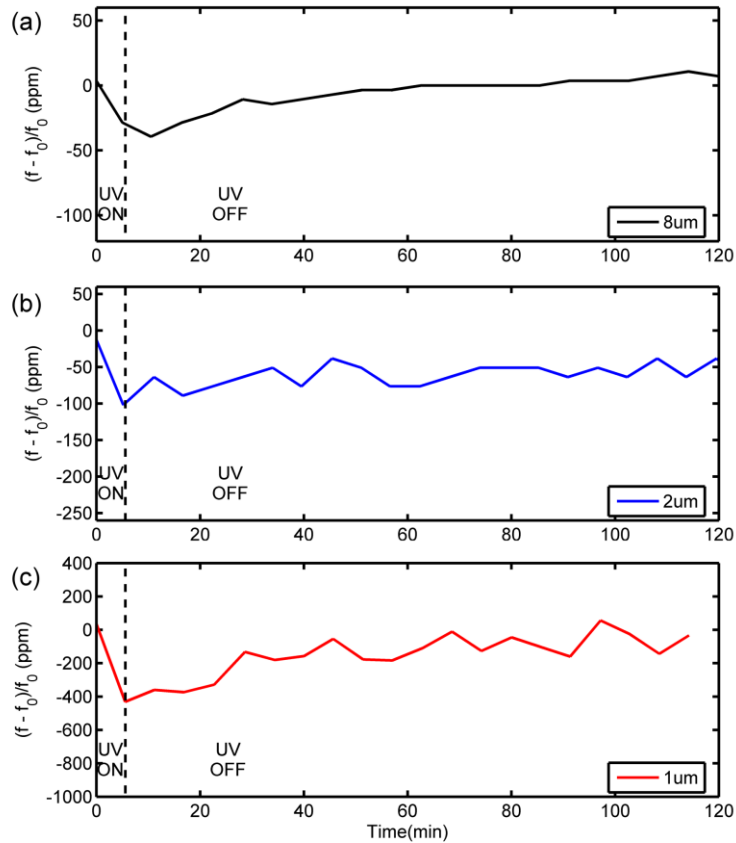


Fig. 44. Ppm change in resonance frequency as a function of time during 5.6 minutes of UV radiation and subsequent annealing for (a) 8µm, (b) 2µm and (c) 1µm wide resonators. The vertical dotted line separates the in-situ and Annealing data.

5.1.1. Effect of beam width

We investigated the effect of beam width on the resonance frequency shift due to UV radiation by conducting 5.6 minutes of UV radiation on resonators with three different beam widths, viz., 1µm, 2µm and 8µm. Fig. 44 shows the ppm change in resonance frequency as a function of time during radiation and after radiation. An unexposed control device on the same package has been used to monitor and subtract the heating effect from the UV result. The smaller devices showed a larger shift in resonance frequency. Devices with 1µm wide cantilever are noisier since the cantilever oscillation cannot transfer as

much energy to the resonator base to have large piezoresistive signal across the resonator base. To increase the reliability of our test, we repeated the UV radiation experiment on five different $1\mu\text{m}$ wide cantilever devices and averaged over the observed resonance frequency shifts.

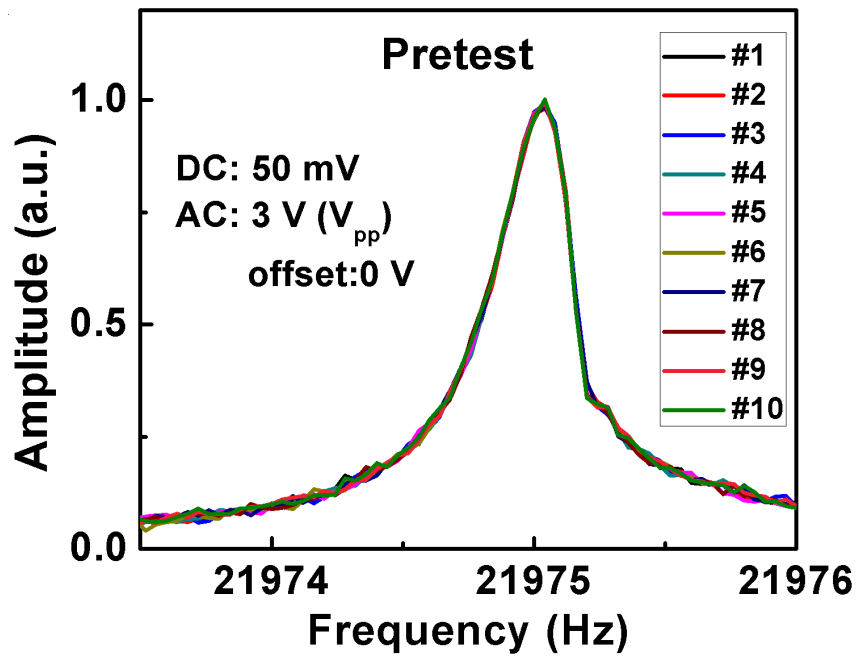


Fig. 45. Pre-radiation characterization of resonance frequency showing the stability of our measurement over 10 frequency sweeps [1].

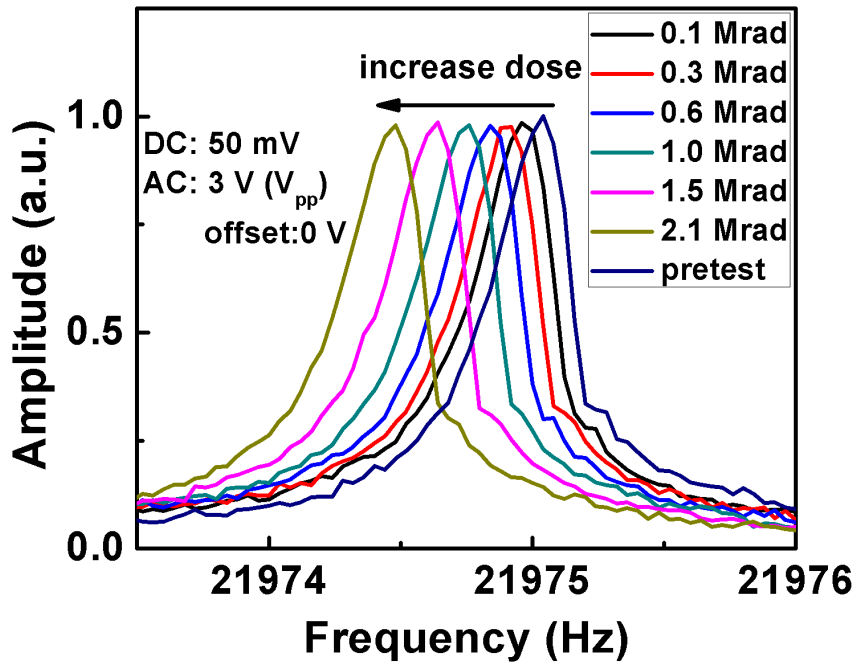


Fig. 46. Frequency sweeps after different total dose of X-ray radiation showing gradual shifting of resonance frequency as the total X-ray dose increases [1].

5.2 X-ray radiation experimental result

We radiated our resonators with 10keV X-ray at room temperature and at a pressure of 2×10^{-6} mbar. Fig. 45 shows the pre-radiation frequency sweeps over a frequency range that included the resonance frequency. It shows the consistency of our measurement setup. The setup was much less noisy than UV measurement, so we did not use reference device for X-ray experiments. We irradiated our heavily doped Si resonator with doping concentration of $5.8 \times 10^{18} \text{cm}^{-3}$ with high X-ray dose rate of 31.5krad/min(SiO_2). Fig. 46 shows the snapshots of frequency sweep at different stage of X-ray radiation with different total doses. The resonance frequency continued to decrease as the total dose was increased. And after 2.1Mrad total dose resonance frequency was

changed by approximately 25.48 ppm (0.56Hz) as shown in Fig. 47. The device recovered nearly to its initial state after about 9 hours of annealing.

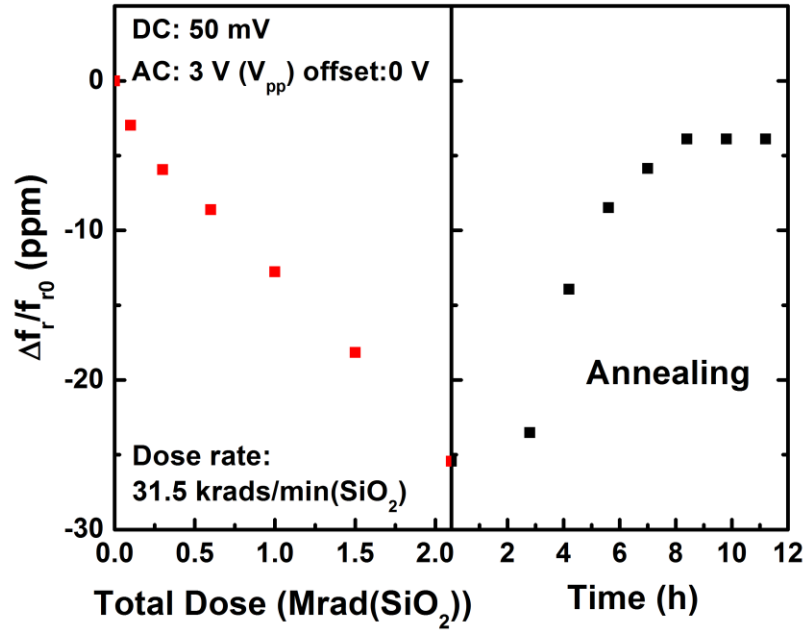


Fig. 47. Ppm change in resonance frequency as a function of total dose(left) and as a function of post-radiation anneal time (right) [1].

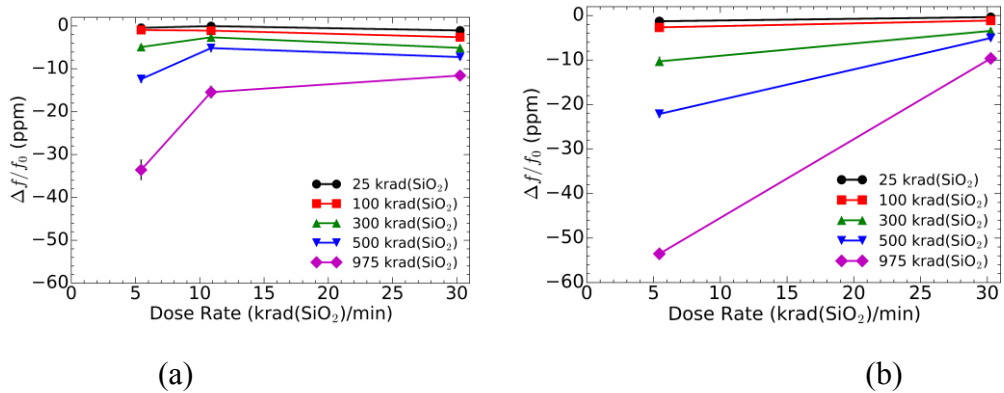


Fig. 48. (a) Ppm change in resonance frequency as a function of dose rate for (a) non-hydrogenated and, (b) hydrogenated devices [16].

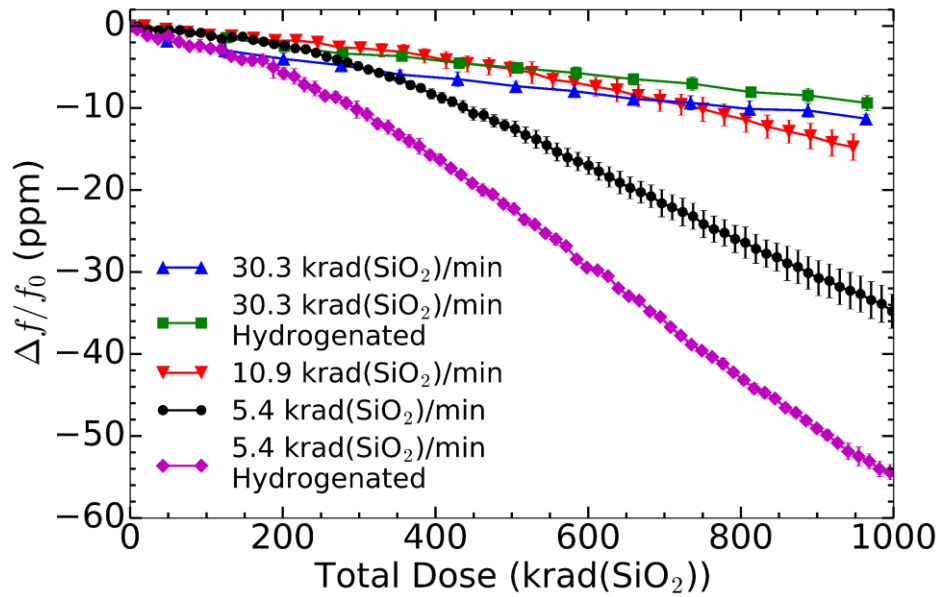


Fig. 49. (a) Symmetric and, (b) Asymmetric MEMS cantilever piezoresistor with dimensions [16].

5.2.1. Effect of dose rate

The resonators were exposed to X-rays at different dose rates to investigate the dose rate dependence. Furthermore, to explore the effect of hydrogen content in our resonators, we irradiated hydrogenated devices where extra hydrogen was introduced in the silicon by putting them in a steam bath for an hour before X-ray exposure. The non-hydrogenated devices were exposed to 5.4 krad/min(SiO₂), 10.9 krad/min(SiO₂) and 30.3 krad/min(SiO₂) dose rates of X-ray for a total dose of 1Mrad as shown in Fig. 49. On the other hand, hydrogenated devices were irradiated with 5.4 krad/min(SiO₂) and 30.3 krad/min(SiO₂) dose rates. The resonance frequency shifted less as the dose rate was increased for both hydrogenated and non-hydrogenated devices. At the high dose rate, the frequency shift of hydrogenated and non-hydrogenated devices was comparable (≈ 10 ppm) but for low dose rate (5.4 krad/min(SiO₂)) hydrogenated devices showed a larger shift (57% more) than their non-hydrogenated counterparts. Fig. 48 shows the ppm change in resonance

frequency as a function of dose rate for non-hydrogenated and hydrogenated devices at different total doses of X-ray. The plots show that at low dose rate the resonance frequency shifts more compared to high dose rate as the total dose increases beyond certain values. Fig. 50 shows the ppm change in resonance frequency as a function of time during radiation and during annealing. The annealing start time is indicated by markers. During annealing, the resonance frequency keeps decreasing (post-radiation degradation) for certain amount of time before starting to recover towards its original value. This post-radiation degradation period is different for different dose rates. Within 11 hours from the start of the radiation, all the devices' resonance frequencies increased beyond their original values. The excess increase in resonance frequency can be related to the pressure change due to continuous pump-down as shown in Fig. 51. The Fig. 51 shows un-irradiated devices' resonance frequency change due to pump-down (decrease in pressure) only and irradiated devices' resonance frequency change due to both pump-down and radiation. The two traces seem to meet after the annealing of the irradiated device indicating that the effect of radiation is to lower the resonance frequency temporarily. And the resonance frequency increase beyond starting value was caused by the continuous pump-down that reduces the pressure in the chamber slightly over time.

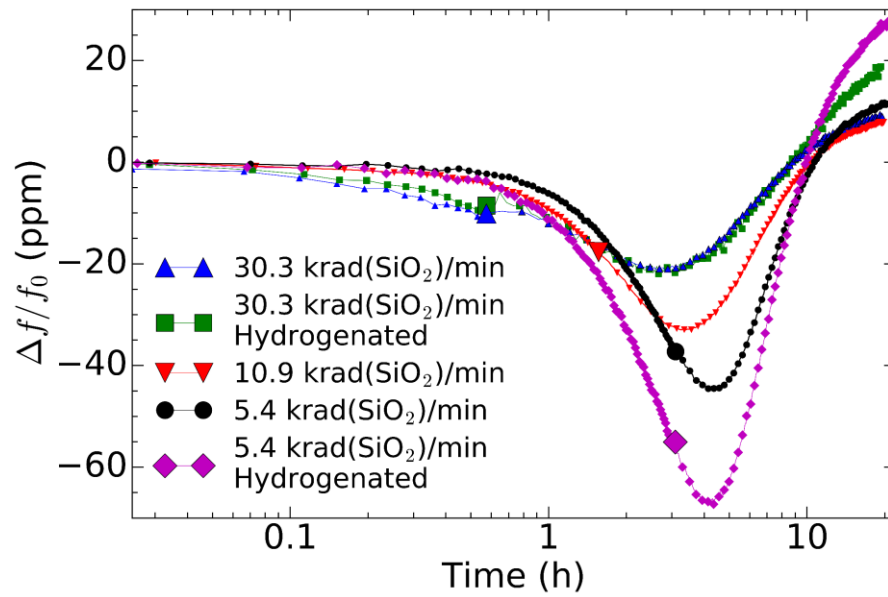


Fig. 50. Time evolution of in-situ and post-radiation resonance frequency shift. The radiation began at time, $t = 0$ and the radiation ended at different times that are indicated by markers for different dose rates [16].

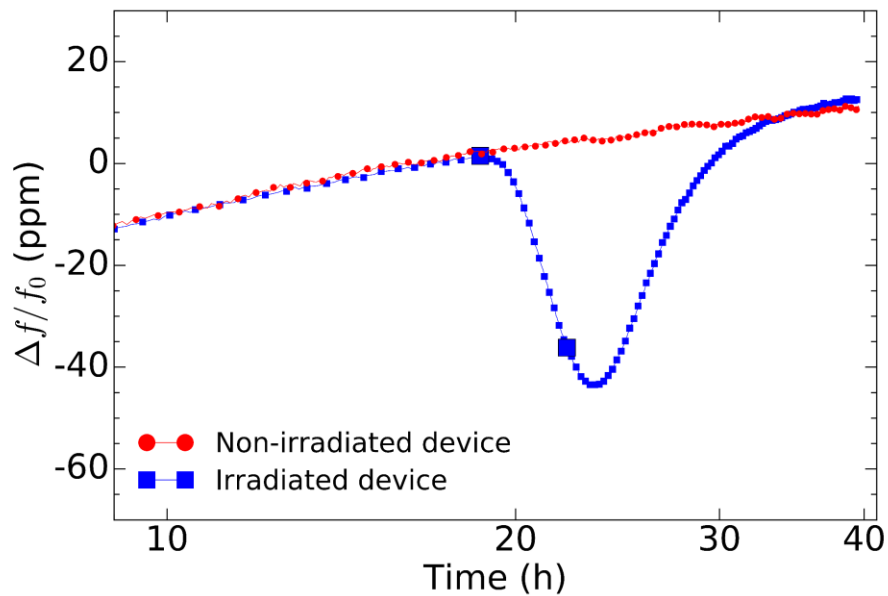


Fig. 51. Comparison of irradiated (at 5.4 krad/min(SiO_2)) and un-irradiated device resonance frequency shift characteristics as a function

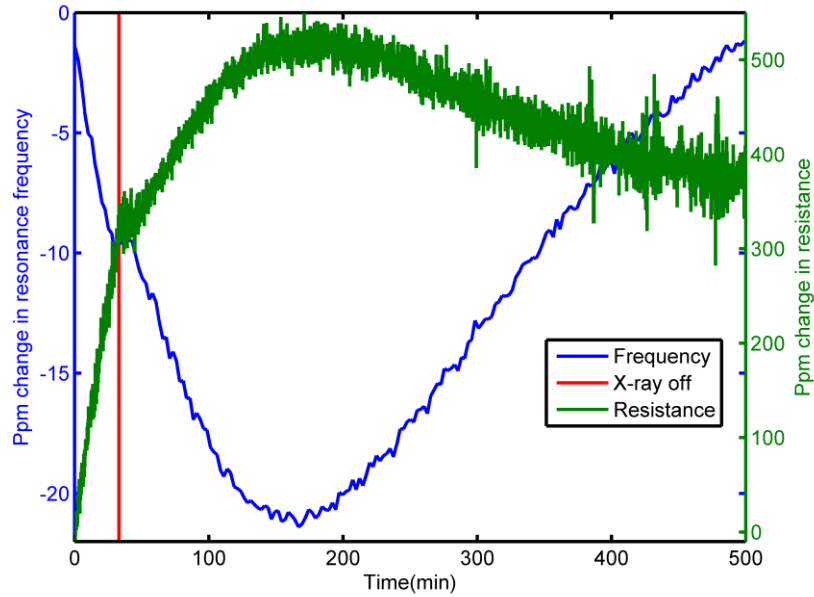


Fig. 52. Ppm change in resonance frequency and ppm change in 4-wire resistance in a heavily doped ($5.8 \times 10^{18} \text{cm}^{-3}$) p-type resonator during and after radiation (red line separates the in-situ and anneal data) for 30.26krad X-ray exposure for about 33 minutes.

5.2.2. Effect on base resistance

Fig. 52 shows the ppm change in resonance frequency and the ppm change in 4-wire base resistance in a heavily doped ($5.8 \times 10^{18} \text{cm}^{-3}$) p-type resonator during 30.26keV X-ray radiation for about 33 minutes and during annealing. The resistance and resonance frequency measurements were conducted on two separate devices that were made of the same type of Si substrate. Unlike the resonance frequency change, the base resistance increased during radiation, but the changes in resonance frequency and 4-wire base resistance looks highly correlated despite being in opposite directions. Fig. 54 shows that the slope of resistance change vs resonance frequency change for different dose rates are similar for both non-hydrogenated and hydrogenated devices. But the slope is dissimilar

between hydrogenated and non-hydrogenated devices with hydrogenated devices having steeper slope. It indicates that for hydrogenated devices resonance frequency changed more for a given change in base resistance compared to non-hydrogenated devices.

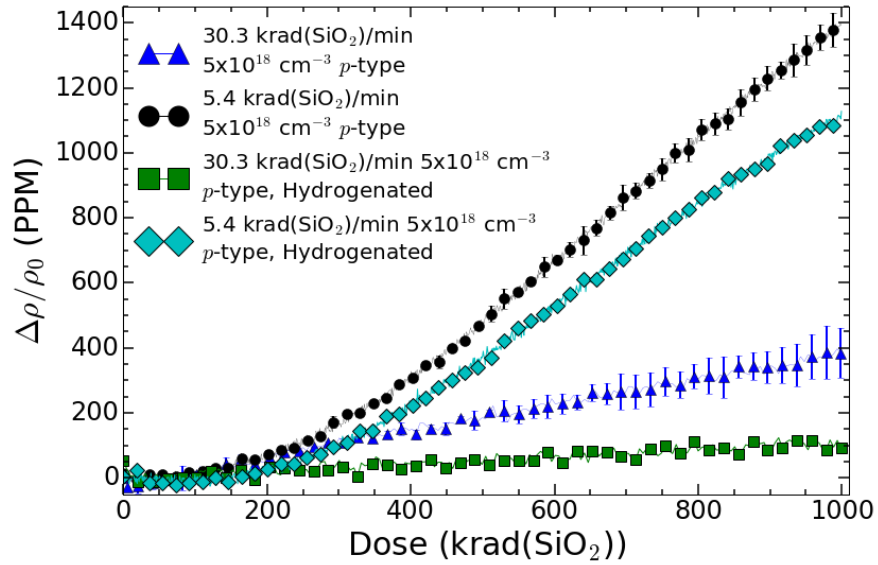


Fig. 53. Dose rate dependence of base resistivity as a function of total dose for non-hydrogenated and hydrogenated devices.

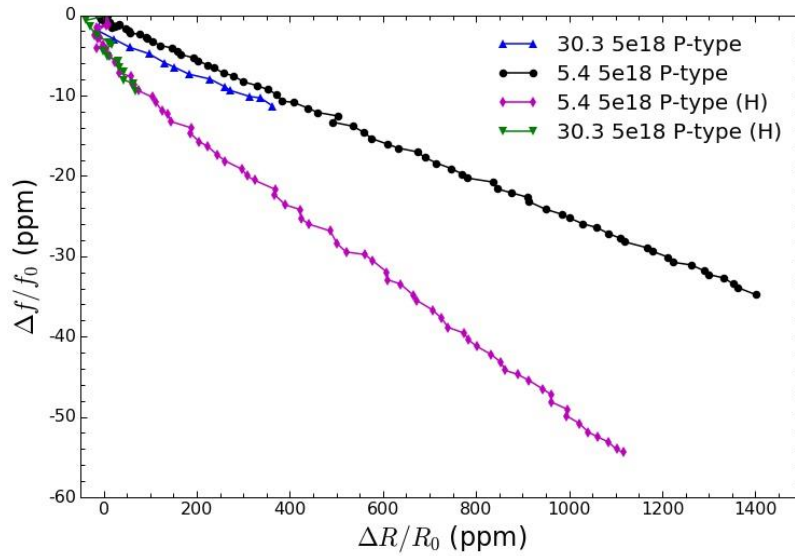
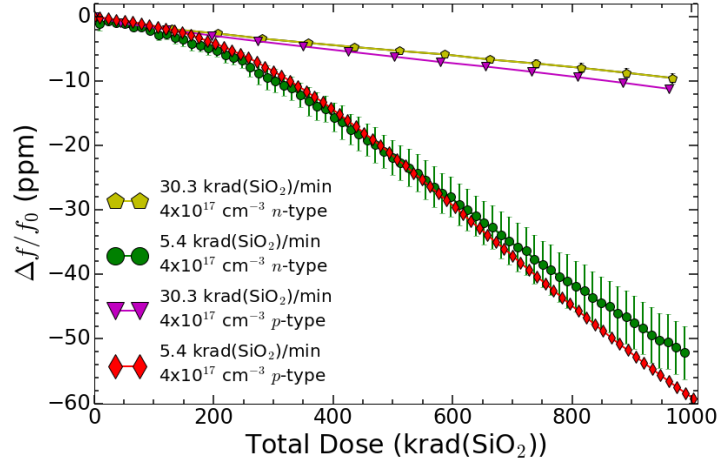
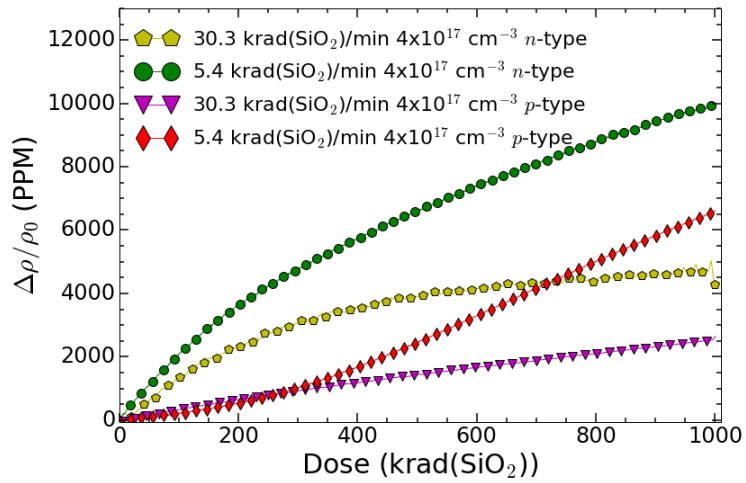


Fig. 54. Resistance change vs. resonance frequency change for different dose rates for both non-hydrogenated and hydrogenated (denoted by “(H)” in the legend) devices.

Base resistivity also shows dose-rate dependence as shown in Fig. 53 for hydrogenated and non-hydrogenated devices. Again, in contrast with resonance frequency, the base resistivity changes more in non-hydrogenated devices compared to hydrogenated devices for both dose rates. The low dose-rate radiation caused a larger shift in base resistivity compared to the high dose rate radiation.



(a)



(b)

Fig. 55. Comparison of low carrier concentration ($3.68 \times 10^{17} \text{cm}^{-3}$) p-type and ($3.62 \times 10^{17} \text{cm}^{-3}$) n-type Si resonators' (a) resonance frequency shift and, (b) 4-wire base resistance shift under different doses of X-ray radiation.

5.2.3. Effect of doping type

To investigate the effect of dopant types on the resonance frequency change and 4-wire base resistance change under X-ray radiation, we radiated low carrier concentration p-type and n-type 8 μm wide Si resonators with 30.3krad/min(SiO_2) and 5.4krad/min(SiO_2)

dose rate X-ray. As shown in Fig. 55, the ppm change in resonance frequency is similar in n-type and p-type devices for both high and low dose-rate X-ray radiation. On the other hand, base resistance change is much higher at both dose-rates for n-type devices compared to p-type.

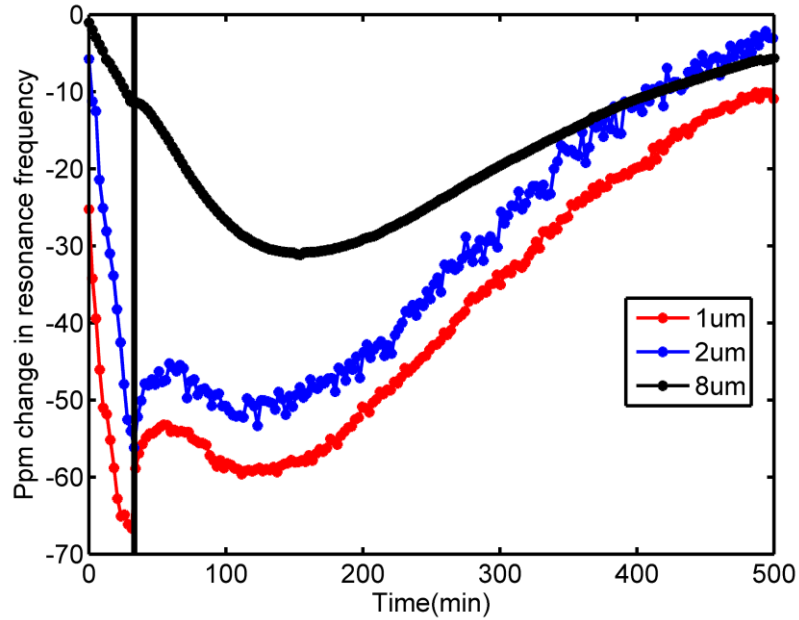
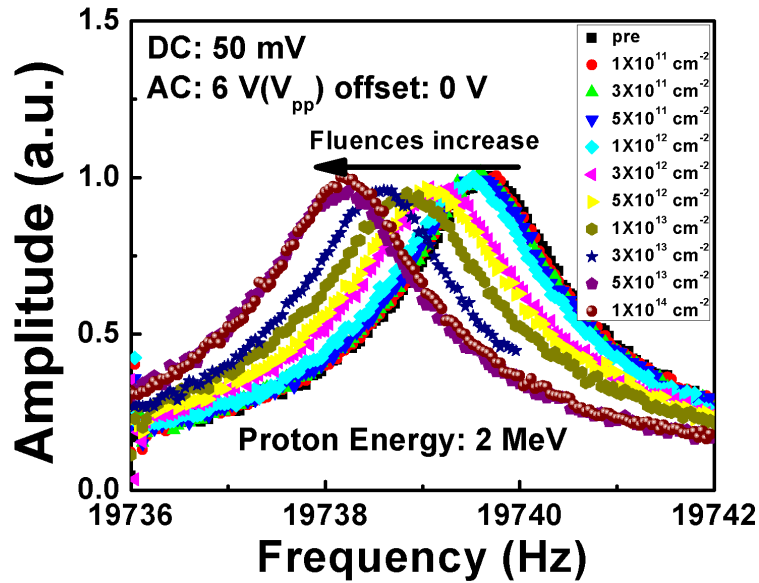


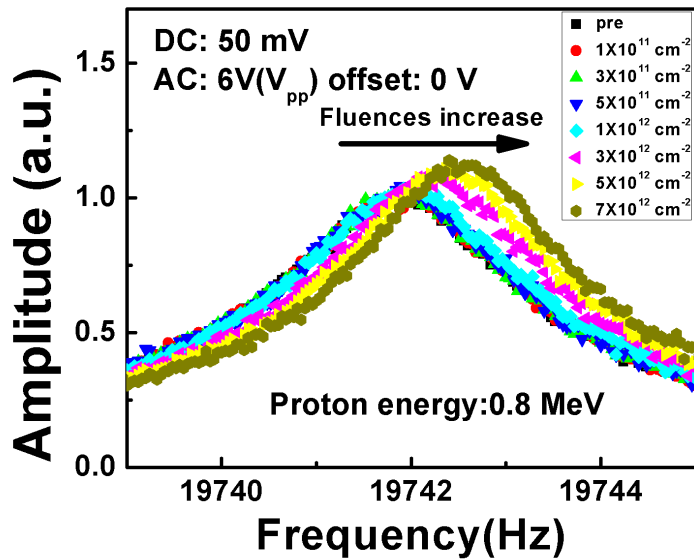
Fig. 56. Width dependence of resonance frequency shift with respect to time. The vertical black line separates the insitu and annealing data.

5.2.4. Effect of beam width

Resonators with three different beam widths ($1\mu\text{m}$, $2\mu\text{m}$ and $8\mu\text{m}$) were radiated with $30.26\text{krad/min}(\text{SiO}_2)$ dose-rate X-ray for about 33 minutes. Similar to UV result, smaller beam width devices showed larger changes in resonance frequencies. Also, the post-radiation degradation is different for smaller width devices where the resonance frequency change oscillates immediately after turning off the radiation and does not decrease below the maximum change observed during radiation.

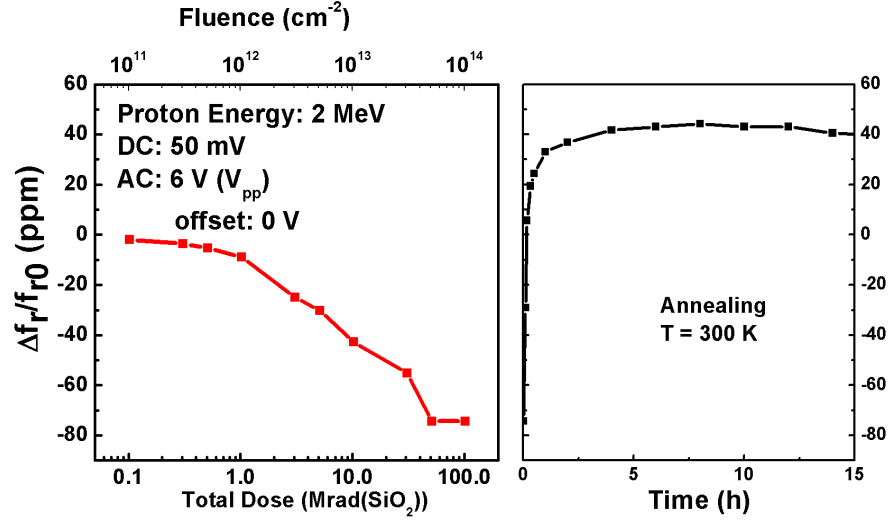


(a)

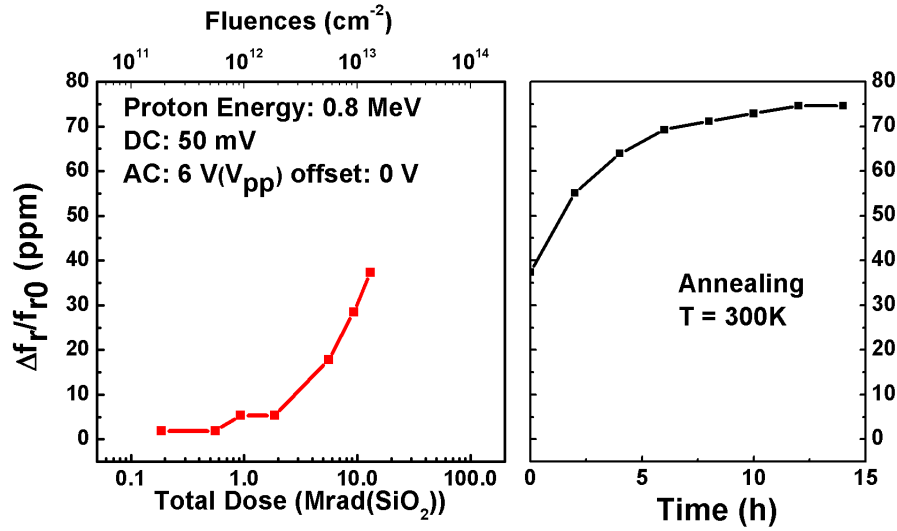


(b)

Fig. 57. Frequency sweep snapshots for different fluences of proton radiation with (a) 2MeV proton and, (b) 0.8 MeV proton. The plots show that the resonance frequency decreases for high energy proton radiation while increases for low energy proton radiation [2].



(a)



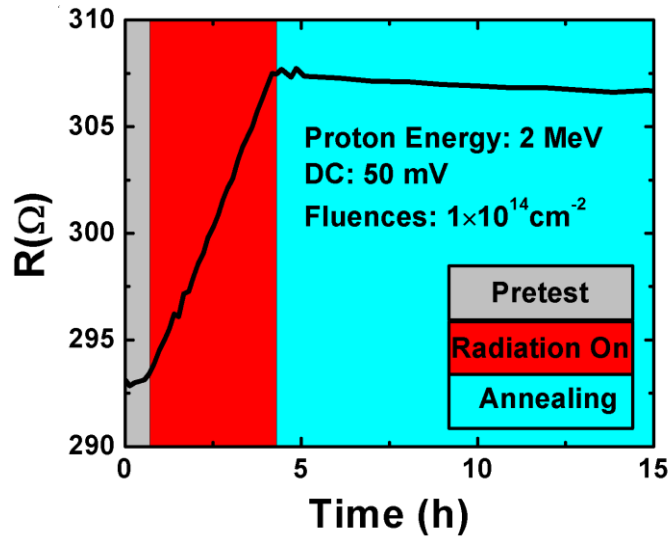
(b)

Fig. 58. Ppm change in resonance frequency as a function of total ionizing dose (bottom x-axis) and fluences (top x-axis) and, subsequent annealing as a function of time for (a) 2 MeV proton radiation and (b) 0.8 MeV proton radiation [2].

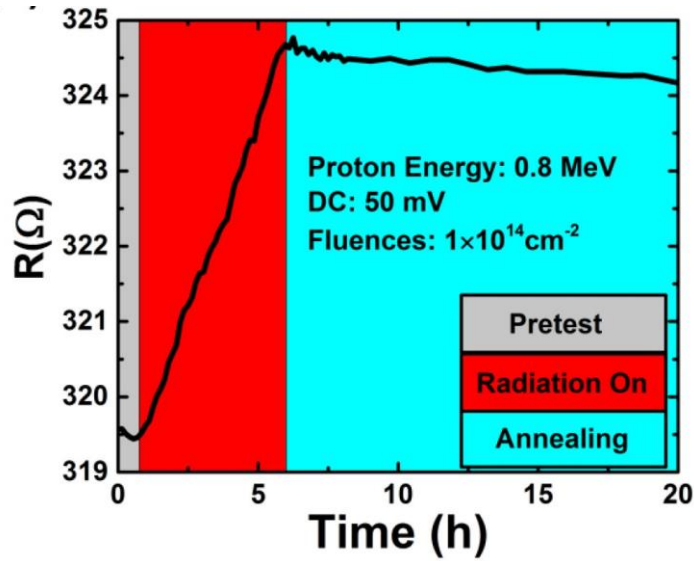
5.3 Proton radiation experimental result

Resonators were irradiated by protons of two different energies: 2 MeV and 0.8 MeV for TID (Total Ionizing Dose) of about 100Mrad and 10Mrad respectively. Fig. 57 shows that for high energy (2MeV) proton radiation, resonance frequency decreases with increase in proton fluence. On the contrary, for low energy (0.8 MeV) proton radiation, resonance frequency increases with increase in proton fluence. (b)

Fig. 58 shows the shift in resonance frequency as a function of total ionizing dose (TID) and proton fluence during 2MeV and 0.8MeV proton radiation. The figure also shows the annealing behavior of the radiated devices. High energy proton (2MeV) radiation was conducted for TID of about 100Mrad that caused the resonance frequency to decrease by approximately 72 ppm. On the other hand, low energy proton (0.8MeV) radiation was conducted for about 10Mrad that caused a resonance frequency increase of about 37 ppm. During annealing, the 2MeV proton radiated sample showed a large increase in resonance frequency that surpassed its starting value (initial value before radiation) by about 40ppm. The resonance frequency of 0.8MeV proton radiated sample further increased during annealing and after 15 hours of annealing the total shift in resonance frequency was about 75 ppm.



(a)



(a) (b)

Fig. 59. Resonator 2-wire base resistance decreases for both 2 MeV and 0.8 MeV proton radiation and in both cases the resistance persistently stays high during annealing [2].

Base resistance increased during radiation for both types of proton radiation and the resistances recovered only a little during the observed period of anneal time as shown in Fig. 59.

5.4 Conclusion

We characterized the radiation damage with respect to change in resonance frequency and base resistance. In general, UV and X-ray causes temporary damage whereas proton radiation causes permanent damage to the resonator. Recovery time after UV radiation (typically ≈ 70 hrs) is longer compared to X-ray radiation (typically ≈ 1 hrs). X-ray radiation damage showed dose-rate dependence. We also showed doping type and doping concentration dependence of UV and X-ray radiation damage. The surface-to-volume ratio of the resonators were changed by changing the width of the center cantilever. For UV and X-ray radiation experiments, resonators of three different widths, viz., $1\mu\text{m}$, $2\mu\text{m}$ and $8\mu\text{m}$, were radiated and smaller width devices have shown greater radiation damage. We observed post-radiation behavior of proton-radiated samples for about 15 hours and by this time the resonance frequency reached its new stable value which is significantly higher than its pristine value before radiation which indicates permanent damage. In the next chapter, we will use our presented theory of previous chapter to explain the experimental observations presented in this chapter.

CHAPTER VI

THEORETICAL MODELS AND DISCUSSIONS

In this chapter, I presented several theoretical models that explain the observed experimental results. At first, I discussed about the spring softening effect and the gas adsorption effect on the resonance frequency change. I also derived the expected change in resistance during radiation due to photogeneration, using continuity equation. I analyzed the experimental data from UV and X-ray radiation experiments in reference to native oxide charging and hydrogen-dopant complex dissociation models, respectively. Finally, the proton radiation damage is explained with respect to competing effect of ionization and displacement damage.

All three types of radiation--UV, X-ray and proton radiation--causes significant damage to the tested MEMS resonators. But the damage mechanisms are different for different kinds of radiation. I will discuss about the extent to which our theoretical models explain and fit the experimental data. Origin of surface-to-volume ratio dependence of radiation damage will also be explained for both UV and X-ray. Proton radiation data will be analyzed to show the relative contribution of the ionization and displacement damage in the total radiation damage for two different proton energies.

6.1 Model of UV radiation damage

UV radiation creates lots of electron-hole pairs in silicon since UV photon has much higher energy than the bandgap of Si. The excess free carriers change the resistivity and resonance frequency of the irradiated sample. Native oxide, defects and surface states traps some excess carriers and makes the change to persist for long time after UV is turned off. Excess surface charge modifies the local electric field which causes spring softening effect. Spring softening decreases the resonance frequency. Surface charges can also attract surrounding ionized gas molecules: causing them to adsorb on the surface. Adsorbed gas adds to the mass of the cantilever so the resonance frequency decreases. The contribution of those mechanisms to the change in material properties are investigated in this section.

6.1.1. Spring softening

It is well known that silicon grows about 2-3 nm of native oxide on the surface when exposed to air for enough time (at room temperature and pressure). UV exposure creates electron-hole pairs on the exposed silicon surface some of which get trapped in the native oxide. In the article, the free-standing cantilever resonator is sitting on a substrate with cavity of dimension $705 \mu\text{m} \times 160 \mu\text{m}$ where lateral sides of the cantilever are approximately $80 \mu\text{m}$ away from the cavity walls. Upon UV exposure, both the cantilever and the substrate accumulate charges on their native oxide layer. Charged oxides creates electrostatic force between the substrate and the freestanding cantilever that leads to the spring softening effect.

The general equation of motion of the cantilever excited by an alternating force can be expressed by equation (60) where $F_{drive}(x, t)$ and $F(x)$ represents the driving force and the force causing spring softening effect, respectively. Parameters m and k are the

generalized mass and generalized spring constant of the equivalent lumped parameter model of the cantilever.

$$m\ddot{x} + b\dot{x} + kx = F_{drive}(x, t) + F(x) \quad (60)$$

The electrostatic force due to charged oxide is distributed along the length of the cantilever and can easily be converted to an equivalent force acting on the tip of the cantilever. If $w(x)$ is the distributed electrostatic force and l is the length of the cantilever, the spring softening force $F(x)$ can be expressed by equation (61) where $\frac{3w(x)l}{8}$ is the equivalent force acting on the tip of the cantilever [106].

$$F(x) = \frac{3w(x)l}{8} = k'x \quad (61)$$

Parameter k' in equation (61) quantifies the amount of spring softening and can be directly subtracted from the spring constant of the system. So, the general equation of motion can be rewritten as follows:

$$m\ddot{x} + b\dot{x} + (k - k')x = F_{drive}(x, t) \quad (62)$$

The resonant frequency can now be expressed as,

$$f_s = \frac{1}{2\pi} \sqrt{\frac{k - k'}{m}} \quad (63)$$

So, a reduction of resonance frequency occurs due to the electrostatic force generated by the trapped charges in the oxide.

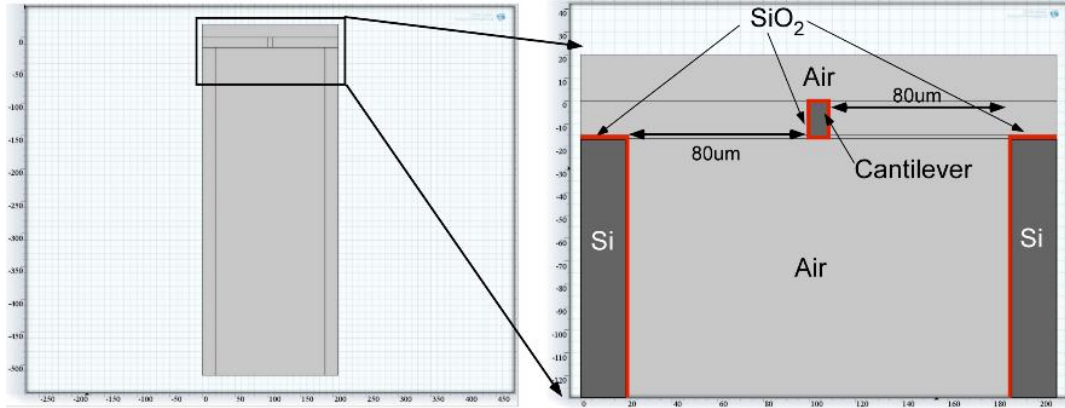


Fig. 60. 2D model used for COMSOL simulation to find electrostatic force per unit length due to charged oxide. Charged oxide areas are marked in red.

The amount of frequency reduction due to the electrostatic force exerted by the charged oxide was calculated with the help a 2D finite element model simulation. The simulation was conducted using COMSOL Multiphysics (a finite element simulation software) to find the electrostatic force per unit length of the cantilever at different positions of the cantilever above the cavity. The simulation model consisted of cross section of the cantilever and the cavity walls as shown in Fig. 60. A thin oxide layer was placed on all exposed silicon surface. Surface charge of $6.25 \times 10^{12} \text{ cm}^{-2}$ was placed on the oxide layers.

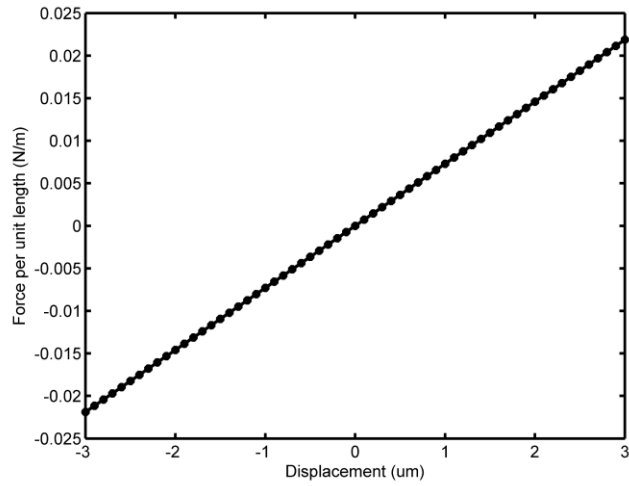
The dimension of the model prohibited the use of 2nm oxide layers in the simulation. So, a group of simulation was carried out with different oxide thicknesses to find the 2nm oxide thickness result by extrapolation. Fig. 61(a) shows a typical result, obtained using $1 \mu\text{m}$ thick oxide layer, that plots electrostatic distributed force per unit length with respect to displacement of the cantilever from center zero position. The slope of this plot helps us to calculate the spring softening parameter k' . Finally, using equation (4) new resonance frequency can be calculated that accounts for spring softening effect. Fig. 61(b) shows extrapolation of the simulation data to find slope that corresponds to 2nm

oxide but lack of data at smaller oxide thicknesses made it difficult to extrapolate with good accuracy.

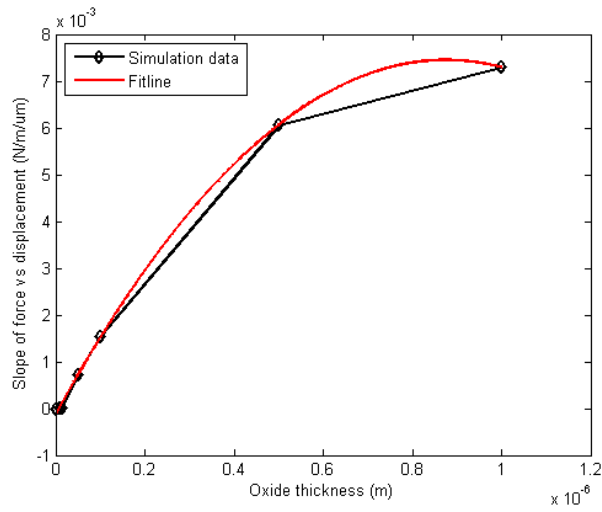
Table 9: Resonance frequency change for different oxide thicknesses

Oxide thickness	k' (N/m)	Frequency shift(Hz)	Ppm change in frequency
100nm	3.799	-1045.6	-40756
50nm	0.176	-480	-18712
15nm	1.85×10^{-3}	-4.99	-194
2nm	$<2.46 \times 10^{-5}$	<-0.07	<-2

Table 9 shows ppm change in resonance frequency for different oxide thicknesses. Looking at the trend in reduction of ppm change with oxide thickness, we predict the shift of resonance frequency will be less than 2 ppm due to spring softening at 2nm oxide thickness which is significantly lower compared to what was observed during UV exposure.

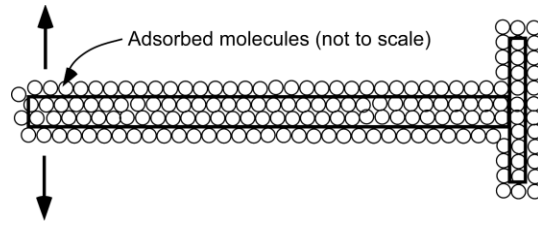


(a)

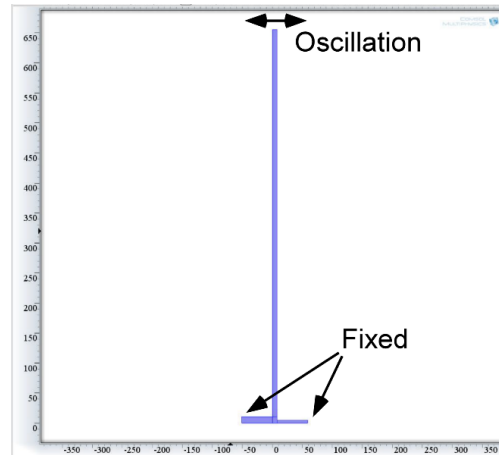


(b)

Fig. 61. (a) Electrostatic force per unit length of the cantilever vs. displacement from center of the cavity, (b) extrapolation of simulation data to find the slope of force vs. displacement plot for 2nm thick oxide.



(a)



(b)

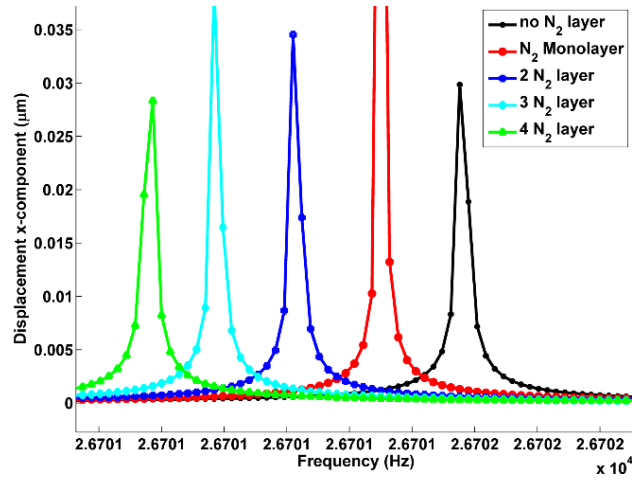
Fig. 62. (a) Schematic illustration of the gas adsorption on the cantilever, (b) cantilever model used in the 2D simulation.

6.1.2. Gas adsorption on surface

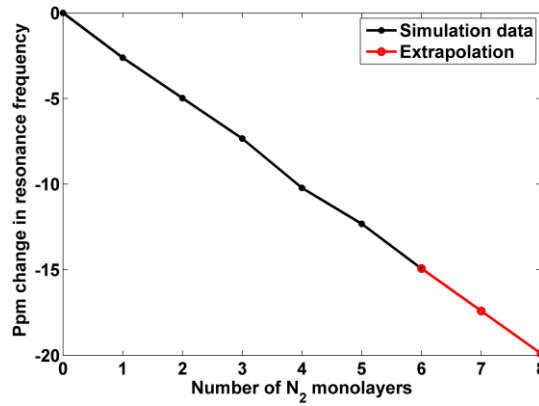
UV radiation can ionize the residual gases in a vacuum chamber. The ionized gas molecules can potentially get adsorbed on the surface of the cantilever. As a result, the effective mass of the cantilever gets changed that causes a shift in resonance frequency of the cantilever. Equation (64) shows the resonance frequency of the cantilever obtained by representing the cantilever as a simple mass-spring-dashpot lumped parameter model where m_{eff} and k_{eff} are the effective mass and effective spring constant of the system respectively. It is obvious from the equation that an increase in mass will cause the resonance frequency to decrease.

(64)

$$f_0 = \frac{1}{2\pi} \sqrt{\frac{k_{eff}}{m_{eff}}}$$



(a)



(b)

Fig.63. (a) Displacement vs. driving frequency for different amount of mass added to the cantilever, (b) Resonance frequency plotted against added monolayers of N₂ mass. About 8 monolayers need to be adsorbed on the cantilever to cause 20 ppm change in resonance frequency.

A 2D mechanical simulation using COMSOL was carried out to find the amount of shift in resonance frequency observed for a change in the mass of the cantilever. For simplicity, the dimension of the cantilever was kept fixed while the mass of the cantilever

was changed. The mass was incremented by the amount of one monolayer of N₂ adsorbed uniformly surrounding the exposed surface of the cantilever as shown in Fig. 62(a). The actual model used in the simulation is shown in Fig. 62(b) where few boundary conditions are also noted. Frequency domain analysis was carried out with a boundary condition of applied alternative force at the tip of the cantilever. The simulation gives us the resonance frequency in the form of peak displacement in a frequency sweep as shown in Fig.63(a). Ppm change in resonance frequency is plotted against number of monolayers adsorbed on the cantilever surface in Fig.63(b). It is observed that more than 8 monolayers of N₂ need to be adsorbed to increase the cantilever mass sufficiently to cause same order magnitude change (> 20ppm) in resonance frequency that was observed during UV exposure. So, gas adsorption should not be the dominant effect that contributes to the resonance frequency shift during UV exposure.

6.1.3. Resistance change due to photocarriers

UV radiation corresponds to about 100nm to 400nm wavelength in the electromagnetic spectrum [107]. At this wavelength range, all the radiation is absorbed close to the surface (<100nm) as shown in Fig. 64 [108]. The energy range of UV is about 3eV to 12eV. UV readily ionizes the silicon by transferring electrons from its valence band to conduction band and reduces the resistivity of the irradiated sample. At equilibrium, the resistance change due to photocarriers can be calculated using continuity equation that gives us the net effect due to carrier generation and recombination [55].

Let us consider the case of resistance change due to excess hole generated by UV radiation of wavelength 255nm: on a highly doped p-type wafer. Equation (65) shows the continuity equation for excess holes where D_p is the hole diffusion coefficient, δp is the excess

hole concentration, τ_A is augur time constant, L_A is absorption length, G_0 is generation rate at the surface. and y is positive downwards (Fig. 8(a)).

$$-\frac{1}{q}D_p \frac{d^2 \delta p}{dy^2} - \frac{\delta p}{\tau_A} + G_0 \exp\left(-\frac{y}{L_A}\right) = 0 \quad (65)$$

Table 10: Parameter values used in photocarrier generation calculation

	Symbol	Value	Unit
Augur coefficients [9]	c_n	2.8×10^{-31}	cm^6s^{-1}
	c_p	9.9×10^{-32}	cm^6s^{-1}
Parameters of Arora model [17] for mobility	μ_n^{min}	88.3	$\text{cm}^2\text{V}^{-1}\text{s}^{-1}$
	μ_p^{min}	54.3	$\text{cm}^2\text{V}^{-1}\text{s}^{-1}$
	μ_n^{max}	1330.3	$\text{cm}^2\text{V}^{-1}\text{s}^{-1}$
	μ_p^{max}	461.2	$\text{cm}^2\text{V}^{-1}\text{s}^{-1}$
	N_n^{ref}	1.295×10^{17}	cm^{-3}
	N_p^{ref}	2.35×10^{17}	cm^{-3}
	γ_n	0.891	-
	γ_p	0.88	-
Absorption length	L_A	5.255	nm
Surface recombination velocity	S	3.8×10^4	cm/s
Doping concentration	N_A	5.98×10^{18}	cm^{-3}
Conduction band effective Density of States	N_C	3.37×10^{19}	cm^{-3}
Valence band effective Density of States	N_V	1.83×10^{19}	cm^{-3}
Power of UV source	P	1.6	mW/cm^2
EHP generation per photon	M_{ph}	1.05	-

Auger time constant is calculated using the following expression:

$$\tau_A = \frac{1}{c_n n_0^2 + c_p p_0^2 + 2n_i^2(c_n + c_p)} \quad (66)$$

where c_n and c_p are Auger coefficients (from Table 10); and, n_0 and p_0 are electron and hole concentration respectively, at equilibrium at 300K.

Generation rate (G_0) is given by,

$$G_0 = \frac{I_{ph} M_{ph}}{L_A} \quad (67)$$

where I_{ph} is photon flux on the cantilever surface and M_{ph} is the number of electron-hole pair (EHP) generated per photon.

Flux of photon is calculated from power of incident UV radiation, P ; energy of the single UV photon, E_{ph} ; and, reflection coefficient, Γ_R as shown in equation (68) where $\Gamma_R = \left(\frac{1-\sqrt{\epsilon_{Si}}}{1+\sqrt{\epsilon_{Si}}}\right)^2$ is calculated using dielectric constant of silicon, $\epsilon_{Si} = 11.8$.

$$I_{ph} = \frac{P}{E_{ph}} (1 - \Gamma_R) \quad (68)$$

We found the excess carrier concentration profile by solving equation (65) given by,

$$\delta p(y) = C_1 \cos \sqrt{m}x + C_2 \sin \sqrt{m}x + \left(\frac{nL_A}{mL_A^2 + 1}\right) \exp\left(-\frac{y}{L_A}\right) \quad (69)$$

where $m = -\frac{1}{D_p \tau_A}$ and $n = \frac{-G_0}{D_p}$.

The coefficients C_1 and C_2 can be determined by using the following boundary conditions:

$$D_p \left. \frac{d\delta p}{dy} \right|_{y=0} = S\delta p(0), \text{ at } y = 0 \quad (70)$$

$$D_p \left. \frac{d\delta p}{dy} \right|_{y=H} = -S\delta p(H), \text{ at } y = H \quad (71)$$

where S is the surface recombination velocity and H is the height of the cantilever. We used the surfaced recombination velocity of non-passivated (100) oriented Si surface (3.8×10^4 cm/s) in our calculation.

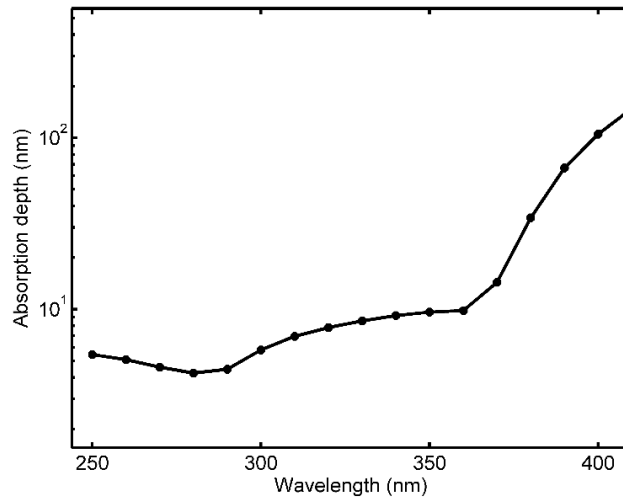


Fig. 64. Absorption depth of UV in silicon with respect to wavelength. Most of the UV is absorbed close to the surface.

Fig. 8 (b) shows excess hole concentration as a function of depth into the silicon from the top surface. Table 10 shows the parameter values that is used to calculate the excess carrier concentration profile. Silicon absorbs UV on the surface region (0nm -5nm) and generates lot of electron-hole pairs. An exponential excess carrier profile follows the generation region where the carriers diffuse into the Si and recombines along the way. The effect of high surface recombination velocity is evident in the inset of Fig. 8(b) where we

observe a dip in excess carrier concentration on the surface resulting in a buried peak at around 2nm.

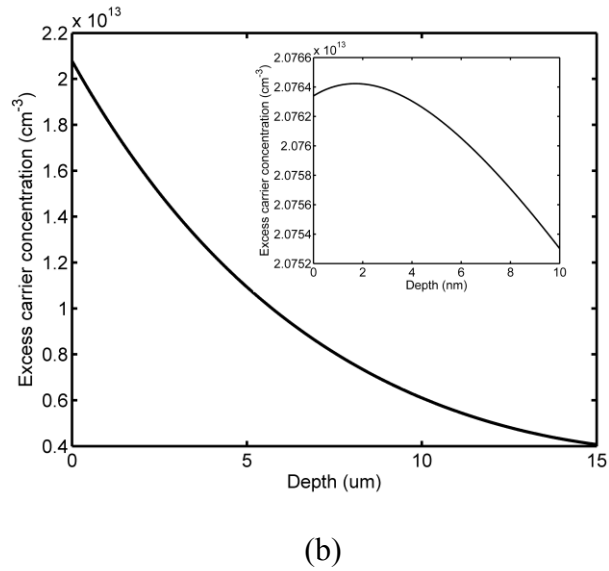
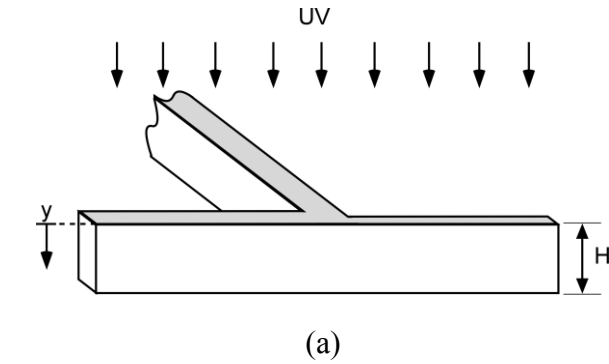


Fig. 65. (a) Schematic diagram of UV radiated cantilever showing the direction of radiation, (b) Excess carrier concentration across the cantilever starting from top surface. Si absorbs UV light at/near the surface (up to ≈ 10 nm depth) and generates lots of excess carriers. Surface recombination lowers the concentration at the surface (shown in inset figure).

We can calculate the average change in hole concentration, Δp by integrating over the excess hole concentration and dividing by the height of the cantilever as shown below:

$$\Delta p = \frac{1}{H} \int_0^H \delta p \, dy \quad (72)$$

Since electron and holes are generated in pairs by UV, average change in electron concentration, $\Delta n = \Delta p$.

We found the hole mobility, μ_p and electron mobility, μ_n using Arora model [17] using the following expressions:

$$\mu_p = \mu_p^{min} + \frac{\mu_p^{max} - \mu_p^{min}}{1 + \left(\frac{N_A}{N_p^{ref}}\right)^{\gamma_p}} \quad (73)$$

$$\mu_n = \mu_n^{min} + \frac{\mu_n^{max} - \mu_n^{min}}{1 + \left(\frac{N_A}{N_n^{ref}}\right)^{\gamma_n}} \quad (74)$$

The model parameters at 300K are listed in Table 10.

So, the excess carrier modified new resistivity of the cantilever base is given by,

$$\rho_{uv} = \frac{1}{q\mu_n(n_0 + \Delta n) + q\mu_p(p_0 + \Delta p)} \quad (75)$$

Table 11: Results of photocarrier generation calculation for different UV wavelengths

UV wavelength(nm)	Incident power (mW/cm ²)	Average excess carrier concentration, $\Delta n = \Delta p$ (cm ⁻³)	Ppm change in resistance
255	1.6	1.488×10^{10}	0.0065
275	0.4	3.898×10^9	0.0017
365	113.57	1.487×10^{12}	0.6636

The T-shaped cantilever base consists of two section: thick arm of dimension $51 \mu\text{m} \times 11 \mu\text{m} \times 15 \mu\text{m}$ and thin arm of dimension $51 \mu\text{m} \times 5 \mu\text{m} \times 15 \mu\text{m}$. New resistance of the base, R_{uv} is calculated with the modified resistivity and compared with the resistance

before the radiation and we found 0.006 parts per million (ppm) change in resistance due to photocarriers induced by UV radiation.

Similar calculation was carried out for UV radiation of different wavelengths and different intensities: the results are summarized in Table 11. We observe that the change in resistance due to photocarriers is small and the change should be attained very quickly after turning on/off the UV source since the Auger time constant is very small (2.825×10^{-7} s).

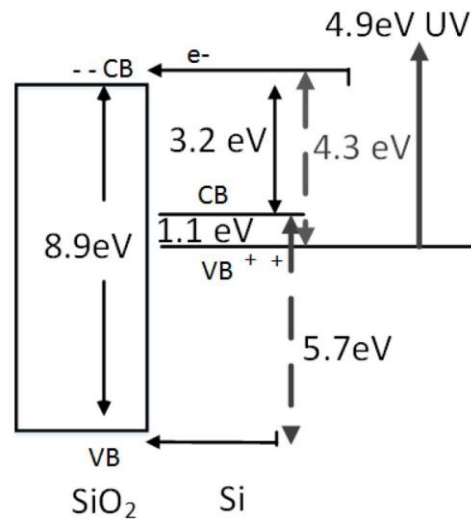


Fig. 66. Band diagram of silicon and silicon dioxide showing the relative energy difference between conduction and valence bands.

6.1.4. Trapping of photocarriers at native oxide

We know that exposed silicon grows thin layer (2-3nm) of oxide on the surface very quickly. This thin oxide film can play a huge role at separating charges generated due to radiation. From previous section, we noticed that the change in resistance for photocarriers is small even for the High energy UV (wavelength < 288nm) that can transfer electron to the conduction band of silicon dioxide from silicon's valence band. Additionally, UV with shorter wavelength (<217nm) can also transfer electrons from

valence band of SiO₂ to conduction band of silicon (Fig. 66). Once carriers get transferred to oxide from silicon, it gets trapped and takes a long time to diffuse back to silicon. Surface states at the Si-SiO₂ interface also traps carriers. As a result, we expect to see persistent photoconductivity after UV radiation that persists for a long time [109] before it recovers back to its original condition. Essentially, the charge separation at the Si/SiO₂ interface creates an electric field at the surface of the cantilever. The field penetrates Si and get terminated by the charges inside the silicon.

Based on the nature of the electric field, the silicon surface might go to accumulation, depletion or strong inversion to accommodate the charges that terminates the surface electric field. So, free carrier concentration changes in that region and the energy bands (conduction band, valence band and intrinsic energy level) bend near the surface. We can find the bending potential, $\psi(x)$ by solving Poisson's equation given by equation (76), where $\psi(x) = 0, at x = \infty$ and $\psi(x) = \psi_s, at x = 0$ [55].

$$\frac{d^2\psi}{dx^2} = -\frac{q}{\epsilon_{Si}} [p(x) - n(x) + N_d^+ - N_a^-] \quad (76)$$

In uniformly doped uncompensated silicon, N_d^+ and N_a^- depends only on the doping concentration and can be approximated by bulk (at $x = \infty$ in equilibrium) carrier concentrations n_0 and p_0 , respectively. And, ϵ_{Si} represents the dielectric constant of Si given by $\epsilon_{Si} = 11.8\epsilon_0$, where ϵ_0 is the electric permittivity in vacuum. Carrier concentrations $p(x)$ and $n(x)$ can be expressed as a function of potential given by,

$$p(x) = p_0 \exp\left(-\frac{q\psi(x)}{kT}\right) \quad (77)$$

$$n(x) = \frac{n_i^2}{p_0} \exp\left(\frac{q\psi(x)}{kT}\right) \quad (78)$$

where k is the Boltzmann constant and n_i is intrinsic carrier concentration.

Replacing $p(x)$ and $q(x)$ in equation (76) and integrating, we get the following expression for a uniformly doped p-type silicon:

$$\begin{aligned} \frac{d\psi}{dx} &= -\left(\frac{2kTp_0}{\epsilon_{Si}}\right)^{\frac{1}{2}} \left[\left(e^{-\frac{q\psi(x)}{kT}} + \frac{q\psi(x)}{kT} - 1 \right) + \frac{n_0}{p_0} \left(e^{\frac{q\psi(x)}{kT}} - \frac{q\psi(x)}{kT} - 1 \right) \right]^{\frac{1}{2}} \\ &= f(\psi(x)) \end{aligned} \quad (79)$$

where $f(\psi(x))$ shortly represents the right-hand term of equation (79). If we rearrange the above equation and integrate, we find:

$$x = \int_{\psi_s}^{\psi(x)} \frac{d\psi(x')}{f(\psi(x'))} \quad (80)$$

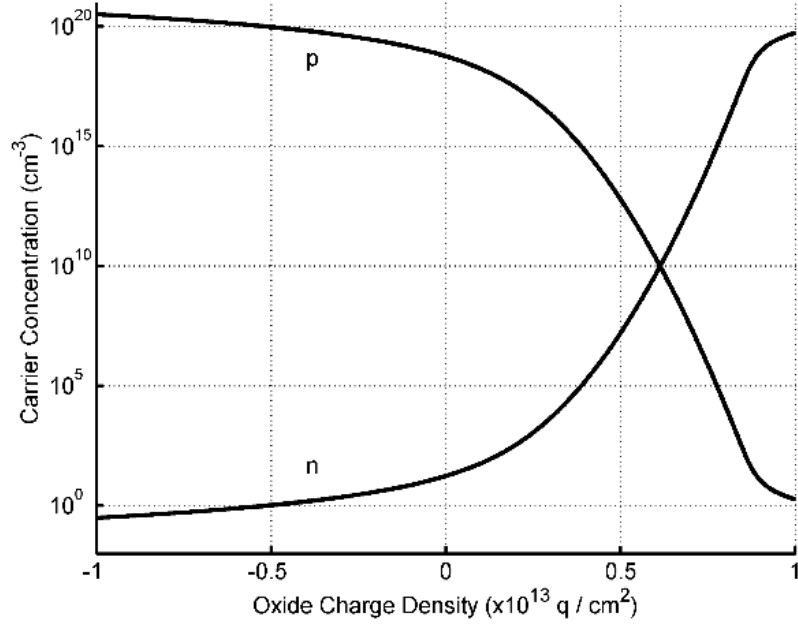


Fig. 67. Majority carrier concentration at the surface of p-type and n-type silicon as a function of the oxide charge density.

Numerically solving equation (80), we can find relationship between potential, ψ and distance, x for given surface potential ψ_s , which in turn depends on total charge in the oxide, Q_{ox} . The oxide charge will attract an equal but opposite charge in the silicon. The total charge in Si is given by:

$$Q_{Si}(\psi) = \epsilon_{Si} \frac{d\psi_s}{dx} = -Q_{ox} \quad (81)$$

where $\frac{d\psi_s}{dx}$ is the potential gradient at the surface (i.e. at $x = 0$). So, we find $\psi_s(Q_{ox})$

by solving the following expression numerically:

$$Q_{ox} - (2kT p_0 \epsilon_{Si})^{\frac{1}{2}} \left[\left(e^{-\frac{q\psi_s}{kT}} + \frac{q\psi_s}{kT} - 1 \right) + \frac{n_0}{p_0} \left(e^{\frac{q\psi_s}{kT}} - \frac{q\psi_s}{kT} - 1 \right) \right]^{\frac{1}{2}} = 0 \quad (82)$$

The conductivity as a function of distance (from the surface) is given by:

$$\sigma(x) = q\mu_p p(x) + q\mu_n n(x) \quad (83)$$

where mobilities μ_p and μ_n can be calculated using equations (73) and (74) respectively; while $p(x)$ and $n(x)$ is found from equations (77) and (78) respectively. Fig. 67 shows the surface (at $x = 0$) majority carrier concentration profile with respect to oxide charge density for p-type and n-type semiconductor. As expected, the majority carrier concentration at the surface is very high during accumulation and very low during depletion.

The resistance of the resonator base can be calculated by:

$$R = \frac{L_b}{W_b \int_0^{H_b} \sigma(x) dx} \quad (84)$$

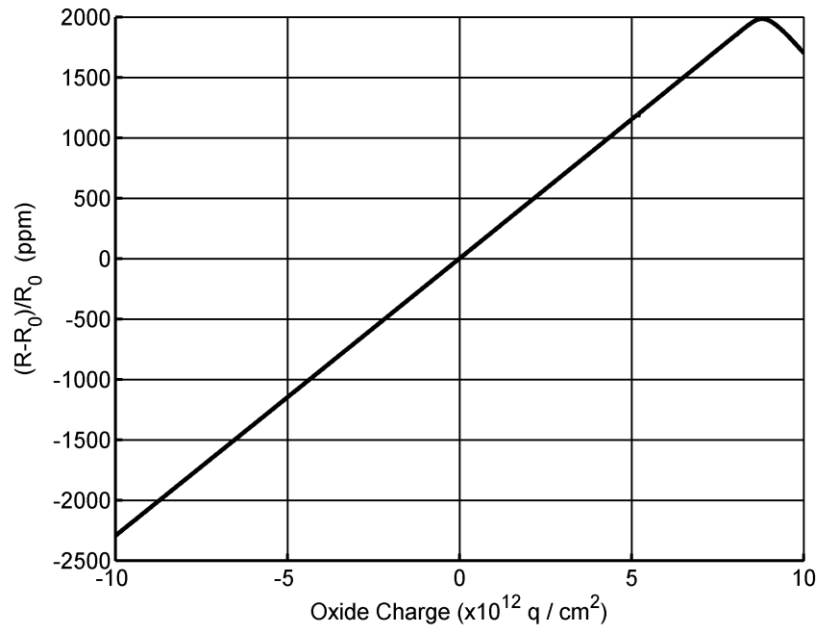


Fig 68. Parts per million (ppm) change in resistance with respect to oxide charge density.

where L_b , W_b and H_b are the length, width and height of the resonator base respectively. It was assumed--to simplify the resistance measurement--that the UV radiation created charges at the top and bottom surfaces of the resonator base but not on the sides. If charges on the side are included the change in resistance will be more. Fig 68 shows the ppm change in resistance of the resonator base as a function of oxide charge density for p-type semiconductor. The resistance goes up as oxide accumulates positive charges since it depletes free holes near the surface in silicon which decreases the effective conductive area of the base. But as the positive charge exceeds certain limit, it causes creation of an inversion channel (of electron) near Si surface--like MOSFET's conduction channel--that lowers the resistance. On the other hand, if the oxide gets negatively charged, it drives the silicon surface towards accumulation so lots of excess holes accumulates at the surface that lowers the resistance of the resonator base.

6.1.5. Resonance frequency modulation by excess free carriers

In the previous section, we discussed about charging of native oxide due to radiation that creates mirror charges in the silicon. We will devote this section to investigate the role of excess carriers in modifying the elastic constant of silicon. Several researchers including Keyes [35], Csavinszky et al. [40], Fjeldly et al. [110], Kim et al. [111] reported that changing the doping concentration changes the elastic constant of semiconductors. Since the observed change in elastic constant was reported to come from the change in electron's free energy [35], we can expect that if electron/hole concentration is increased by other means, e.g. by radiation, that will also have similar effect on elastic constant. The relationship between shear elastic constant and electron concentration is as follows:

$$c'_{44} = c_{44} - \frac{4}{3} \left(\frac{4\pi}{3} \right)^{2/3} \left(\frac{m_n \Xi_u^2 n^{1/3}}{h^2} \right) \quad (85)$$

where c_{44} is the shear elastic constant of undoped silicon (79.51 GPa), h is the Planck's constant, n is the electron concentration, Ξ_u is the deformation potential, and m_n is the effective mass of electron. There are a number of values reported for deformation potential in literature, for example, 9.29 eV in [112] and 8.6 eV in [113], we used a value of 5.5eV that was found by fitting experimental data obtained from [114].

The relationship between shear elastic constant and hole concentration is given by [40],

$$c'_{44} = c_{44} - \frac{1}{5} \left(\frac{8\pi}{3} \right)^{2/3} \frac{\Xi_s^2}{h^2} (m_{hh} p_{hh}^{1/3} + m_{lh} p_{lh}^{1/3}) \quad (86)$$

where Ξ_s is the shear deformation potential; p_{hh} and p_{lh} represents hole concentrations in heavy hole and light hole bands, respectively. The effective masses of holes residing at heavy hole band and light hole band are represented by m_{hh} and m_{lh} , respectively. Researchers used different values of shear deformation potentials, for example, it ranged from 5.8eV to 11.8eV in [40]. According to our calculation using experimental elastic constant data from [114], the value of Ξ_s ranges from 8.1eV to 13.8eV. We used 13.8eV in our calculation because it was found to fit best for highly doped silicon. From equation (85) and (86), we observe that increase in carrier concentration reduces elastic constant, and vice versa. Fig. 69 shows normalized change in shear elastic constant, c_{44} as a function of distance from the surface of a p-type Si for different oxide charge densities that drive the silicon surface to accumulation, depletion or strong inversion. In case of accumulation, c_{44} decreases near the surface due to the presence of excess holes attracted by the negative charge in the oxide. In case of depletion, the positive charge in

the oxide repels the holes in Si to create a depletion region that extends from the surface into the bulk. So, the elastic constant near the surface increases to undoped c_{44} value. But if the positive charge in oxide is too high, silicon surface goes into strong inversion that causes electron concentration to increase near the surface. The extra electrons reduce elastic constant near the surface, but elastic constant remains high in the adjacent depletion region.

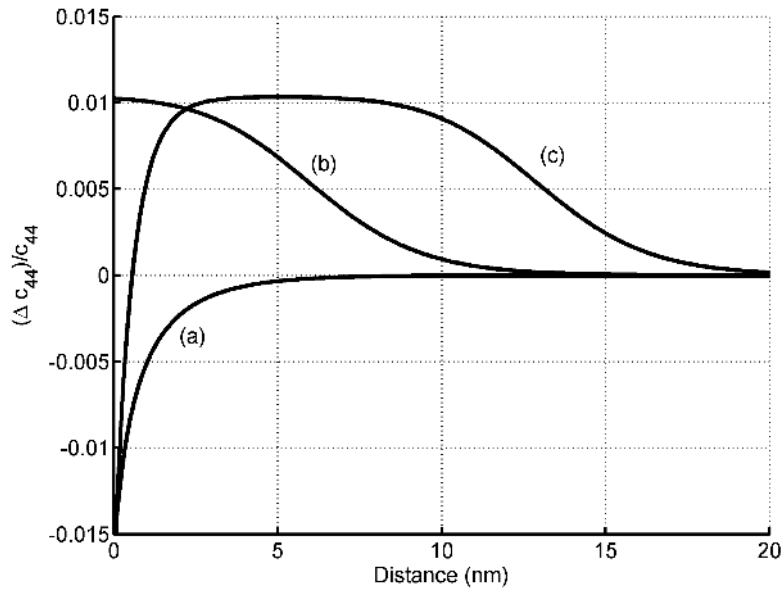


Fig. 69. Normalized change in c_{44} with respect to distance from the surface plotted for different oxide charge densities that causes (a) accumulation ($\rho_{ox} = -0.5 \times 10^{13} \text{ cm}^{-2}$), (b) depletion ($\rho_{ox} = 0.5 \times 10^{13} \text{ cm}^{-2}$), or (c) strong inversion ($\rho_{ox} = 1 \times 10^{13} \text{ cm}^{-2}$) at the silicon surface for p-type silicon with doping concentration of $5.8 \times 10^{18} \text{ cm}^{-3}$.

We can calculate the resonance of a simple cantilever beam using the following equation.

$$\omega = \frac{\xi^2}{L^2} \sqrt{\frac{EI}{\rho WH}} \quad (87)$$

where L , is the length of the cantilever, W and H are the cantilever width and height, respectively, ξ is the mode constant (for first mode, $\xi = 1.875104$), ρ is silicon density, E is the Young's modulus.

Since our freestanding cantilever lies in the $[110]$ direction, Young's modulus, E and c_{44} can be related by the following expression:

$$E = 4 \frac{c_{11}^2 + c_{11}c_{12} - 2c_{12}^2}{2c_{11}c_{44} + c_{11}^2 + c_{11}c_{12} - 2c_{12}^2} c_{44} \quad (88)$$

where c_{11} and c_{12} are other non-zero elastic constants of silicon. For simplicity, we will assume that c_{11} and c_{12} does not change with doping and Young's modulus is proportional to c_{44} . So, $\frac{E'}{E} \approx \frac{c_{44}'}{c_{44}}$ where E' and c_{44}' are the modified values of Young's modulus and elastic constant, respectively.

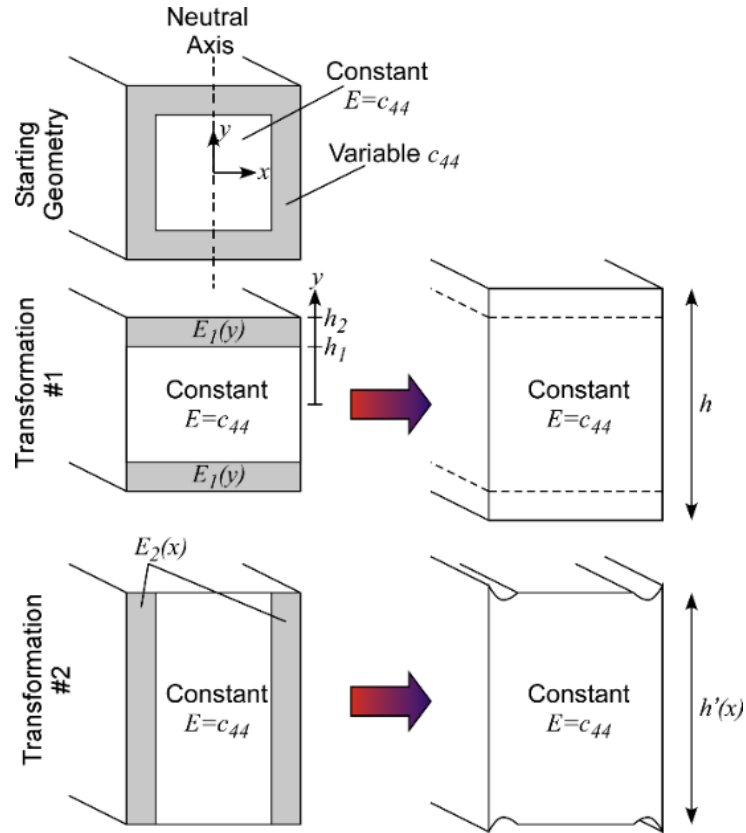


Fig. 70. Beam dimension transformation to get a uniform and constant effective Young's modulus.

Since trapped charge in the native oxide modulates the carrier concentration near the silicon surface, the Young's modulus will change from its bulk value in that region. We can still use equation (87) to calculate the resonance frequency if we can find an equivalent Young's modulus that remains constant throughout the beam. We can do that by transforming the dimensions [115] of the beam as illustrated in Fig. 70. Since the Young's modulus changes on all four sides of the beam cross section, we did two geometry transformation as shown in the figure. The first transformation found the new height h to account for the Young's modulus variation, $E_1(y)$ at the top and bottom surfaces. If $2h_1$ is the height before transformation and h_2 is the thickness of the volume affected by the Young's modulus change, the transformed height is given by,

$$h = 2h_1 + 2 \int_{h_1}^{h_2} \frac{E_1(y)}{E} dy \quad (89)$$

This new height, h is used in the second transformation that accounts for the Young's modulus variation, $E_2(x)$ at the left and right sides of the beam. The heights obtained from the two transformations are related by the following equation,

$$h'(x) = \frac{E_2(x)}{E} h \quad (90)$$

We can calculate the moment of inertia of the transformed geometry using the general formula which in this case is given by,

$$I_y = \int_{-\frac{w}{2}}^{\frac{w}{2}} \int_{-\frac{h'(x)}{2}}^{\frac{h'(x)}{2}} x^2 dx dy = \frac{2h}{E} \int_0^{\frac{w}{2}} x^2 E_2(x) dx \quad (91)$$

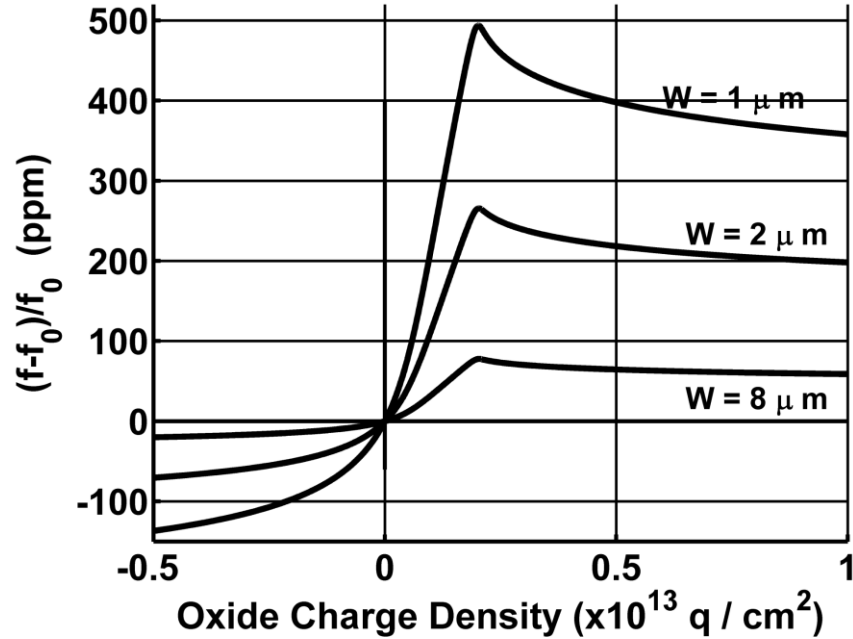


Fig. 71. Dimensional dependence study of the UV radiation damage with heavily doped ($5.8 \times 10^{18} \text{cm}^{-3}$) p-type Si resonators. (a) Ppm change in resonance frequency with respect to oxide charge density for three different widths ($1 \mu\text{m}$, $2 \mu\text{m}$ and $8 \mu\text{m}$).

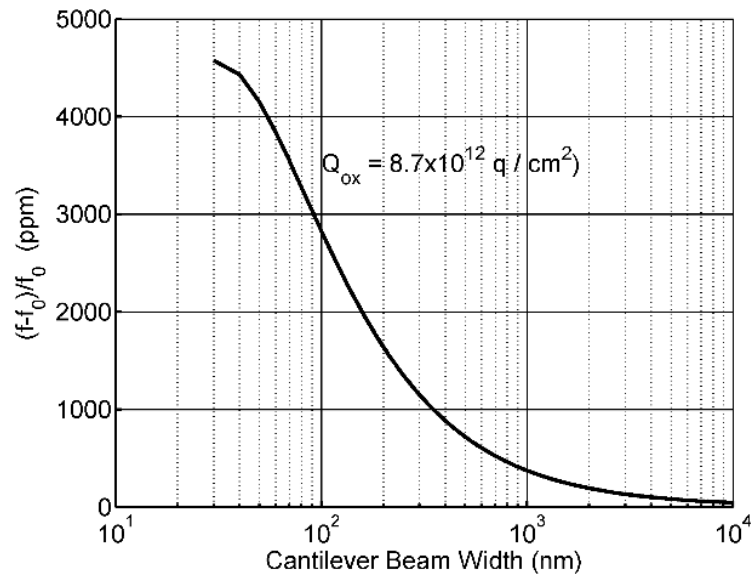


Fig. 72. Normalized resonance frequency shift vs. beam width for p-type resonators with doping concentration of $5.8 \times 10^{18} \text{ cm}^{-3}$ and a fixed oxide charge density of $8.71 \times 10^{12} \text{ cm}^{-2}$.

Equation (91) can be solved numerically and it will allow us to calculate resonance frequency using a uniform Young's modulus across the whole geometry. We calculated the resonance frequency change as a function of the oxide charge density at the beam surface as shown in Fig. 71. The plot shows the calculated resonant frequency change for $1 \mu\text{m}$, $2 \mu\text{m}$ and $8 \mu\text{m}$ wide resonators. Similar to the experimental result, smaller width devices show a larger shift in resonance frequency for the same amount of oxide charging. Since we do not know the starting and ending charge state of the native oxide, we cannot exactly calculate the expected change in resonance frequency but from the plot we see that it is possible to explain the experimentally observed ppm change in resonance frequency using the model. The surface charge model successfully shows the trend in resonance frequency change due to UV irradiation for different width devices. If we shrink the beam width more, the UV radiation effect sharply increases as shown in Fig. 72. It shows that

UV radiation might have more profound effect as the MEMS devices are scaled down, e.g. greater than 3000ppm change is expected for devices with less than 100nm beam width according to this calculation [13].

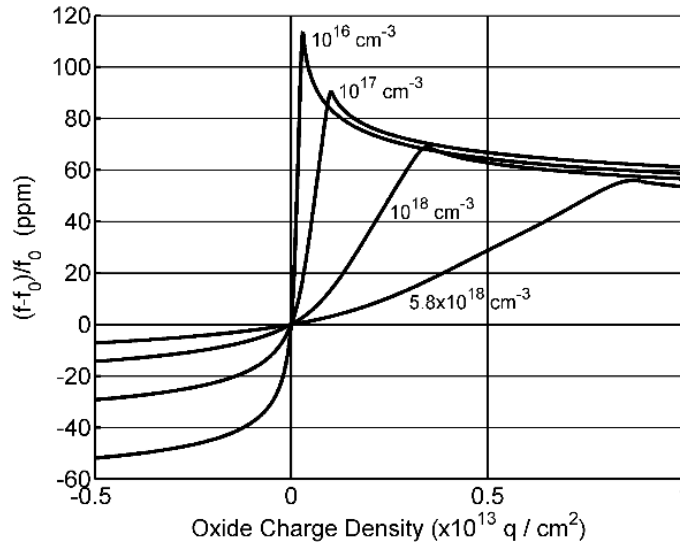


Fig. 73. Normalized resonance frequency shift as a function of oxide charge density for p-type Si resonators of different doping concentration.

Fig. 73 shows the doping level dependence of the UV radiation. As shown in the figure, it is expected that the devices with lower doping concentration will show larger shift in resonance since it requires larger volume to redistribute mirror charges in silicon with lower doping, for the same amount of surface charging. But we did not see any conclusive result to support this prediction.

6.2 Model of X-ray radiation damage

In the above section, we calculated the expected change in resonance frequency for change in Young's modulus only near the surface of the beam using geometry

transformation. For a uniform change in Young's modulus, the resonance frequency change can be calculated using the following simple formula,

$$\Delta f = 10^6 \times \frac{\xi^2}{2\pi l^2} \sqrt{\frac{I}{\rho_{Si}wh}} (\sqrt{E'} - \sqrt{E}) \quad (92)$$

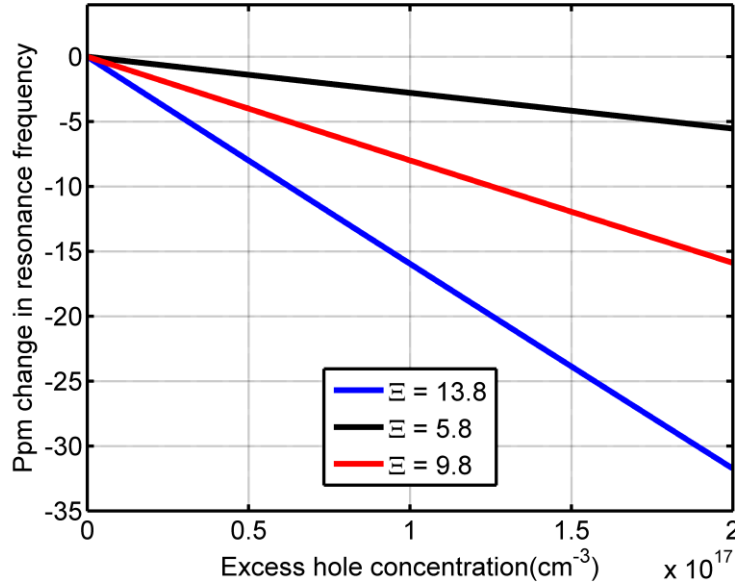


Fig. 74. Ppm change in resonance frequency as a function of excess hole concentration for several deformation potential values that span the typical range of values found in literature. Deformation potential affects the slope of the plot and larger deformation potential causes steeper slope i.e. for a given change in carrier concentration we get larger shift in frequency.

where E' is the modified Young's modulus due to radiation, ξ^2 is a mode constant (for first mode, $\xi = 1.875104$), ρ_{Si} is the density of Si, I is the moment of inertia and, l , w and h are length, width and height of the center cantilever respectively. The ppm change in resonance frequency as a function of excess hole concentration is plotted in Fig. 74 for three different deformation potentials. It shows that the expected shift in resonance frequency for a certain change in carrier concentration varies widely with different values of deformation potential. So, we cannot predict shift in resonance frequency exactly

without knowing correct value of deformation potential. This is one of the reasons behind explaining radiation mechanism in a qualitative manner rather than exact quantitative analysis.

Carrier concentration changes through two different mechanisms for X-ray and UV radiation as reported in earlier publications [1, 13]. The effect of carrier concentration increase on resistivity is also different for X-ray and UV. We found that resistance decreases during UV radiation [13] but increases during X-ray radiation. Resistance decreases during UV radiation since carrier concentration is increased and carrier mobility does not get affected significantly due to UV radiation. X-ray radiation causes changes in both carrier mobility and carrier concentration as discussed below.

A. Resistance change during X-ray radiation

X-ray Radiation creates extra carrier by both electron-hole pair generation and hydrogen-boron dissociation. After Hydrogen-dopant dissociation hydrogen and dopant ion act as scattering centers. The dominant hydrogen state in p-type silicon is reported to be H^+ [116]. The carrier mobility get decreases due to increased impurity scattering. The net effect of increased carrier concentration and decreased mobility determines the direction of resistance change.

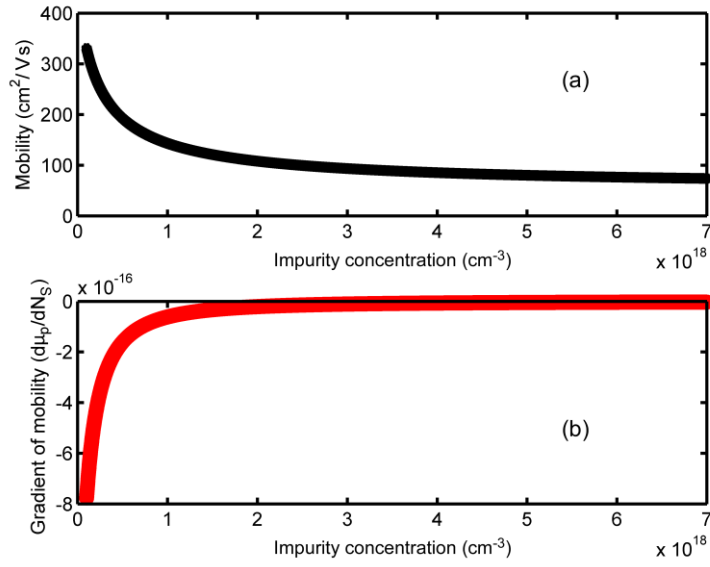


Fig. 75. (a) Hole mobility as a function of impurity concentration (N_s) and, (b) gradient of mobility ($d\mu_p/dN_s$) as a function of impurity concentration

Arora model [17] can be used to find the effect of increased scattering center on carrier mobility. That model gives us the mobility as a function of impurity concentration as shown in equation (93) and plotted in Fig. 75(a).

$$\mu_p = \mu_p^{min} + \frac{\mu_0}{1 + \left(\frac{N_s}{N_{ref}}\right)^\gamma} \quad (93)$$

where μ_p^{min} , μ_0 and N_{ref} are empirically determined constant [17]. Both charged boron and hydrogen can be considered as impurity in our case. The gradient of mobility with respect to impurity concentration as a function of impurity concentration is shown in Fig. 75(b). The figure shows that at lower impurity concentration, the gradient is steeper so the amount of change in mobility for a given change in scattering center concentration depends on the initial doping concentration and hydrogen ion concentration. We will assume at the beginning of radiation there were no hydrogen ion and the impurity concentration were

equal to initially active boron dopant concentration. The resistivity will depend on two competing factors—increase in carrier concentration and decrease in mobility—and can be calculated using the following equation:

$$\rho = \frac{1}{q \times \mu_p \times (p + \Delta p)} \quad (94)$$

where, p is the hole concentration before irradiation which is approximately equals to doping concentration (N_a), Δp is excess hole concentration due to X-ray and, μ_p is hole mobility that can be calculated using (93).

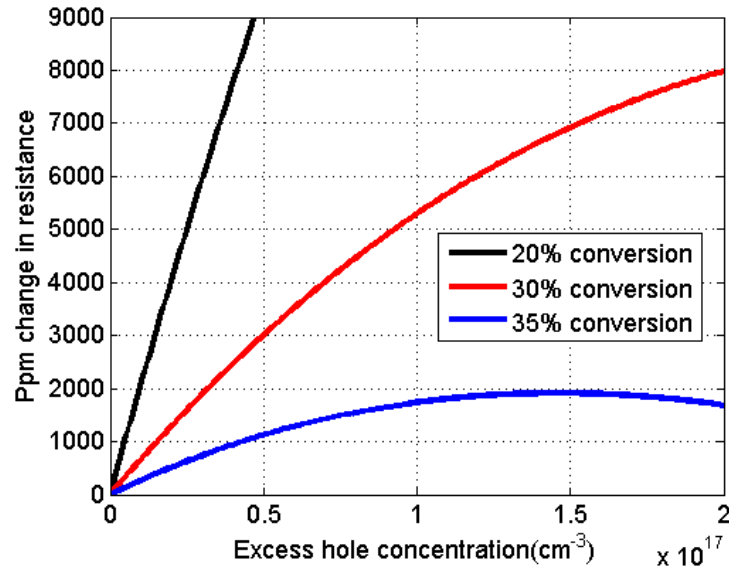


Fig. 76. Ppm change in resistance with respect to excess hole concentration for different percentage of trapping of positively charged hydrogen at the surface.

When a positively charged hydrogen get trapped at the interface or native oxide, we gain a hole from the depassivated boron that is left behind by the hydrogen. The net effect of mobility change and carrier concentration change determines the base resistance. And it relies on what percentage of generated positively charged hydrogen get trapped at

any given time. We assume that during radiation, the system reaches an equilibrium when hydrogen-boron dissociation rate and hydrogen trapping rate are equal. So, in equilibrium, a fixed percentage of newly generated positively charged hydrogen ion get trapped for a given dose rate. Fig. 76 shows expected ppm change in resistance as a function of excess hole concentration for different percentages of hydrogen trapping. It shows that when hydrogen trapping is less, resistance increase is more but as the carrier concentration increases above certain value resistance will start to decrease. If we consider the extreme case where all the hydrogens are getting trapped, the resistance will monotonically decrease due to increased carrier. So, the observed resistance increase during X-ray exposure supports our model of hydrogen and boron scattering center formation.

B. Dimensional dependence of X-ray radiation damage

The positively charged hydrogen activates the surface states at the Si-SiO₂ interface [117]. Positively charged hydrogen and neutral hydrogen molecule both has higher diffusion barrier in Si than SiO₂ [118]. So unreacted neutral and charged hydrogen diffuse into the oxide. The following reactions occur at the bulk during X-ray radiation:



The following reaction occur at the interface [119]:



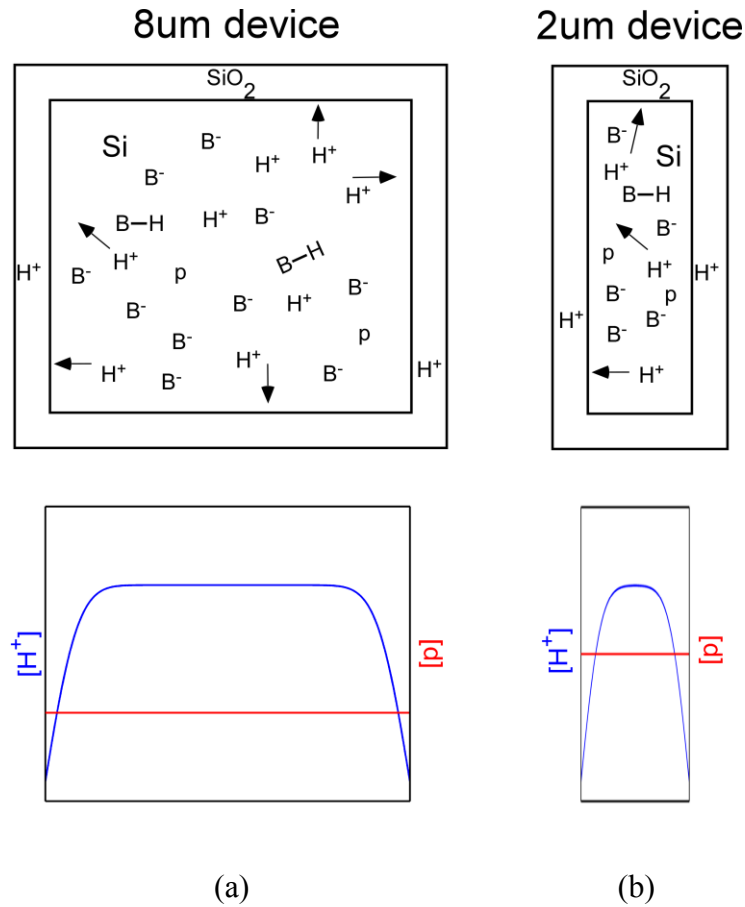


Fig. 77. Schematic illustration that shows the concept of hydrogen transport in Si and subsequent trapping in native oxide for (a) $8\mu\text{m}$ and (b) $2\mu\text{m}$ wide resonating cantilever devices. The hydrogen gets trapped at the same rate per unit surface area for both devices but the change in free hydrogen concentration per unit volume is different due to different surface-to-volume ratio.

We propose that as the hydrogen ion reacts with surface states or get trapped in the native oxide, a concentration gradient of positively charged hydrogen forms near the surface shown Fig. 8 where a cross section of the resonator cantilever is illustrated. This gradient causes extra hydrogen ions to diffuse towards the interface. As the hydrogen separates from the boron and hydrogen get trapped at the interface/oxide boron gets activated. So free carrier concentration increases. Since diffusion of hydrogen towards the interface takes some finite amount of time, there is a lag between carrier generation and

hydrogen-boron dissociation. So, impurity scattering due to excess ions dominate the resistance change and causes resistance to increase. On the other hand, resonance frequency does not get affected by charged species concentration and decreases due to increased excess carriers only.

From Fig. 8, we can see that the concentration of holes is higher for narrower (smaller width) devices because it loses larger percentage of its total hydrogen content through wider surface area. The generated hole spread quickly over the whole volume of silicon due to high mobility, so the concentration of hole increases uniformly. The width of the center cantilever was changed to change the surface-to-volume ratio. So, higher surface-to-volume devices will have larger changes in resonance frequency for the same duration of radiation exposure due to larger change in excess hole concentration. This explanation is the basis of the dimensional dependence for X-ray radiation. We can calculate the rate at which hydrogen is getting trapped by calculating the excess carrier that need to be generated to cause the observed resonance frequency shift using the equations (86), (88) and (92). We assumed that hydrogen will get trapped at a constant rate, r_T for a given dose rate irrespective of the beam width dimension. We calculated the change in excess hole concentration, Δp required to get the observed change in resonance frequency after 1Mrad X-ray radiation for our 8 μm wide cantilever resonator. We propose that the number of hydrogens trapped, H_T at the surface is the same as the change in excess hole concentration. We calculated the expected number of trapped hydrogens for the same dose rate for different beam width resonators. That gives us the change in excess carrier concentration for different beam width devices. Mathematically,

$$\Delta p = r_T \times Rsv \times t \quad (99)$$

where t is the duration of radiation and Rsv is the surface-to-volume ratio given by,

$$Rsv = \frac{2(lw + wh + lh)}{lwh} \quad (100)$$

Now, since for a given dose rate t and r_T are constant, $\Delta p \propto Rsv$.

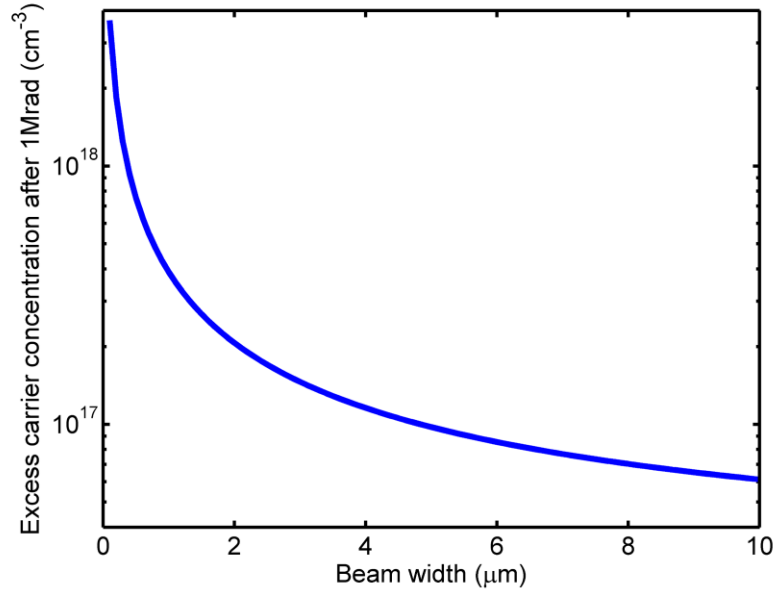


Fig. 78. Excess carrier concentration as a function of beam width that shows excess free carrier decreases as the width increases.

As shown in Fig. 78, the excess carrier concentration is higher for devices with smaller beam width i.e. for devices with higher surface-to-volume ratio. Since we now know the excess carrier concentration, we can calculate expected resonance frequency shift for different beam widths.

Fig. 79 shows the ppm change in resonance frequency as a function of beam width. The experimentally observed resonance frequency shift is overlaid on the same plot.

The experimental results agree with the model with reasonable accuracy.

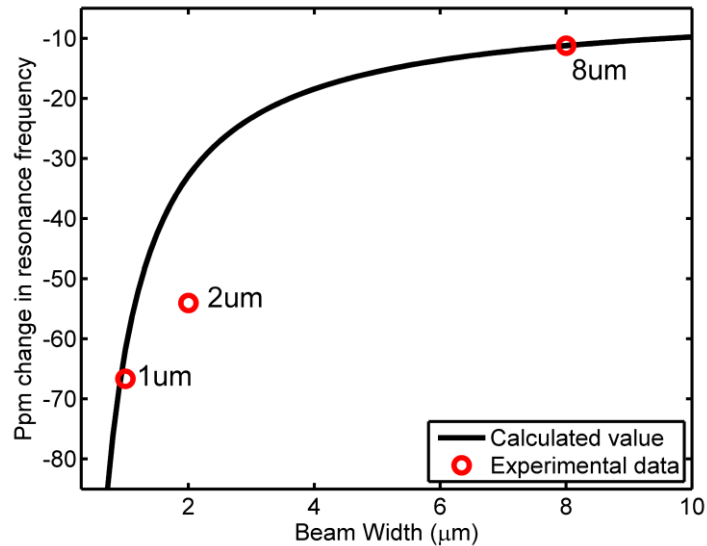


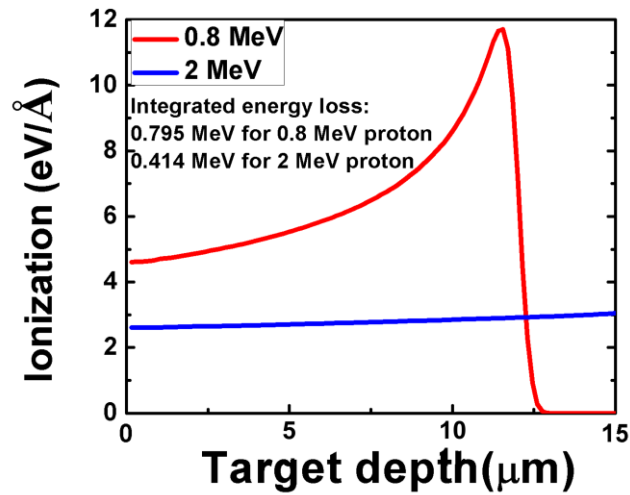
Fig. 79. Comparison of experimental and theoretically predicted values of ppm change in resonance frequency for different beam widths. Our model's prediction closely matches with the experimental values.

After radiation is turned off the hydrogen diffusion towards the surface continues for certain amount of time due to the remaining free positively charged hydrogen concentration. Also, the surface field due to native oxide charging get reduced helping the motion of hydrogen towards the interface. Hydrogen starts to passivate boron that drops free hydrogen concentration so after certain time the diffusion stops. The resistance starts to decrease, and resonance frequency starts to increase. The x-ray ionization damage is reversible and after annealing the resonance frequency and resistance recovers to their original values. So, observed complete recovery of radiated devices supports our hypothesis of hydrogen diffusion-based damage mechanism.

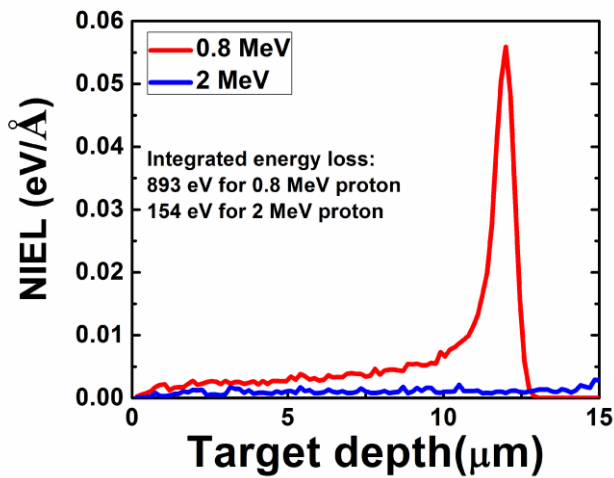
6.3 Model of proton radiation damage

Proton causes both ionization and displacement damage. The ionization increases carrier concentration in a similar fashion as X-ray whereas displacement damage reduces carrier concentration by creating defects and trap centers. So, the net change in carrier concentration is determined by the competing effect of ionization damage and displacement damage. We radiated highly doped ($5.8 \times 10^{18} \text{ cm}^{-3}$) p-type $8\mu\text{m}$ wide resonators with 0.8MeV and 2MeV proton—at flux rates of $4 \times 10^8 \text{ ions/cm}^2\cdot\text{s}$ and $10^{10} \text{ ions/cm}^2\cdot\text{s}$ respectively. The resonance frequency decreased for high energy proton radiation while increased for low energy proton radiation. The energy dependence of the proton radiation damage is observed because proton with 2MeV energy easily passes through the silicon whereas proton with 0.8MeV energy loses all its energy and stops inside silicon beam. As a result, the magnitude of ionization damage and displacement damage caused by these two types of proton radiation differs significantly. For the high energy proton radiation, ionization effect dominates at lower fluences causing resonant frequency to decrease like X-ray radiation, but as the radiation continues (i.e. at higher fluences) the displacement damage becomes more significant which tends to offset further decrease in resonance frequency. During annealing, the ionization damage recovers quickly but the displacement damage does not recover resulting in a net positive shift in resonance frequency. On the other hand, for low energy proton radiation, the displacement damage is always dominant as the protons impinge on the silicon and forms a lot of defect cluster at a much higher rate than high energy proton radiation. So, the ionization damage is less pronounced. Furthermore, the defects reduce the lifetime of the carrier and hinders H^+ transport across silicon that further reduces the ionization damage. During annealing, again

the ionization damage recovers leaving the displacement damage mostly in place. As a result, a larger permanent net positive shift in resonance is observed for low energy proton radiation. Fig. 80 shows the result of SRIM (The Stopping and Range of Ions in Matter) simulation where ionization and non-ionization energy loss as a function of silicon depth from the radiated surface. This simulation validates our theory of larger displacement damage for low energy proton radiation and it also shows the peak where most of the low energy proton stops inside our 15 μm thick silicon resonator.



(a)



(b)

Fig. 80. Simulation results from SRIM analysis. (a) Ionization energy as a function of target depth from the exposed Si surface for 0.8MeV proton radiation and (b) Non-ionizing energy loss (NIEL) as a function of target depth from the Si surface for 2MeV proton radiation.

From the experiment, the resistance is found to increase during both types of proton radiation which recovers only a little during annealing. This permanent resistance increase

can be attributed to the reduced carrier mobility as a result of increase in crystal defects caused by the displacement damage that now acts as a scattering center.

6.4 Conclusion

X-ray and UV radiation damage mechanisms are different, but both are dominated by the surface effect. Hydrogen-boron complex dissociates under X-ray exposure and hydrogen get trapped at the surface defect or native oxide that changes the carrier concentration and carrier mobility in the silicon. The resistance and resonance frequency change are found to be inversely related due to the interplay of carrier concentration and mobility change. Post-radiation damage and annealing characteristics indicate a diffusion-based mechanism for X-ray radiation damage that reinforces the credibility of our model. The hydrogen diffusion model also explained dimensional dependence and the theoretical calculation matched closely with the experimental observation. UV radiation damage also showed dimensional dependence and we showed that our model successfully predicted the trend of increased radiation damage for higher surface-to-volume devices. Proton radiation causes both ionization and displacement damage where the dominant mechanism depends on the energy of the proton and the dimension of the sample. Our models show that radiation effect increases on MEMS devices as the device size is reduced, so we should re-evaluate radiation effect when scaling MEMS devices for space application, especially towards nanoscale.

CHAPTER VII

CONCLUSION

We investigated the radiation damage mechanism in MEMS devices with three different types of radiation: UV, X-ray and proton. Ionization damage is found to be the principle damage mechanism for UV and X-ray radiation, although the underlying physical mechanism of ionization damage is different. During UV radiation, native oxide charging due to charge separation at the Si-SiO₂ interface plays the dominant role. On the other hand, hydrogen-dopant complex dissociation due to X-ray radiation is the major contributor to the X-ray radiation damage. The surface is found to play a large role in the damage mechanism for both UV and X-ray, and it is supported by the fact that the high surface-to-volume devices show greater damage. We showed that reduction in certain dimension enhances the radiation damage and our proposed models fit the observed dimensional dependence of radiation damage for both X-ray and UV radiation. For x-ray radiation, radiation damage is also found to be dose-rate dependent where low dose-rate radiation caused more damage than high dose-rate radiation. UV and X-ray does not have enough energy to cause displacement damage, so we did not see any permanent damage and all devices eventually recovers after radiation. In contrast, proton radiation caused both ionization and displacement damage where the ratio of ionization and displacement damage depends on the proton energy and device geometry. Finally, we found that UV and

X-ray causes reversible ionization damage while proton causes both reversible ionization damage and irreversible displacement damage.

The novel contributions of this work to the studies of MEMS and radiation effect has been summarized below:

- Designed, optimized and fabricated a novel asymmetric piezoresistor that is about 481 times more sensitive compared to its symmetric counterpart.
- We successfully fabricated high aspect ratio (15:1) silicon cantilever using conventional Bosch DRIE process.
- We are the first group who extended application of Keyes' theory [35] to find the effect of any carrier concentration change—due to any mechanism such as radiation, temperature change and junction bias—on the elastic constant of silicon.
- Theoretically modeled the UV radiation damage mechanism that relates the mechanical property of silicon to the carrier concentration change near the surface. It also successfully predicted the dimensional dependence of the UV radiation damage.
- Dimensional dependence of the X-ray radiation effect has been successfully explained with hydrogen diffusion model. We showed how different species of hydrogen diffusing through silicon may interact with defect states and cause the observed radiation damage.

It was difficult to do exact analytic comparison between theoretical calculation and experimental observations in most cases since some parameters used in our models, such as deformation potential, does not have a well-defined value in literature and the theories

behind some of the models need to be developed further. In some cases, measuring ppm level changes was challenging due to the noise and that contributed to the deviation of experimental and theoretical results.

This work showed the different pathways of radiation damage for different types of radiation and identified the factors/elements that play the major role in the process. For example, amount of exposed surface oxide and hydrogen content plays the largest role in case of UV and X-ray radiation damage, respectively. The surface-to-volume ratio is another big factor that affect the amount of radiation damage. Proton radiation can irreversibly alter the crystal structure of the silicon that causes permanent displacement damage. So, when designing MEMS devices for space application, the abovementioned factors need to be considered carefully. Overall, I believe the results presented in this work will help us to design radiation-hard MEMS devices that will operate reliably in radiation environment.

REFERENCES

- [1] H. Gong, W. Liao, E. X. Zhang, A. L. Sternberg, M. W. McCurdy, J. L. Davidson, *et al.*, "Total-Ionizing-Dose Effects in Piezoresistive Micromachined Cantilevers," *IEEE Transactions on Nuclear Science*, vol. 64, pp. 263-268, 2017.
- [2] H. Gong, W. Liao, E. X. Zhang, A. L. Sternberg, M. W. McCurdy, J. L. Davidson, *et al.*, "Proton-Induced Displacement Damage and Total-Ionizing-Dose Effects on Silicon-Based MEMS Resonators," *IEEE Transactions on Nuclear Science*, vol. 65, pp. 34-38, 2018.
- [3] J. T. Lin, P. D. Shuvra, W. Liao, S. McNamara, K. M. Walsh, C. N. Arutt, *et al.*, "Surface carrier concentration effect on elastic modulus of piezoelectric MEMS silicon cantilevers," in *2017 19th International Conference on Solid-State Sensors, Actuators and Microsystems (TRANSDUCERS)*, 2017, pp. 1175-1178.
- [4] ThorLab. (2018, 05/17/2018). *LED255J - OPTAN® UV LED with Ball Lens, 255 nm, 1 mW (Min), TO-39* Available: <https://www.thorlabs.com/thorproduct.cfm?partnumber=LED255J>
- [5] B. G. Streetman and S. Banerjee, *Solid State Electronic Devices*: Pearson Prentice Hall, 2006.
- [6] M. UofL. (2018, 05/16/2018). *MNTC Cleanroom SOP*. Available: <https://louisville.edu/micronano/files/documents/standard-operating-procedures/SUSSAlignerSOP.pdf>

- [7] M. UofL. (2018, 05/16/2018). *MNTC cleanroom SOP*. Available: <http://louisville.edu/micronano/files/documents/standard-operating-procedures/PVD75SOP.pdf>
- [8] E. Optics. (2018, 05/17/2018). *Calcium Fluoride (CaF₂) Windows* Available: <https://www.edmundoptics.com/optics/windows-diffusers/ultraviolet-uv-infrared-ir-windows/Calcium-Fluoride-CaFsub2sub-Windows/>
- [9] J. Dziewior and W. Schmid, "Auger coefficients for highly doped and highly excited silicon," *Applied Physics Letters*, vol. 31, pp. 346-348, 1977.
- [10] S. Pranoy Deb, M. Shamus, L. Ji-Tzuoh, A. Bruce, W. Kevin, and D. Jim, "Axial asymmetry for improved sensitivity in MEMS piezoresistors," *Journal of Micromechanics and Microengineering*, vol. 26, p. 095014, 2016.
- [11] J. T. Borenstein, J. W. Corbett, and S. J. Pearton, "Kinetic model for hydrogen reactions in boron-doped silicon," *Journal of Applied Physics*, vol. 73, pp. 2751-2754, 1993.
- [12] P. J. H. Denteneer, C. G. Van De Walle, and S. T. Pantelides, "MICROSCOPIC STRUCTURE OF THE HYDROGEN-BORON COMPLEX IN CRYSTALLINE SILICON," *PHYSICAL REVIEW B*, vol. 39, pp. 10809-10824, 1989.
- [13] J. T. Lin, P. D. Shuvra, S. McNamara, H. Gong, W. Liao, J. L. Davidson, *et al.*, "Near-Surface Electronic Contribution to Semiconductor Elasticity," *Physical Review Applied*, vol. 8, p. 034013, 09/18/ 2017.
- [14] V. V. Voronkov and R. Falster, "Modelling plasma-induced hydrogen profiles in boron-doped and near-intrinsic silicon," *physica status solidi (a)*, vol. 214, pp. 1700287-n/a, 2017.

- [15] J. Cazaux, "A physical approach to the radiation damage mechanisms induced by X-rays in X-ray microscopy and related techniques," *Journal of Microscopy*, vol. 188, pp. 106-124, 1997.
- [16] C. N. Arutt, W. Liao, H. Gong, P. D. Shuvra, J. T. Lin, M. L. Alles, *et al.*, "Dose-Rate Effects on the Total-Ionizing-Dose Response of Piezoresistive Micromachined Cantilevers," *IEEE Transactions on Nuclear Science*, vol. 65, pp. 58-63, 2018.
- [17] N. D. Arora, J. R. Hauser, and D. J. Roulston, "Electron and hole mobilities in silicon as a function of concentration and temperature," *IEEE Transactions on Electron Devices*, vol. 29, pp. 292-295, 1982.
- [18] H. Shea, "MEMS for pico- to micro-satellites."
- [19] G. W. Gray, "COSMIC RAYS," *Scientific American*, vol. 180, pp. 28-39, 1949.
- [20] H. R. Shea, *MEMS for pico- to micro-satellites*, 2009.
- [21] P. Gallois, "Life expectancy of communication satellites," *Electronics and Power*, vol. 33, pp. 547-550, 1987.
- [22] D. picosats. Available: <https://www.darpa.mil/about-us/timeline/picosat>
- [23] A. Brown and Y. Lu, "Performance Test Results of an Integrated GPS/MEMS Inertial Navigation Package," *Proceedings of the 17th International Technical Meeting of the Satellite Division of The Institute of Navigation (ION GNSS 2004)*, Long Beach, CA, pp. 825-832, September 2004 2004.
- [24] J. T. M. v. Beek and R. Puers, "A review of MEMS oscillators for frequency reference and timing applications," *Journal of Micromechanics and Microengineering*, vol. 22, p. 013001, 2012.

- [25] N. A. Charles, L. A. Michael, L. Wenjun, G. Huiqi, L. D. Jim, D. S. Ronald, *et al.*, "The study of radiation effects in emerging micro and nano electro mechanical systems (M and NEMs)," *Semiconductor Science and Technology*, vol. 32, p. 013005, 2017.
- [26] Wikipedia. Available: https://en.wikipedia.org/wiki/Chernobyl_disaster
- [27] Wikipedia.
- [28] H. R. Shea, "Effects of radiation on MEMS," 2011, pp. 79280E-79280E-13.
- [29] H. R. Shea, "Radiation sensitivity of microelectromechanical system devices," *Journal of Micro/Nanolithography, MEMS, and MOEMS*, vol. 8, pp. 031303-031303-11, 2009.
- [30] A. Tazzoli, G. Cellere, E. Autizi, V. Peretti, A. Paccagnella, and G. Meneghesso, "Radiation Sensitivity of Ohmic RF-MEMS Switches for Spatial Applications," in *2009 IEEE 22nd International Conference on Micro Electro Mechanical Systems*, 2009, pp. 634-637.
- [31] D. G. Marinaro, P. McMahon, and A. Wilson, "Proton Radiation Effects on MEMS Silicon Strain Gauges," *IEEE Transactions on Nuclear Science*, vol. 55, pp. 1714-1718, 2008.
- [32] K. E. Holbert, J. A. Nessel, S. S. McCready, A. S. Heger, and T. H. Harlow, "Response of piezoresistive MEMS accelerometers and pressure transducers to high gamma dose," *IEEE Transactions on Nuclear Science*, vol. 50, pp. 1852-1859, 2003.

- [33] S. S. McCready, T. H. Harlow, A. S. Heger, and K. E. Holbert, "Piezoresistive micromechanical transducer operation in a pulsed neutron and gamma ray environment," in *IEEE Radiation Effects Data Workshop*, 2002, pp. 181-186.
- [34] S. Zhu, Y. Huang, J. Wang, A. Li, S. Shen, and M. Bao, "Total dose radiation effects of pressure sensors fabricated on uni-bond-SOI materials," *Nuclear Science and Techniques*, vol. 12, pp. 209-214, 2001.
- [35] R. W. Keyes, "The Electronic Contribution to the Elastic Properties of Germanium," *IBM Journal of Research and Development*, vol. 5, pp. 266-278, 1961.
- [36] L. P. Schanwald, J. R. Schwank, J. J. Sniegowski, D. S. Walsh, N. F. Smith, K. A. Peterson, *et al.*, "Radiation effects on surface micromachined comb drives and microengines," *IEEE Transactions on Nuclear Science*, vol. 45, pp. 2789-2798, 1998.
- [37] S. S. McClure, L. D. Edmonds, R. Mihailovich, A. H. Johnston, P. Alonzo, J. DeNatale, *et al.*, "Radiation effects in micro-electromechanical systems (MEMS): RF relays," *IEEE Transactions on Nuclear Science*, vol. 49, pp. 3197-3202, 2002.
- [38] L. D. Edmonds, G. M. Swift, and C. I. Lee, "Radiation response of a MEMS accelerometer: an electrostatic force," *IEEE Transactions on Nuclear Science*, vol. 45, pp. 2779-2788, 1998.
- [39] T. F. Miyahira, H. N. Becker, S. S. McClure, L. D. Edmonds, A. H. Johnston, and Y. Hishinuma, "Total dose degradation of MEMS optical mirrors," *IEEE Transactions on Nuclear Science*, vol. 50, pp. 1860-1866, 2003.

- [40] P. Csavinszky and N. G. Einspruch, "Effect of Doping on the Elastic Constants of Silicon," *Physical Review*, vol. 132, pp. 2434-2440, 12/15/ 1963.
- [41] S. Buchner, D. A. Rapchun, H. Moseley, S. E. Meyer, T. Oldham, K. Ray, *et al.*, "Response of a MEMS Microshutter Operating at 60 K to Ionizing Radiation," *IEEE Transactions on Nuclear Science*, vol. 54, pp. 2463-2467, 2007.
- [42] S. R. Messenger, E. A. Burke, G. P. Summers, M. A. Xapsos, R. J. Walters, E. M. Jackson, *et al.*, "Nonionizing energy loss (NIEL) for heavy ions," *IEEE Transactions on Nuclear Science*, vol. 46, pp. 1595-1602, 1999.
- [43] A. Holmes-Siedle and L. Adams, *Handbook of radiation effects*: Oxford University Press, 1993.
- [44] E. A. Burke, "Energy Dependence of Proton-Induced Displacement Damage in Silicon," *IEEE Transactions on Nuclear Science*, vol. 33, pp. 1276-1281, 1986.
- [45] J. Lindhard, V. Nielsen, M. Scharff, and P. V. Thomsen, "INTEGRAL EQUATIONS GOVERNING RADIATION EFFECTS. (NOTES ON ATOMIC COLLISIONS, III)," 1963-01-01 1963.
- [46] P. E. Hodgson, *The Optical Model of Elastic Scattering*: Clarendon Press, 1963.
- [47] *SRIM - The Stopping and Range of Ions in Matter*. Available: <http://www.srim.org/>
- [48] *PHITS - Particle and Heavy Ion Transport Code System*. Available: <https://phits.jaea.go.jp/>
- [49] G. P. Summers, E. A. Burke, P. Shapiro, S. R. Messenger, and R. J. Walters, "Damage correlations in semiconductors exposed to gamma, electron and proton radiations," *IEEE Transactions on Nuclear Science*, vol. 40, pp. 1372-1379, 1993.

- [50] Y. Iwamoto, H. Iwamoto, M. Harada, and K. Niita, "Calculation of displacement cross-sections for structural materials in accelerators using PHITS event generator and its applications to radiation damage," *Journal of Nuclear Science and Technology*, vol. 51, pp. 98-107, 2014/01/02 2014.
- [51] B. E. Anspaugh, "Proton and electron damage coefficients for GaAs/Ge solar cells," in *The Conference Record of the Twenty-Second IEEE Photovoltaic Specialists Conference - 1991*, 1991, pp. 1593-1598 vol.2.
- [52] J. Gomes and H. R. Shea, "Displacement damage effects in silicon MEMS at high proton doses," 2011, pp. 79280G-79280G-10.
- [53] G. C. Messenger, "A summary review of displacement damage from high energy radiation in silicon semiconductors and semiconductor devices," *IEEE Transactions on Nuclear Science*, vol. 39, pp. 468-473, 1992.
- [54] V. G. Theonas, M. Exarchos, G. Konstantinidis, and G. J. Papaioannou, "RF MEMS sensitivity to electromagnetic radiation," *Journal of Physics: Conference Series*, vol. 10, p. 313, 2005.
- [55] Y. Taur and T. H. Ning, *Fundamentals of Modern VLSI Devices*: Cambridge University Press, 2013.
- [56] H. J. Queisser and D. E. Theodorou, "Decay kinetics of persistent photoconductivity in semiconductors," *Physical Review B*, vol. 33, pp. 4027-4033, 03/15/ 1986.
- [57] H. J. Queisser and D. E. Theodorou, "Hall-Effect Analysis of Persistent Photocurrents in InGaAs Layers," *Physical Review Letters*, vol. 43, pp. 401-404, 07/30/ 1979.

- [58] H. J. Queisser and D. E. Theodorou, "Persistent photoconductivity in sulfur-diffused silicon," *Solid State Communications*, vol. 51, pp. 875-877, 1984/09/01/1984.
- [59] E. F. Schubert, A. Fischer, and K. Ploog, "Electron-impurity tunneling in selectively doped n-type $\text{Al}_x\text{Ga}_{1-x}\text{As}/\text{GaAs}$ heterostructures," *Physical Review B*, vol. 31, pp. 7937-7946, 06/15/1985 1985.
- [60] J. I. Pankove, D. E. Carlson, J. E. Berkeyheiser, and R. O. Wance, "Neutralization of Shallow Acceptor Levels in Silicon by Atomic Hydrogen," *Physical Review Letters*, vol. 51, pp. 2224-2225, 12/12/1983.
- [61] J. I. Pankove, P. J. Zanzucchi, C. W. Magee, and G. Lucovsky, "Hydrogen localization near boron in silicon," *Applied Physics Letters*, vol. 46, pp. 421-423, 1985.
- [62] M. Stutzmann, "Hydrogen passivation of boron acceptors in silicon: Raman studies," *Physical Review B*, vol. 35, pp. 5921-5924, 04/15/1987.
- [63] A. Chantre, L. Bouchet, and E. Andre, "On the Hydrogen Content of Commercial Silicon Wafers," *Journal of The Electrochemical Society*, vol. 135, pp. 2867-2869, November 1, 1988 1988.
- [64] L. V. C. Assali and J. R. Leite, "Microscopic Mechanism of Hydrogen Passivation of Acceptor Shallow Levels in Silicon," *Physical Review Letters*, vol. 55, pp. 980-982, 08/26/1985.
- [65] A. A. Bonapasta, A. Lapicciarella, N. Tomassini, and M. Capizzi, "Hydrogen passivation of shallow acceptors in Si : An ab initio approach," *Physical Review B*, vol. 36, pp. 6228-6230, 10/15/1987.

- [66] J. M. Baranowski and J. Tatarkiewicz, "Bonding or antibonding position of hydrogen in silicon," *Physical Review B*, vol. 35, pp. 7450-7453, 05/15/ 1987.
- [67] R. Rizk, P. de Mierry, D. Ballutaud, M. Aucouturier, and D. Mathiot, "Hydrogen diffusion and passivation processes in p- and n-type crystalline silicon," *Physical Review B*, vol. 44, pp. 6141-6151, 09/15/ 1991.
- [68] D. Tripathi, P. C. Srivastava, and S. Chandra, "Hydrogen passivation studies on Pd-n-type-Si diodes," *Physical Review B*, vol. 39, pp. 13420-13425, 06/15/ 1989.
- [69] N. M. Johnson and C. Herring, "Diffusion of negatively charged hydrogen in silicon," *Physical Review B*, vol. 46, pp. 15554-15557, 12/15/ 1992.
- [70] C. Herring, N. M. Johnson, and C. G. Van de Walle, "Energy levels of isolated interstitial hydrogen in silicon," *Physical Review B*, vol. 64, p. 125209, 09/11/ 2001.
- [71] R. W. Keyes, "Electronic Effects in the Elastic Properties of Semiconductors," in *Solid State Physics*. vol. 20, F. Seitz, D. Turnbull, and H. Ehrenreich, Eds., ed: Academic Press, 1968, pp. 37-90.
- [72] R. I. Revilla, X.-J. Li, Y.-L. Yang, and C. Wang, "Large Electric Field-Enhanced-Hardness Effect in a SiO₂ Film," *Scientific Reports*, vol. 4, p. 4523, 03/31/ 2014.
- [73] E. J. Ng, V. A. Hong, Y. Yang, C. H. Ahn, C. L. M. Everhart, and T. W. Kenny, "Temperature Dependence of the Elastic Constants of Doped Silicon," *Journal of Microelectromechanical Systems*, vol. 24, pp. 730-741, 2015.
- [74] W. Shockley and J. Bardeen, "Energy Bands and Mobilities in Monatomic Semiconductors," *Physical Review*, vol. 77, pp. 407-408, 02/01/ 1950.
- [75] J. Bardeen and W. Shockley, "Deformation Potentials and Mobilities in Non-Polar Crystals," *Physical Review*, vol. 80, pp. 72-80, 10/01/ 1950.

- [76] L. J. Bruner and R. W. Keyes, "Electronic Effect in the Elastic Constants of Germanium," *Physical Review Letters*, vol. 7, pp. 55-56, 07/15/ 1961.
- [77] A. R. Knudson, S. Buchner, P. McDonald, W. J. Stapor, A. B. Campbell, K. S. Grabowski, *et al.*, "The effects of radiation on MEMS accelerometers," *IEEE Transactions on Nuclear Science*, vol. 43, pp. 3122-3126, 1996.
- [78] C. S. Smith, "Piezoresistance Effect in Germanium and Silicon," *Physical Review*, vol. 94, pp. 42-49, 04/01/ 1954.
- [79] C.-S. Li, M.-H. Li, C.-C. Chen, C.-H. Chin, and S.-S. Li, "A Low-Voltage CMOS-Microelectromechanical Systems Thermal-Piezoresistive Resonator With $Q > 10000$," *IEEE Electron Device Letters*, vol. 36, pp. 192-194, 2015.
- [80] U. Gowrishetty, K. Walsh, J. Aebersold, T. Roussel, H. Millar, and D. Jackson, "Development of Ultra-Miniature Pressure Sensors for 1-French Biomedical Applications and Beyond," *Sensor Letters*, vol. 6, pp. 433-440, // 2008.
- [81] K. M. Walsh, H. T. Henderson, and G. N. De Brabander, "A fully-packaged silicon micromachined piezoresistive accelerometer," in *Southeastcon '92, Proceedings.*, *IEEE*, 1992, pp. 753-756 vol.2.
- [82] X. Li, X. Chen, Z. Song, P. Dong, and Y. Wang, "A microgyroscope with piezoresistance for both high-performance coriolis-effect detection and seesaw-like vibration control," *Journal of Microelectromechanical Systems*, vol. 15, pp. 1698-1707, 2006.
- [83] Y. Xu, J.-T. Lin, B. W. Alphenaar, and R. S. Keynton, "Viscous damping of microresonators for gas composition analysis," *Applied Physics Letters*, vol. 88, p. 143513, 2006.

- [84] T. Gotszalk, P. Grabiec, and I. W. Rangelow, "Piezoresistive sensors for scanning probe microscopy," *Ultramicroscopy*, vol. 82, pp. 39-48, 2// 2000.
- [85] Y. Kanda, "Piezoresistance effect of silicon," *Sensors and Actuators A: Physical*, vol. 28, pp. 83-91, 7// 1991.
- [86] Y. Kanda and Y. Kanda, "A graphical representation of the piezoresistance coefficients in silicon," *Electron Devices, IEEE Transactions on*, vol. 29, pp. 64-70, 1982.
- [87] Y. Kanda and K. Matsuda, "Piezoresistance Effect in p-Type Silicon," *AIP Conference Proceedings*, vol. 772, pp. 79-80, 2005.
- [88] K. Matsuda, Y. Kanda, K. Yamamura, and K. Suzuki, "Nonlinearity of piezoresistance effect in p- and n-Type silicon," *Sensors and Actuators A: Physical*, vol. 21, pp. 45-48, 1990/02/01 1990.
- [89] Y. Kanda and K. Suzuki, "Origin of the shear piezoresistance coefficient π_{44} of n-type silicon," *Phys Rev B Condens Matter*, vol. 43, pp. 6754-6756, Mar 15 1991.
- [90] H. Takahashi, A. Nakai, N. Thanh-Vinh, K. Matsumoto, and I. Shimoyama, "A triaxial tactile sensor without crosstalk using pairs of piezoresistive beams with sidewall doping," *Sensors and Actuators A: Physical*, vol. 199, pp. 43-48, 9/1/ 2013.
- [91] B. W. Chui, T. W. Kenny, H. J. Mamin, B. D. Terris, and D. Rugar, "Independent detection of vertical and lateral forces with a sidewall-implanted dual-axis piezoresistive cantilever," *Applied Physics Letters*, vol. 72, pp. 1388-1390, 1998.
- [92] K. Tetsuo, T. Hidetoshi, B.-K. Nguyen, A. Yuichiro, T. Yusuke, N. Kentaro, *et al.*, "Design of a piezoresistive triaxial force sensor probe using the sidewall doping

- method," *Journal of Micromechanics and Microengineering*, vol. 23, p. 035027, 2013.
- [93] G. Fuse, H. Umimoto, S. Odanaka, M. Wakabayashi, M. Fukumoto, and T. Ohzone, "Depth Profiles of Boron Atoms with Large Tilt-Angle Implantations," *Journal of The Electrochemical Society*, vol. 133, pp. 996-998, May 1, 1986 1986.
- [94] R. Kakoschke, R. E. Kaim, P. F. H. M. v. d. Meulen, and J. F. M. Westendorp, "Trench sidewall implantation with a parallel scanned ion beam," *IEEE Transactions on Electron Devices*, vol. 37, pp. 1052-1056, 1990.
- [95] P. C. Fletcher, Y. Xu, P. Gopinath, J. Williams, B. W. Alphenaar, R. D. Bradshaw, *et al.*, "Piezoresistive Geometry for Maximizing Microcantilever Array Sensitivity," in *University/Government/Industry Micro/Nano Symposium, 2008. UGIM 2008. 17th Biennial, 2008*, pp. 208-211.
- [96] R. D. Bradshaw, P. Fletcher, Y. Xu, B. Alphenaar, and R. Keynton, "Model optimization of a piezoresistive microactuation-based sensor for gas composition analysis," *ASME McMat*, 2007.
- [97] T. Tan, S. Mitchell, D. McNeill, H. Wadsworth, and S. Strahan, "A Computational Approach for Simulating P-type Silicon Piezoresistor Using Four Point Bending Setup," *Simulation*, vol. 6, p. 8.
- [98] M. Aikele, K. Bauer, W. Ficker, F. Neubauer, U. Prechtel, J. Schalk, *et al.*, "Resonant accelerometer with self-test," *Sensors and Actuators A: Physical*, vol. 92, pp. 161-167, 8/1/ 2001.
- [99] R. Amarasinghe, D. V. Dao, V. T. Dau, and S. Sugiyama, "Ultra miniature novel three-axis micro accelerometer," in *Sensors, 2009 IEEE*, 2009, pp. 1305-1308.

- [100] C. Hong, B. Minhang, H. Zhu, and S. Shen, "A piezoresistive accelerometer with a novel vertical beam structure," in *Solid State Sensors and Actuators, 1997. TRANSDUCERS '97 Chicago., 1997 International Conference on*, 1997, pp. 1201-1204 vol.2.
- [101] Y. Liu, Y. L. Zhao, and S. Lu, "An improved structural design for accelerometers based on cantilever beam-mass structure," *Sensor Review*, vol. 32, pp. 222-229, 2012.
- [102] A. Ranjith, D. Dzung Viet, T. Toshiyuki, and S. Susumu, "Simulation, fabrication and characterization of a three-axis piezoresistive accelerometer," *Smart Materials and Structures*, vol. 15, p. 1691, 2006.
- [103] K. L. Phan, J. T. M. van Beek, and G. E. J. Koops, "Piezoresistive ring-shaped MEMS resonator," in *Solid-State Sensors, Actuators and Microsystems Conference, 2009. TRANSDUCERS 2009. International*, 2009, pp. 1413-1416.
- [104] F. Laerme, A. Schilp, K. Funk, and M. Offenbergl, "Bosch deep silicon etching: improving uniformity and etch rate for advanced MEMS applications," in *Technical Digest. IEEE International MEMS 99 Conference. Twelfth IEEE International Conference on Micro Electro Mechanical Systems (Cat. No.99CH36291)*, 1999, pp. 211-216.
- [105] M. W. McCurdy, M. H. Mendenhall, R. A. Reed, B. R. Rogers, R. A. Weller, and R. D. Schrimpf, "Vanderbilt Pelletron - Low Energy Protons and Other Ions for Radiation Effects on Electronics," in *2015 IEEE Radiation Effects Data Workshop (REDW)*, 2015, pp. 1-6.

- [106] W. Young and R. Budynas, *Roark's Formulas for Stress and Strain*: McGraw-Hill Education, 2001.
- [107] A. United States. Environmental Protection Agency. Office of and Radiation. (1999). *UV radiation*. Available: <http://purl.access.gpo.gov/GPO/LPS22218>
- [108] M. A. Green and M. J. Keevers, "Optical properties of intrinsic silicon at 300 K," *Progress in Photovoltaics: Research and Applications*, vol. 3, pp. 189-192, 1995.
- [109] V. Fomenko and E. Borguet, "Combined electron-hole dynamics at UV-irradiated ultrathin Si-SiO₂ interfaces probed by second harmonic generation," *Physical Review B*, vol. 68, p. 081301, 08/07/ 2003.
- [110] T. A. Fjeldly, F. Cerdeira, and M. Cardona, "Effects of Free Carriers on Zone-Center Vibrational Modes in Heavily Doped p-type Si. I. Acoustical Modes," *Physical Review B*, vol. 8, pp. 4723-4733, 11/15/ 1973.
- [111] C. K. Kim, M. Cardona, and S. Rodriguez, "Effect of free carriers on the elastic constants of p-type silicon and germanium," *Physical Review B*, vol. 13, pp. 5429-5441, 06/15/ 1976.
- [112] E. Ungersboeck, S. Dhar, G. Karlowatz, V. Sverdlov, H. Kosina, and S. Selberherr, "The Effect of General Strain on the Band Structure and Electron Mobility of Silicon," *IEEE Transactions on Electron Devices*, vol. 54, pp. 2183-2190, 2007.
- [113] J. J. Hall, "Electronic Effects in the Elastic Constants of n-Type Silicon," *Physical Review*, vol. 161, pp. 756-761, 09/15/ 1967.
- [114] A. Jaakkola, M. Prunnila, T. Pensala, J. Dekker, and P. Pekko, "Determination of doping and temperature-dependent elastic constants of degenerately doped silicon

- from MEMS resonators," *IEEE Transactions on Ultrasonics, Ferroelectrics, and Frequency Control*, vol. 61, pp. 1063-1074, 2014.
- [115] F. P. Beer and E. R. Johnston, Jr., *Mechanics of Materials*: McGraw-Hill, Inc., 1981.
- [116] K. J. Chang and D. J. Chadi, "Hydrogen bonding and diffusion in crystalline silicon," *Physical Review B*, vol. 40, pp. 11644-11653, 12/15/ 1989.
- [117] S. N. Rashkeev, C. R. Cirba, D. M. Fleetwood, R. D. Schrimpf, S. C. Witzak, A. Michez, *et al.*, "Physical model for enhanced interface-trap formation at low dose rates," *IEEE Transactions on Nuclear Science*, vol. 49, pp. 2650-2655, 2002.
- [118] S. N. Rashkeev, D. M. Fleetwood, R. D. Schrimpf, and S. T. Pantelides, "Effects of hydrogen motion on interface trap formation and annealing," *IEEE Transactions on Nuclear Science*, vol. 51, pp. 3158-3165, 2004.
- [119] L. Tsetseris, R. D. Schrimpf, D. M. Fleetwood, R. L. Pease, and S. T. Pantelides, "Common origin for enhanced low-dose-rate sensitivity and bias temperature instability under negative bias," *IEEE Transactions on Nuclear Science*, vol. 52, pp. 2265-2271, 2005.

CURRICULUM VITA

Pranoy Deb Shuvra

2204 James Guthrie Ct., Apt. 3, Louisville, KY-40217; (502) 794-5490

pranoydebshuvra@gmail.com

SUMMARY OF QUALIFICATIONS

- 6+ years of working experience in well-equipped cleanroom facility fabricating and designing MEMS devices such as resonators, accelerometer, pressure sensors and, MOSFETs.
- Extensive experience in designing, modeling and simulating MEMS devices with commercial FEM software such as COMSOL and CoventorWare.
- Designed a MEMS energy storage device that stores electrical and mechanical energy.
- Fabricated MEMS devices using large band gap material such as GaN.

EDUCATION

Doctor of Philosophy, Electrical Engineering

University of Louisville, Louisville, KY, USA

2012-2018

GPA 3.977/4.00

Dissertation: “Exploration of Radiation Damage Mechanism in MEMS devices”

Advisor: Dr. Shamus McNamara

M.S., Applied Physics, Electronics and Communication Engineering
2009-2010
University of Chittagong, Chittagong, Bangladesh
GPA 3.98/4.00

B.Sc., Applied Physics, Electronics and Communication Engineering
2005-2009
University of Chittagong, Chittagong, Bangladesh
GPA 3.76/4.00

TECHNICAL SKILLS

Micro-fabrication

- Wet etching of metals and insulators; RCA cleaning; Dry etching using Trion Metal Etcher, DRIE & MARCH RIE;
- Oxidation; Annealing and; Diffusion
- Thin film deposition using sputtering machines such as PVD75 and TECHNICS 4604.
- Optical Lithography: Photomask Design in L-edit, Alignment and Exposure with SUSS Mask Aligner.

Characterization

- Thin film characterization using DEKTAK profilometer, surface profiling using ZYGO interferometer, Atomic Force Microscopy (AFM) and Scanning Electron Microscopy (SEM).
- XRD for grain size determination.

Testing & Packaging

- Electrical characterization such as C-V and I-V measurement with LCR meter, Parameter Analyzer and Lock-in Amplifier.
- Vacuum probe station equipped with turbo pump to conduct electrical testing in controlled environment.
- Wire bonding in chip carriers with K&S 4524 Digital Ball Bonder.

CAD, DAQ and FEM software

- Athena for modeling fab sequence, Atlas to simulate electrical testing on athena model.
- COMSOL and CoventorWare for Finite Element Analysis (FEM) of designed MEMS devices.
- MATLAB and MATHCAD for mathematical model simulation.
- Solidworks and CANVAS for graphical design and illustration.
- LABVIEW for computer assisted data acquisition, sorting and analysis.
- Igor pro for data storage, analysis and visualization.
- Minitab for design of experiment.

Other skills

- Programming languages: C, JAVA, Python, Assembly for microcontroller AVR and PIC, Android programming, machine learning.
- Teaching skills: Conducted undergraduate classes and labs both as a teaching assistant in US and as Lecturer at Bangladesh.

EXPERIENCE

Research Assistant, Dept. of Electrical and Computer Engineering

University of Louisville, Louisville. KY-40217

- Designed, simulated and optimized piezoresistive MEMS resonator.
- Developed lumped model that helped explain the physical mechanism of the resonator.
- Successfully fabricated and packaged MEMS resonator.
- Characterized the fabricated resonators before and after x-ray exposure.
- Designed and fabricated sensitive MEMS accelerometers.
- Developed successful fabrication process of GaN semiconductor MEMS devices.

Teaching assistant, Dept. of Electrical and Computer Engineering, University of Louisville, Louisville. KY-40217

PUBLICATIONS AND PATENT

-
-
- [1] P. D. Shuvra and S. McNamara, "The strain capacitor: A novel energy storage device," *AIP Advances*, vol. 4, p. 127158, 2014/12/01 2014.

- [2] P. D. Shuvra, S. McNamara, J. Lin, B. Alphenaar, K. Walsh, and J. Davidson, "Axial asymmetry for improved sensitivity in MEMS piezoresistors," *Journal of Micromechanics and Microengineering*, vol. 26, p. 095014, 2016.
- [3] J. T. Lin, P. D. Shuvra, S. McNamara, H. Gong, W. Liao, J. L. Davidson, *et al.*, "Near-Surface Electronic Contribution to Semiconductor Elasticity," *Physical Review Applied*, vol. 8, p. 034013, 09/18/ 2017.
- [4] J. T. Lin, P. D. Shuvra, W. Liao, S. McNamara, K. M. Walsh, C. N. Arutt, *et al.*, "Surface carrier concentration effect on elastic modulus of piezoelectric MEMS silicon cantilevers," in *2017 19th International Conference on Solid-State Sensors, Actuators and Microsystems (TRANSDUCERS)*, 2017, pp. 1175-1178.
- [5] C. N. Arutt, P. D. Shuvra, J. Lin, M. L. Alles, B. W. Alphenaar, J. L. Davidson, *et al.*, "Dopant-Type and -Concentration Dependence of Total-Ionizing-Dose Response in Piezoresistive Micromachined Cantilevers," *IEEE Transactions on Nuclear Science*, pp. 1-1, 2018.
- [6] C. N. Arutt, W. Liao, H. Gong, P. D. Shuvra, J. T. Lin, M. L. Alles, *et al.*, "Dose-Rate Effects on the Total-Ionizing-Dose Response of Piezoresistive Micromachined Cantilevers," *IEEE Transactions on Nuclear Science*, vol. 65, pp. 58-63, 2018.
- [7] H. Gong, W. Liao, E. X. Zhang, A. L. Sternberg, M. W. McCurdy, J. L. Davidson, *et al.*, "Total-Ionizing-Dose Effects in Piezoresistive Micromachined Cantilevers," *IEEE Transactions on Nuclear Science*, vol. 64, pp. 263-268, 2017.
- [8] N. A. Charles, L. A. Michael, L. Wenjun, G. Huiqi, L. D. Jim, D. S. Ronald, *et al.*, "The study of radiation effects in emerging micro and nano electro mechanical systems (M and NEMs)," *Semiconductor Science and Technology*, vol. 32, p. 013005, 2017.
- [9] H. Gong, W. Liao, E. X. Zhang, A. L. Sternberg, M. W. McCurdy, J. L. Davidson, *et al.*, "Proton-Induced Displacement Damage and Total-Ionizing-Dose Effects on Silicon-Based MEMS Resonators," *IEEE Transactions on Nuclear Science*, vol. 65, pp. 34-38, 2018.
- [10] P. D. Shuvra and S. McNamara, "Strain Capacitor Energy Storage Devices and Assemblies" (Patent pending).

POSTER PRESENTATIONS

- [1] Pranoy Deb Shuvra and Shamus McNamara, “Louisville Strain Capacitor”, KY NSF EPSCoR conference, October 17, 2013.
- [2] Pranoy Deb Shuvra and Shamus McNamara, “Strain Capacitor as a novel Energy Storage Device”, RE³ Workshop, Renewable energy and energy efficiency, March 22-24, 2015.
- [3] Pranoy Deb Shuvra *et al.*, “Proton-Induced Total-Ionizing-Dose and Displacement-Damage Effects on Silicon Based MEMS Resonators” 2017 IEEE Nuclear and Space Radiation Effects Conference, New Orleans, Louisiana July 17-21, 2017
- [4] Pranoy Deb Shuvra *et al.*, “Dose-Rate Effects on the Total Ionizing Dose Response of Piezoresistive Micromachined Cantilevers” 2017 IEEE Nuclear and Space Radiation Effects Conference, New Orleans, Louisiana July 17-21, 2017
- [5] Pranoy Deb Shuvra *et al.* “Surface Carrier Concentration Effect on Elastic Modulus of Piezoelectric Mems Silicon Cantilevers”, Transducers 2017, The 19th International Conference on Solid-State Sensors, Actuators and Microsystems, Kaohsiung, Taiwan June 18-22, 2017.
- [6] Pranoy Deb Shuvra *et al.* “Radiation effect on MEMS devices”, Speed Research Exposition, University of Louisville, Kentucky March 2-3, 2018.